

Sheffield Hallam University

Electrodynamic sensors and neural networks for electrical charge tomography.

BIDIN, Abdul Rahman.

Available from the Sheffield Hallam University Research Archive (SHURA) at:

<http://shura.shu.ac.uk/19355/>

A Sheffield Hallam University thesis

This thesis is protected by copyright which belongs to the author.

The content must not be changed in any way or sold commercially in any format or medium without the formal permission of the author.

When referring to this work, full bibliographic details including the author, title, awarding institution and date of the thesis must be given.

Please visit <http://shura.shu.ac.uk/19355/> and <http://shura.shu.ac.uk/information.html> for further details about copyright and re-use permissions.



Sheffield Hallam University
REFERENCE ONLY

ProQuest Number: 10694236

All rights reserved

INFORMATION TO ALL USERS

The quality of this reproduction is dependent upon the quality of the copy submitted.

In the unlikely event that the author did not send a complete manuscript and there are missing pages, these will be noted. Also, if material had to be removed, a note will indicate the deletion.



ProQuest 10694236

Published by ProQuest LLC (2017). Copyright of the Dissertation is held by the Author.

All rights reserved.

This work is protected against unauthorized copying under Title 17, United States Code
Microform Edition © ProQuest LLC.

ProQuest LLC.
789 East Eisenhower Parkway
P.O. Box 1346
Ann Arbor, MI 48106 – 1346

**Electrodynamic Sensors and Neural Networks
for Electrical Charge Tomography**

by

Abdul Rahman Bidin

A thesis submitted to

The Sheffield Hallam University

for the degree of

Doctor of Philosophy

in the

School of Engineering Information Technology

June 1993

Dedication.

**I dedicate this work to my wife, Ainee,
for her love and support during those difficult years.**

Acknowledgement.

I would like to record my sincere and heartfelt thanks to my Guru, Dr Bob Green, for his intelligent supervision, helpful suggestions and constructive criticisms of my work. I am extremely grateful for his emphatic support and encouragement throughout the period of my study.

I would also like to thank my co-supervisors, Dr R W Taylor of York University, for the neural network aspects of the research and Dr M E Shackleton for her useful comments.

My thanks are also due to colleagues at Du Pont, Dr Arthur Boxman for the finer aspects of particle behaviour in flow processes and Dr Reg Davies for the invitation to the US Engineering Foundation Workshop on Control of Particulate Processes in Santa Barbara on January 24-29th 1993.

To the guys in Unit 4 Science Park; I have enjoyed their stimulating discussions and company: Mohammad Hadawi, Kristof Chylewski, Dave Barass, Tony Daniels and Jan Nordin.

My special thanks to Imad Sheibani and Don Rimmer for the quality of technical help in the preparation of the work materials.

There has been generous help from lecturers for which I am grateful: Mr Alan Taylor-Firth for provision of space in his construction laboratory, Dr Ken Dutton for his cross-correlation program, Mr Brett Naylor for the construction details of the measurement system, Dr Ian Halliday for discussions on the physics of electrical charge systems and Dr Ivan Basarab for comments on the thesis.

The financial assistance from the Malaysian Government, Universiti Pertanian Malaysia and Leche Trust of the British Council is highly appreciated, and without which this research could not have been possible.

The Du Pont award for the contribution and continuation of this research, is an honour which I shall cherish throughout my career.

The trials and tribulations throughout the Phd work have indeed been a humbling experience and I submit in humility and gratitude to Almighty God for all His blessings and generous help from sources that were beyond my expectation.

Table of Contents

Abstract.	1
Chapter 1 An Overview of process tomography.	3
1.1 Process Tomography.	3
1.2 Use of tomography in powder and particulate processes.	4
1.4 The Thesis Outline.	7
Chapter 2 Review of Tomography Sensors and Applications.	9
2.1 Introduction.	9
2.2 Tomography sensors.	9
2.3 Electrical charge tomography.	13
2.4 Flow regime identification from tomographic data by neural networks.	15
2.5 Conclusions from literature review.	18
Chapter 3 Electrodynamic Models	19
3.1 Electrification of particulates in pneumatic transport.	19
3.2 The single-particle charge model.	20
3.2.1 Assumptions for the models.	20
3.2.2 The induction model.	22
3.2.3 The field model.	25
3.2.4 The response to a moving particle.	27
3.3 The two-particle charge model.	29
3.4 The multi-particle charge model.	32
3.5 Mass flowrate model.	36
Chapter 4 Signal Analysis Methods.	38
4.1 Introduction.	38
4.2 Cross correlation and power spectral density.	38
4.3 Neural networks.	41
4.3.1 The Kohonen network.	42
4.3.2 Learning parameters.	45
4.3.3 Classification maps.	56
4.3.4 Regime identification from synthetic data.	62
Chapter 5 The Measurement System.	64
5.1 The transducer.	64
5.2 The 16-channel circular array sensor configuration.	66
5.3 Data acquisition system.	70
5.4 Signal processing software.	72
5.5 The bead flow rig.	72
5.6 The sand flow rig.	74
5.7 The flow models.	76
Chapter 6 The Experiments and Results.	78
6.1 Introduction.	78
6.2 Single particle flow experiment.	78
6.2.1 Bead flow measurements by oscilloscope.	78
6.2.2 Results using the data acquisition system.	80

6.2.2.1 Sensor response in time domain.	80
6.2.2.2 Spatial profile from sensor output.	81
6.3 Boundary voltage measurements of sand flow.	84
6.3.1 The procedures.	84
6.3.2 Sensor response to flow noise.	84
6.3.3 Flow regime profiles.	85
6.3.3.1 Full flow	85
6.3.3.2 Half flow	86
6.3.3.3 Stratified flow	87
6.3.3.4 Annular flow	88
6.3.3.5 Core flow	89
6.4 Velocity measurements of sand flow.	90
6.4.1 The procedures.	90
6.4.2 Cross correlation results.	90
Chapter 7 Analysis of Results.	94
7.1 Introduction.	94
7.2 Single particle flow.	95
7.2.1 Verification of induction model.	95
7.2.2 Particle location from normalised voltage profile.	95
7.2.3 Spectral analysis for a single bead.	97
7.3 Voltage profiles for sand flow.	99
7.3.1 Full flow.	100
7.3.2 Half flow.	101
7.3.3 Stratified flow.	102
7.3.4 Annular flow.	103
7.3.5 Discussion on flow profiles.	103
7.3.6 Comparison of models with sand flow results.	104
7.4 Flow regime identification from measured data.	105
7.4.1 The training patterns.	105
7.4.2 The neural map classifier.	108
7.4.3 The test patterns.	109
7.5 Velocity and mass flowrate estimations.	110
7.5.1 Velocity from cross correlation.	111
7.5.2 Mass flowrate from velocity and voltage measurements.	111
7.5.3 Effects of baffles on velocity and mass flowrate.	116
7.6 Spectral analysis of electrodynamic signals.	117
7.6.1 Power spectrum of flow signals.	117
7.6.1.1 Full flow.	118
7.6.1.2 Half flow.	120
7.6.1.2.1 Collisions.	121
7.6.1.2.2 Hydrodynamics.	121
7.6.1.2.3 Clustering.	121
7.6.1.3 Annular flow.	122
7.6.1.4 Core flow.	125
7.6.1.5 Stratified flow.	127
7.7 Ratio backprojection for empirically-based image reconstruction.	128
7.7.1 Single particle flow reconstruction.	129
7.7.2 Sand flow reconstruction.	130
Chapter 8 Conclusions and Recommendations for Further Work.	134
8.1 General conclusions.	134

8.1.1 Single particle models.	134
8.1.2 Two particle model.	134
8.1.3 Multiparticle model.	135
8.1.4 Neural network models.	135
8.1.5 Electrodynamic transducers.	136
8.1.6 Artificial flow regimes.	136
8.1.7 Boundary voltage profiles of sand flow.	136
8.1.8 Flow regime identification.	137
8.1.9 Velocity determination.	137
8.1.10 Spectral analysis.	137
8.1.11 Image reconstruction.	138
8.2 Suggestions for further work.	138
8.2.1 The mathematical models.	138
8.2.2 Improvements to the flow rig.	139
8.2.3 Sensor systems.	139
8.2.4 Range of flows.	140
8.2.5 Neural networks.	140
8.2.6 Cross correlation.	141
8.2.7 Reconstruction algorithms.	141
8.2.8 Particle sizing.	142
8.2.9 Effect of particle size.	143
8.2.10 Application in liquids flow.	143
References.	144
Publications of the Research.	155
2.1 Publications list.	155
2.2 ECAPT Task 3 report.	156
2.3 Du Pont invited paper.	156

Abstract.

This research into the feasibility of imaging particulate processes using electrical charge tomography investigates four techniques: the multi-sensing of electrical charge in a cross-section, a neural network based classifier for flow regime identification, cross correlation based velocity determination and spectral analysis of electrodynamic signals.

A single charged-particle model is developed to simulate the induction effect on a sensor by a charge. The spatial representation of the voltage induced onto sixteen sensors, placed on the boundary of a circular pipe, gives a flow distribution profile over the cross-section.

A two charged-particle model is developed to simulate the electrodynamic effect of two particles on a tomographic sensor configuration. As in the single particle model, a spatial representation of the voltages induced onto the sensors is presented. This voltage profile is due to the combined effects of position and charge of the two particles.

A multi-particle model is developed to predict the voltage profile of several flow regimes: full, annular, core, half and stratified. The model is extended to provide the loading and concentration of a given flow.

A measurement system is constructed consisting of sixteen sensors equally spaced around the boundary of a circular 100mm pipe. Measurements on a bead drop system are designed to verify the single particle model.

A sand flow system, consisting mainly of 300 micron sized particles, is used for measurements of the induced voltages due to different flow regimes. The latter are created artificially by using baffles of different shapes that obstruct the sand flow.

The voltage profile from the sixteen sensors gives spatial information about the flow regime. These voltage profiles are normalised into patterns that are presented to a Kohonen neural network for classification. Two regime classification between well differentiated regimes gives an accuracy of identification of 95%. This is expanded to provide classification of three regimes with more variability in the input patterns giving success rates between 50% to 70%.

A power spectral density analysis of the measured electrodynamic signals gives observable features for particle characterisation during flow. In full flow, with no baffles obstructing the sand flow, a consistently high frequency spectra of 550Hz is observed. At flow rates above 0.540 kgs^{-1} , the frequency spectra shifts to a lower range of 200Hz. In obstructed flow, such as in stratified regime, an inhomogeneous phase is inferred from the drop in frequency of the power spectra at relatively low flowrates (0.36 kgs^{-1}). These results suggest a relationship between the observed spectra and the phenomenon of clustering of particles at higher concentrations. The potential of electrodynamic spectroscopy for particle characterisation in terms of size distribution is discussed.

Knowledge of flow regime voltage profile, regime identification and concentration provided a basis for an empirically based image reconstruction algorithm.

Finally the achievements of the thesis are discussed and suggestions made for further work.

Chapter 1

An Overview of Process Tomography.

1.1 Process Tomography.

Tomography comes from the Greek words tomo (slice) and graph (picture). As defined in one encyclopaedia [Helicon 1992] , it is the obtaining of plane section images, which show a slice through an object. In this project, the objective is to investigate the feasibility of using electrodynamic sensors and neural networks, together with an image reconstruction algorithm, to produce an image such as the velocity, concentration and size distribution profiles at a cross-section of a pipe conveying dry particulates.

Process Tomography is a developing measurement technology. It is gaining attention from industry because of some recent successes and the increased work into various fundamental aspects of the technology. As demonstrated by the first international workshop on Process Tomography held last year [ECAPT92, 1992] which reported new sensing techniques, new algorithms and began to address the fundamental challenges such as resolution, speed of acquisition, quality of information and other factors that are essential to make the technology acceptable to industrial practice.

The specific characteristic of tomographic measurement is its proven ability to interrogate the dynamic state of a process condition within a unit operation such as a mixing vessel or conveyor without interfering with the process itself. This is achieved using non-invasive sensors along a cross-sectional boundary of the process equipment. The tomographic measurement data is manipulated using algorithms for image reconstruction, profile analysis and numerical quantities such as flow rates, concentration, size and phase distribution.

From the knowledge of material distribution and movement, improved internal models involving kinetic and dynamic parameters can be derived and used as an aid to optimise process design. This is in sharp contrast to present day design methodology which usually assumes time and space averaged parameters such as well mixed reactors, completely fluidised beds, fully dispersed emulsions and so on.

Currently, models based on for example, a computational fluid dynamics approach, are used to simulate the internal phenomenon of a particular process. Tomographic techniques can contribute further by verifying these models which eventually may lead to better dynamic models when the two technologies are combined [Illyas 1993].

The measurements made by a process tomography system capture micro-scale data at points and average these parameters in both time and space. Hence, more useful knowledge of a process condition is available at lower cost than the more expensive techniques of laser or NMR methods. From an on-line monitoring point of view, tomography techniques will be advantageous.

1.2 Use of tomography in powder and particulate processes.

Pneumatic and hydraulic conveying is currently used to transport solids over distances ranging from a few meters to several kilometers. This method of transportation is used in the chemical industry because it is cheaper and less hazardous than conventional transportation by rail and road.

In pneumatic conveying, particles are moved by drag force from the air flow. The parameters which affect the conveying process include the flow velocity, distribution of gas/solid fraction, the pressure gradient, physical size distribution of the material. These

may all contribute to the different flow characteristics or regimes in the conveying pipeline, which affect the efficiency of energy consumption [Beck 1986] or cause blockage and damage to pipes.

In horizontal pneumatic conveying, the flow regimes generated depend upon the conveying gas velocity. In dense phase transport where gas velocity is relatively low, the distribution of solid particles tend to become less uniform and form a moving bed on the base of the pipeline. At a critical deposition velocity, particles will deposit on the surface of these beds, an effect known as saltation [Rhodes 1990]. Hence, knowledge of these regimes, in particular when an internal image is made available, will help to monitor effects during transport.

On the other hand, in vertical pneumatic transport, at low gas velocity and high loading factor, that is dense phase conveying, the particles move in clouds along the pipe in a flow regime very similar in formation to slug flow in gas/liquid transport. At high gas velocities and low solids loading, that is light phase conveying, the flow has a more uniform distribution. At lower gas velocity, a transition from homogenous or uniform flow to annular flow is observed. This transition may be a useful parameter for plant control if it can be monitored. In these, tomography would have the ability to obtain real time information about these regimes.

The information that can be derived from the tomography sensors will enable velocity, flowrate and concentration to be determined over a wide range of flow regimes by providing better averaging in time and space through multi-projections of the same observation.

BRITISH THESIS SERVICE

DX 176131 Page count 166

Batch number 9

Comments:

Awarding body SHEFFIELD HALLAM

Thesis by BIDIN. A. R.

We have assigned this thesis the number given at the top of this sheet.

In your notification to ASLIB, please quote this number so that it can be included in their *Index to Theses with Abstracts*.

THE BRITISH LIBRARY
DOCUMENT SUPPLY CENTRE

Many measurement techniques have been applied to the pneumatic transport of powder and particulates [Henry et al 1977, Coulthard 1992]. Tomography will provide an increase in the quantity and quality of information available when compared to earlier techniques.

The specific objectives of this thesis are:

1. Familiarise with the concepts of process tomography, associated sensor technology and neural networks.
2. Define the specifications of the problems to be investigated in order to demonstrate the feasibility of developing a working technique for electrodynamic tomography.
3. Develop a mathematical model of this system and compare measured and predicted values.
4. Specify, design and construct a measurement system consisting of sixteen transducers, the associated measurement electronics and data acquisition to a personal computer (PC) environment.
5. Use this system with test phantoms to produce data for a charged particle with known axial position and velocity.
6. Extend the single particle problem to a multi-particle problem by using sand as the test media.
7. Apply neural networks for classification of flow data into known flow regimes or image profiles.

8. Investigate the feasibility of this system determining velocity, concentration and mass flow rates.
9. Analyse the measured data in the frequency domain for possible additional information relating to the particle.
10. Develop algorithms for image reconstruction from the measurements and secondary data.

Figure 1.1 shows the inter-relation of the specific objectives.

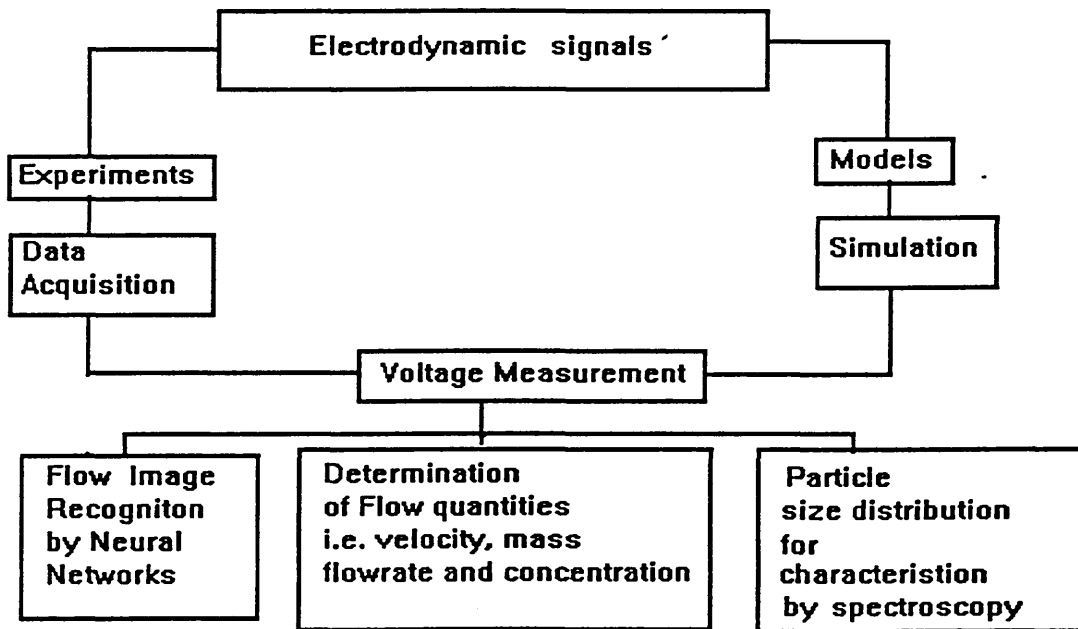


Figure 1.1: Diagram of the research plan.

1.4 The Thesis Outline.

Chapter 2 presents an overview of Process Tomography. Several sensing mechanisms for measurement using non-intrusive techniques are discussed. An electrodynamic system is proposed and applications in powder processing outlined.

Chapter 3 investigates electrical charge theory and uses models to predict the output voltages from point sensors placed along the circumference of the conveying pipe. A generalised model is derived which considers the different flow regimes that pass through the sensing volume due to distribution variations during transport.

Neural networks are investigated for application in process tomography because they can interpret and classify the data obtained into its various categories of likeness. Results of theoretical studies to understand the workings and behaviour of the neural network and its application in pattern recognition of artificial data and measured data is presented in **Chapter 4**.

Chapter 5 describes the design, construction and testing of the 16-channel, circular array, electrodynamic sensor and transducer system.

To verify the models, experiments based on a charged, single bead were conducted and are reported in **Chapter 6**. This chapter also describes experiments using sand as the flowing media. Phantom flow regimes from these measurements are then identified by neural networks.

Chapter 7 discuss the results obtained and the prototype electrodynamic flowmeter and process tomography system.

Chapter 8 presents the overall conclusions and recommendations for future research. This chapter is followed by the references and appendices.

Chapter 2

Review of

Tomography Sensors and Applications.

2.1 Introduction.

This chapter provides an overview of electrical measurement systems for Process Tomography applications. A typical system is shown in figure 2.1

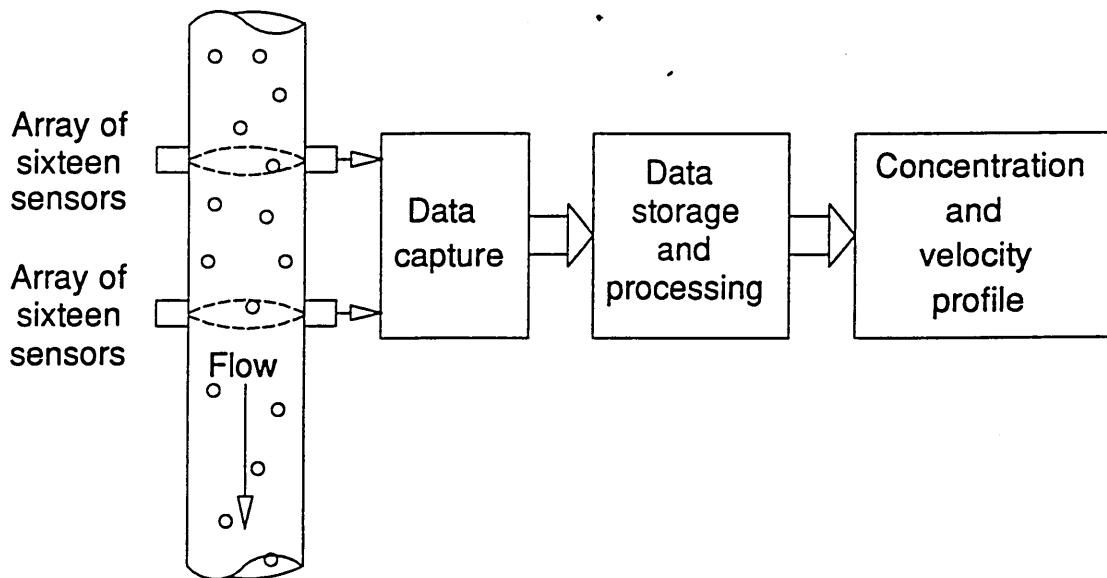


Figure 2.1: A Process Tomography System.

2.2 Tomography sensors.

There are three basic components in a process tomography system:

- a. The sensors
- b. The data acquisition system
- c. The image reconstruction system and display.

Sensor technology is undoubtedly the most essential and critical part of any measurement system. The sensors in a tomography system are usually placed in a circular array; a 16-channel sensor system is quite typical. This is to provide multi projections of the object or event being measured. The main advantages derived from such a configuration are:

1. Replicated measurements obtained at a local level can be used for improved reliability and to provide a better averaging of the process parameter being measured.
2. Surface spatial distribution of the material or an object is obtained directly from the measurement.
3. Multi-component spatial distributions can be obtained through image reconstruction techniques.
4. Structural information about process materials may be obtained by using spectral analysis techniques.

There are many reports on the work which has gone into imaging of liquid flow and gas-liquid flows. Two possible reasons for this are the interest by oil production companies in using capacitance techniques for oil production pipeline monitoring [Huang 1988] and the direct applications of medical electrical impedance tomography [Barber and Brown 1984] to the process industry.

There are not many reports of work to visualise the flow of solids from physical measurements. However, experimental work done using liquid media does not necessarily

limit the use of the basic principles to gas/solids flow. For example, Plaskowski [1991] developed an imaging system for two component air/solids flow intended for the food industry using capacitance transducers.

The reported techniques for tomographic imaging are based on sensing of electrical impedance [Abdullah 1993, Binley et al 1993], induced current [Freeston et al,1993], optics [Xie et al 1993], infra red [Dugdale 1991] and ultra sound [Li et al 1993]. This research aims to use electrodynamic measurements for imaging in process tomography.

The following discussion reports some existing work on sensor technology for process tomography with a view to positioning the electrodynamic technique in the overall scenario of the subject domain.

Electrical sensing is by far the most common method which has been investigated in process tomography research. Electrical capacitance tomography has been developed at UMIST [Huang et al, 1988] based on transducers developed by Huang [1988].

Huang's capacitance measuring circuit is based on the charge transfer principle. A number of capacitance electrodes are mounted on the circumference of a flow pipe and interrogated in turn by electronic control. Measurements are based on changes in capacitance values between electrodes due to the variations in permittivities of the flowing material.

Recently, Huang et al [1991] developed a system for application in oil/gas two-phase flow. A new 12-electrode system was used to increase the spatial resolution from the earlier 8-electrode system. For example, geometric parameters affect the non-uniform field inside the flow pipe resulting in a non-uniform sensitivity distribution over the pipe cross section, which is undesirable. Xie et al [1991] developed a system model based on

the finite element method to describe the capacitance system. Khan and Abdullah [1991] demonstrated a design based on finite element models in order to illustrate the design difficulties faced in earlier designs such as that by Xie et al [1989]. Plaskowski et al [1991] developed a similar prototype commercial system aimed for pneumatic conveying in the food industry.

Electrical impedance sensors have also been used with success in process tomography. Based on the earlier work done by Brown and Barber [1984], [Abdullah 1993] developed a system that can generate a sequence of images depicting the distribution of components or concentration profiles of components across a given plane within a reactor or pipeline as function of time. Electrodes are placed into a vessel wall in order to make measurements of the distribution of electrical resistance within an object plane. Measurements are performed by injecting an ac current via one pair of adjacent electrodes and measuring the voltages at all other pairs of adjacent electrodes. The procedure is repeated for all possible pairs of electrodes and is referred to as the 4-electrode adjacent pair measurement protocol [Dickin et al 1991]. The reconstruction of images from these data uses a series of procedures performed iteratively to determine the distribution of regions of different resistivities representing for instance, component concentrations within a cross section of the pipe or vessel.

Non-electrical methods (such as optical tomographic measurement) have been developed by Dugdale et al [1991] based on an earlier theoretical investigation by Saeed et al [1988]. The basic system is designed around pairs of optical transducers consisting of a GaAs Infra-red light emitting diode and a silicon PIN photodiode. Pulses of IR radiation are emitted by the LED and optically configured to form a collimated beam through the flow regime in a pipe to a photodiode receiver. Attenuation of the beam due to the flow

component concentration causes a corresponding change in the voltage generated by the sensors. Identification of flow regimes such as bubble, churn or plug flow is then obtained by signal processing of the outputs from the transducers. Further processing enables tomograms relating to the concentrations to be generated.

2.3 Electrical charge tomography.

The motivation for using electrodynamic sensors as the sensing device in tomography arises from the fact that many flowing materials pick up charge during transport, primarily by virtue of friction of fine particles amongst themselves and abrasion on the walls of the conveyor [Cross, 1987]. Hence by measuring the voltages induced on sensors placed around the wall of a conveyor, it is possible to obtain spatial information of the transported material within the conveyor.

The term electrodynamics is used to describe the effects of a moving charge as opposed to electrostatics where the charge is stationary. One of the earliest reported works on using electrical charge measurements or electrodynamics is that by King [1973]. He developed a method of relating the electrodynamic noise level, solids mass flow rate and particle-electrode collision rate to theoretical models of intensity of turbulence within a horizontal two phase pipe flow. The method allows the monitoring of the rate at which electrical charge, which is termed streaming current, is conveyed through a pipe by flowing dielectric fluids.

Electrodynamic sensors have been used successfully in the past by several studies [King 1973, Shackleton 1982, Beck CM 1986, Gregory IM, 1987, Gajewski JB 1990, Coulthard 1992]. These were of ring or single pin electrode type. Information obtained from these

measurements showed that mass flowrate, velocity and concentration were obtainable from sensing the electrical charge. These earlier developments were however, insufficient for determining the distribution profile of the flow.

In an industrial application, Featherstone et al [1982], measured yarn velocity in the textile process. In this method, electrically charged yarn is passed through two metal loops which act as sensors. This induces charge on each metal loop which is then amplified by an ac coupled charge-to-voltage converter. The outputs are cross correlated, designed for online velocity measurement. The transit time for the charge to travel between the two points is measured and velocity was calculated from this.

Shot velocity measurement using electrodynamic sensors was studied by Gregory [1987]. Electrostatic variations within a flow were detected by two axially spaced electrodynamic sensors. These sensors measured the random changes in induced charge arising from the turbulent nature of pneumatic conveying. Cross-correlation was used to obtain the velocity. This work considered very light phase conveying of shot particles and the measurements were verified by high-speed photography.

Beck [1986] investigated the efficiency of energy consumption in pneumatic conveying with a measurement system using electrodynamic sensors. A relationship is found between the electrical energy consumption by a pilot plant blower and the solids velocity, obtained through cross correlation of electrodynamic signals.

Electrical charge tomography uses sensor electronics based on earlier work by Shackleton [1981] who used a ring electrode to detect induced charges. Results showed the potential for such transducers to be applied in measurement of charge carrying processes.

2.4 Flow regime identification from tomographic data by neural networks.

Flow regime identification is important in the process industry for plant condition monitoring. The efficiency of conveying and energy consumption, for instance, determine how the materials flow through the pipes. The task of imaging as a means to determine the flow regime requires high computational cost and time. An identification technique directly from measurements provide a more practical solution.

Xie [1988] used a statistical method to calculate the fingerprint of a flow regime. This method, however, requires the computation of the fingerprint identifier every time a set of measurement data is presented for identification. It is thought that an adaptive pattern recognition technique would be able to classify flow regimes from given sets of measurements. This adaptive pattern recognition technique is based on the neural network learning model [Pao 1989].

In the late 80's, there was a sudden resurgence of interest in Neural Networks. Even though the origins of the work [Hebb 1949] predates the emergence of the first digital computer, it was only recently that the increase in neural-network research and applications started [Rumelhart et al 1986].

Studies of the mind and brain are fundamentally domains of neurophysiologists and psychologists [Grossberg 1982]. Neuroscience, as it is often called, has collected vast amounts of data about the brain, ranging from characterisation of the structure of single molecules and ionic channels to imaging brain activity while the brain carries out some cognitive task.

When the mathematical models of the brain functions improved and with the help of computers, a better description of the brain in terms of neural network models could be made [Hestenes 1987]. Over the last forty years, before the mid 80's, only very few learning rules have been developed. New ones have emerged, either as variations of established rules or by new approaches using different theories in Mathematics or Physics.

The principle of neural network learning is based on the simple processing of a single neuron interconnected to other neurons, together acting as a whole unit. Each neuron is activated upon presentation of an input stimuli. The level of activation depends on a threshold limit to trigger a response from the neuron [McClelland et al 1986].

There are three basic learning methods [Karna et al 1989]: supervised, reinforcement and unsupervised learning. In supervised learning, a network is given an example of an input and also the correct output. The network will filter the input, produce an output and compare the calculated output and the correct output. Weights within the network are adjusted to minimise the error. In this scheme, there is a teacher (feedback) to correct outputs. In reinforcement learning, the network is not given the correct output but only told if the output produced is good or bad. With unsupervised learning, a network develops its own classification rules by extracting information from examples presented to the network.

Computing with neural networks, or simply neural computing, is an adaptive learning system. Its goal is to achieve flexibility. Natural situations are highly variable and cannot be foreseen completely by a program. The solution of building very large software systems

considering contingency plans or detailed algorithms for all possible situations is economically unfeasible, inflexible and error-prone. On the contrary, neural networks attain flexibility by formulating the fixed aspects of a structure on an abstract and general level.

The above adaptation capability is called self organisation [Kohonen 1984]. The neural network adjusts its own parameters during a training stage so as to learn the inputs presented to it (figure 2.2). In the test phase, the neural network tries to get the best match between what it has learnt and the test input until a stable solution is reached.

Unlike conventional computing, neural computing has the capability to generalize. The system works by storing particular elements, but the results of its operations are to form generalizations of these particular instances, even though the generalizations are never stored directly. It is also described as having a functional use of experiential knowledge [Aleksander 1988]. It is here that the neural networks can perform functions beyond the capability of rule based conventional systems. Indeed, it is a system that exhibits intelligence and logic, without the explicit rules as in the case of expert systems.

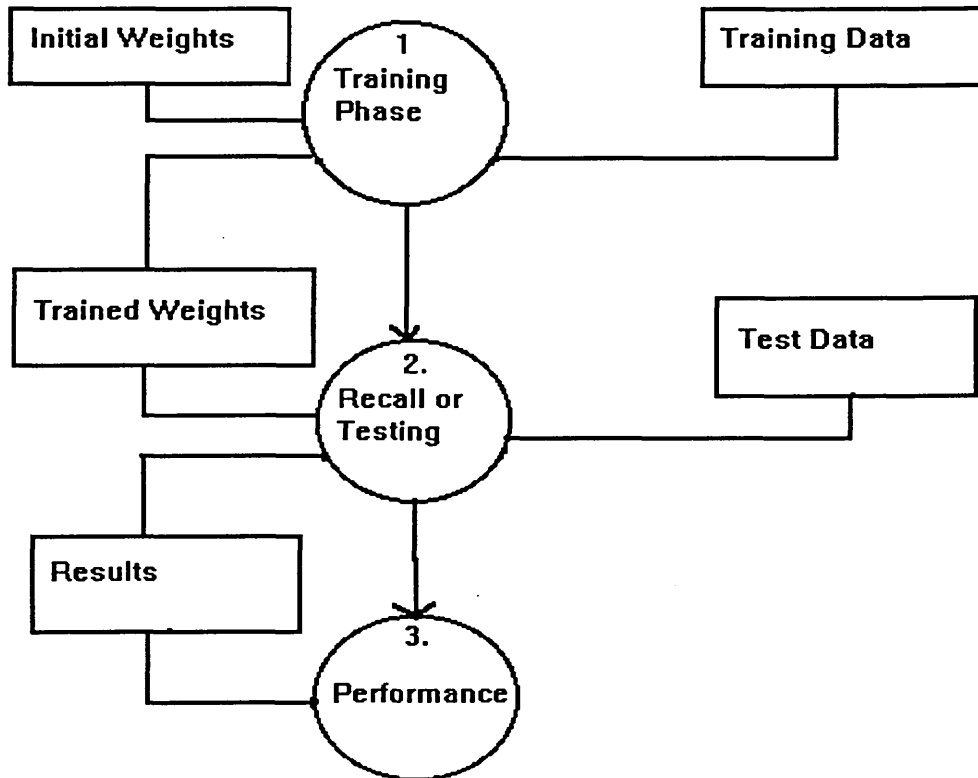


Figure 2.2. Stages in the usage of neural network system.

2.5 Conclusions from literature review.

From this overview, it appears a combination of electrodynamic sensors, because of their high sensitivity, and neural networks, because of their pattern recognition ability, may be suitable for concentration and velocity profiling of dry particulates in pneumatic and gravity drop systems. The next chapter presents a development of some theoretical models of the effects of electrostatic charge on particles onto sensors.

Chapter 3

Electrodynamic Models

3.1 Electrification of particulates in pneumatic transport.

The generation of electrical charge by pneumatic transport of materials has been known for many years. The magnitude of this charge is dependent on various factors including type of material, conducting or non conducting, the quantity involved, moisture level, air flow rate and physical characteristics of the particles and conveyor.

The mechanism by which electrical charge is generated during flow can be classified in many ways [Kelly et al 1989],

a) Tribo-electrification.

This occurs when two dry solid surfaces come into contact due to movement. This occurs with many types of surfaces such as two conductors or between conductor and non-conductor. The mechanism involves transfer of ions between the two surfaces as a result of surface forces [Harper 1967].

b) Homogeneous charge separation.

When a particle breaks up, two smaller particles are created carrying equal and opposite charges with no net accumulation of charge.

In the context of powder processing, both of the above mechanisms occur. Irrespective of how they occur, as the charged particles pass the surface of a sensor placed in a conveyor wall it induces charge. This mechanism was studied by Shackleton [1981].

A detailed review of electrostatic phenomenon in particulate processes, by Lapple [1970], provides useful data. The relationship between electrical properties and particle characteristics, such as particle size and size distribution, for processes involving particles are discussed.

This work focuses on the measurement of this electrical charge for the purpose of determining some related parameters for flow and particle characterisation.

3.2 The single-particle charge model.

Models are considered which relate the charge on a particle to the voltage on a sensor. Two static models are developed based on induction (section 3.2.2) and electric field (section 3.2.3) effects. Tests (section 6.2) support the induction model and this is used to develop the moving charge model (section 3.2.4).

3.2.1 Assumptions for the models.

The model considers a vertical, downward flow of particles in a pipeline. These particles are all assumed to possess a stable electrostatic charge.

Now assume that by superposition, the net effect due to the charges from the various particles in the particulate cloud result in a single point charge. This charge can be assumed to be a single particle travelling in the axial direction of the pipeline, not necessarily coinciding with the central axis of the pipeline.

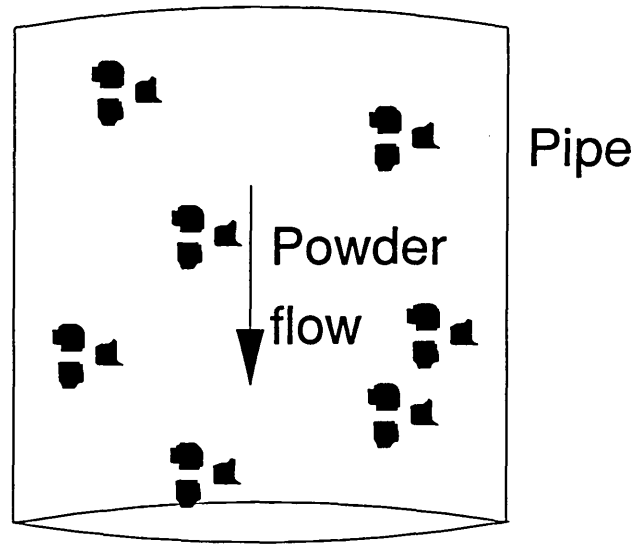


Figure 3.1: Particle flow through pipe.

The fundamental assumptions made with this model are:

1. The particle is travelling in a direction parallel to the axis of the pipe.
2. This particle has a constant finite amount of charge which is not dissipated over the period it travels through the sensing volume.
3. The surface area of the electrode is small compared to the radius of the pipe, hence the electric field does not vary over the cross-sectional plane of the sensor geometry (figure 3.2).
4. There is a perfect earth shield from interacting fields external to the sensing volume.
5. The charge is a regular shaped sphere with a constant surface charge density.

6. The sensor capacitance is maintained constant by a concentric earth shield around the pipe mounting.

7. The medium in the sensing volume is air (relative permittivity is 1).

The sensors along the pipe wall detect the passing charged particle. The potential measured on any one sensor is described by a relationship which depends on the effects of induction, field of the particle or possibly both these effects. The following sections discuss these possible effects.

3.2.2 The induction model.

For a single charged particle, q , the field E is uniformly radial over its surface [Duckworth 1960],

$$E = \frac{q}{4\pi r^2 \epsilon_0} \quad (3.1)$$

where ϵ_0 is the permittivity of free space (8.854×10^{-12} F/m) and air (relative permittivity 1) is the dielectric medium.

It is assumed in this model that the field results in a charge appearing on the surface of an electrode used to sense the change in potential at a point on the wall of a non-conducting or dielectric pipe.

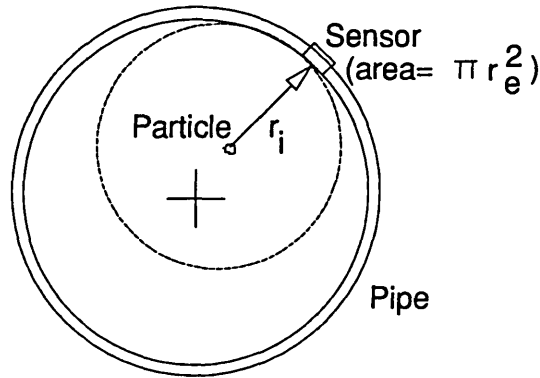


Figure 3.2 A model of charged particle in a sensing volume.

For a given sensor, the surface area is πr_e^2 which is normal to the flux. The surface area of the flux at the radius of the sensor, assumed to be spherical, is $4\pi r_i^2$. So the proportion of flux for each sensor is $\pi r_e^2 / 4\pi r_i^2$

The induced charge in the i th sensor, Q_{induced} will be proportional to the charge on the particle, q (figure 3.2). Hence, with fixed sensor size,

$$Q_{\text{induced}} = \frac{k r_e^2 q}{4 r_i^2} = \frac{k_1 q}{r_i^2} \quad (3.2)$$

But $Q_{\text{induced}} = C V_{\text{induced}}$ and the capacitance C is constant for all sensors, therefore

$$Q_{\text{induced}} = k_2 V_{\text{induced}}$$

Substituting for Q_{induced} in equation (3.2) gives,

$$V_{\text{induced}} = k_3 \frac{q}{r_i^2} \quad (3.3)$$

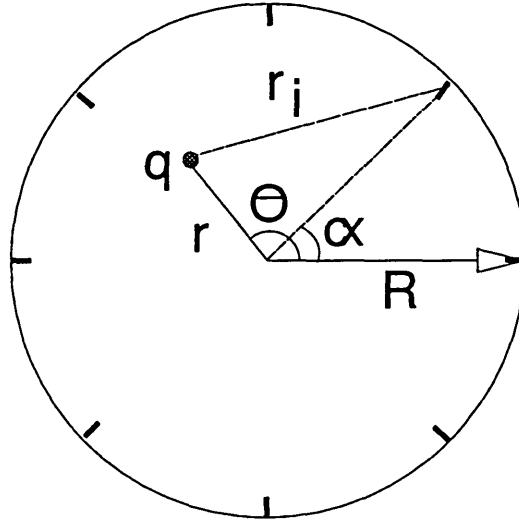


Figure 3.3 : Geometry of sensor and particle.

From figure 3.3, the distance from the charge to the sensor is given by the geometrical relation

$$r_i = \sqrt{r^2 + R^2 - 2Rr \cos(\theta - \alpha)} \quad (3.4)$$

The angle θ is the radial position of the charge, while α is that for the sensor location from a diametrical reference axis.

Because q and k are unknowns in the equation 3.3, for a given r and R , the voltages are normalised over the maximum voltage realised, v_{\max} to cancel out any constant terms in the model due to sensor or pipe geometry and size of charge. Hence,

$$v_{i,normalised} = \frac{v_i}{v_{\max}} = \left(\frac{r_{\max}}{r_i} \right)^2 \quad (3.5)$$

From this model, an estimation of the profile of the boundary voltages is reconstructed by plotting the sensor output voltage against position on the circumference of the pipe (figure 3.4). It is possible to simulate different positions of the charged particle by changing the values of r and θ in equation 3.4. However, changing θ only shifts the angular offset of the profiles. Hence, only results from one diametrical axis are shown.

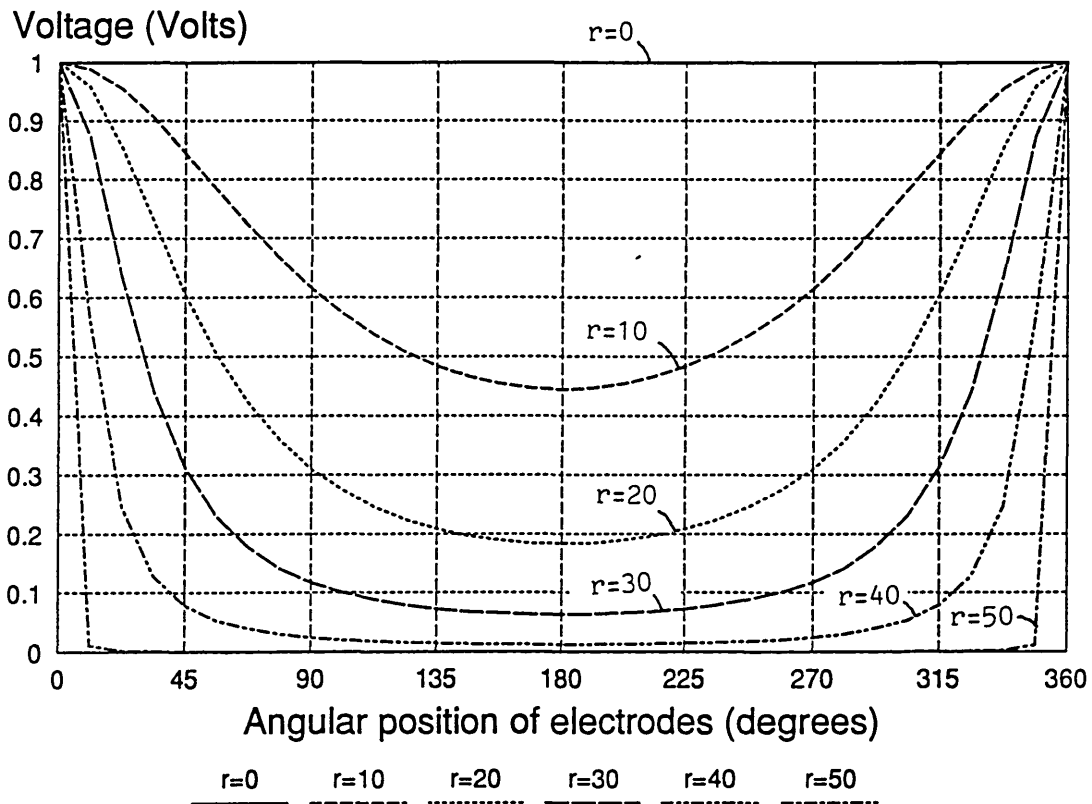


Figure 3.4 Theoretical voltage profile based on induced sensor model.

3.2.3 The field model.

For a point charge, q , the field E , is uniformly radial [Neff 1991].

$$E = \frac{q}{4\pi r^2 \epsilon_0} \quad (3.6)$$

The resulting potential becomes,

$$V = \int -E dr = \frac{q}{4\pi r \epsilon_0} \quad (3.7)$$

The particle can be considered to be surrounded by equipotential spheres.

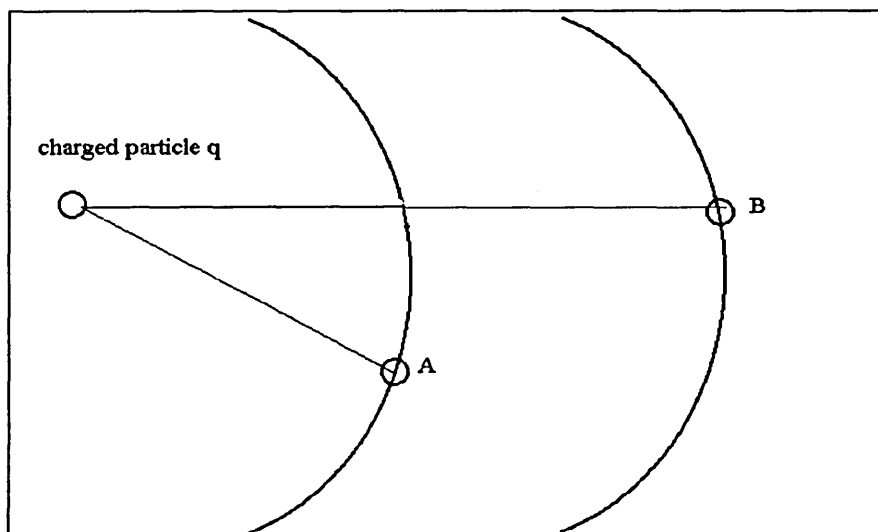


Figure 3.5 Equipotential lines from charge.

The potential at sensor A is $q/4\pi r_a \epsilon_0$ and that at B is $q/4\pi r_b \epsilon_0$. It is assumed that there is no interaction with the surroundings and that V can be measured without distorting the field. The measured voltage is then the potential difference between A and B;

$$V = \frac{q}{4\pi \epsilon_0} \left(\frac{1}{r_a} - \frac{1}{r_b} \right) \quad (3.8)$$

3.2.4 The response to a moving particle.

Assume an electrode at the origin, and a particle (charge q) moving at constant velocity v along the line $x=D, z=0$.

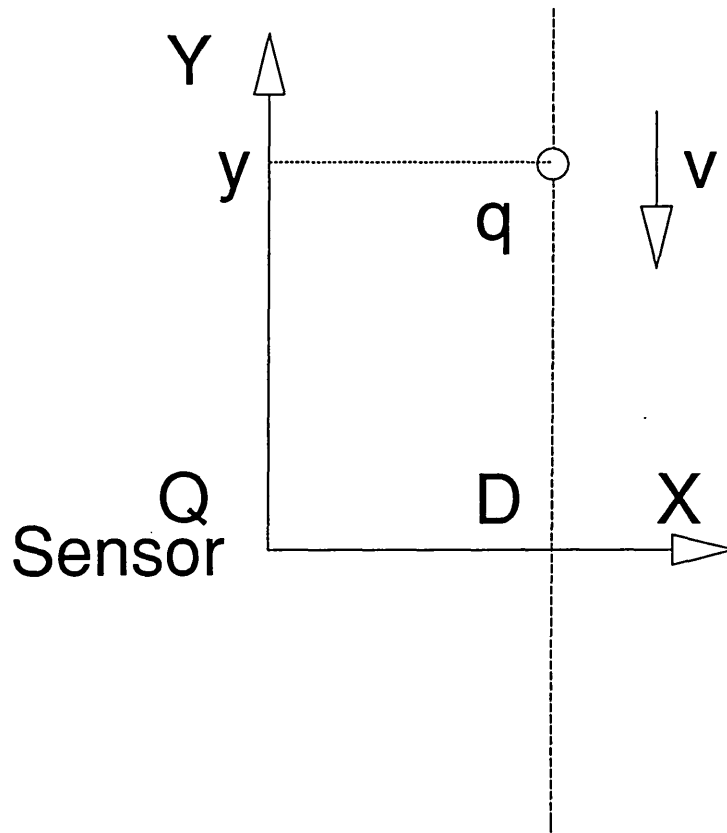


figure 3.6 Moving charge through measurement section.

Experimental results shown in section 6.2 support the induction model. Therefore, assuming the inverse square law relationship holds, then the induced charge Q is given by:

$$Q = -kq \frac{1}{D^2 + y^2} \quad (3.9)$$

where $y=vt$ and $t=0$ when the particle is directly opposite the electrode. The equation then becomes

$$Q = -kq \frac{1}{D^2 + v^2 t^2} \quad (3.10)$$

This charge Q is varying with time and results in a current $\frac{dQ}{dt}$

flowing into the sensor from the measurement circuit. The current, i , is given by

$$\frac{dQ}{dt} = 2kq \frac{v^2 t}{(D^2 + v^2 t^2)^2}$$

The current flows into and out of the capacitor via a resistance R , resulting in a varying voltage, V .

Results for this case have been evaluated for $v=5$ m/s and for $D=10$ mm. The results are shown graphically in figure 3.7.

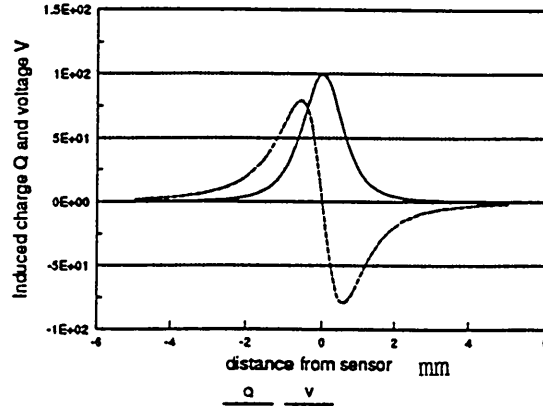


Figure 3.7. Induced charge and voltage due to moving particle.

3.3 The two-particle charge model.

By superposition, the potential induced by two charged particles can be found from [Neff 1991],

$$V = k(q1 + q2) \quad (3.12)$$

$$= k(p1/r12 + p2/r22) \quad (3.13)$$

where V is the potential induced by the two charged particles, p1 and p2, at known radial positions, r1 and r2. As in section 3.2, normalisation is used to ratio the predicted responses from all the sensors to the peak value calculated for each configuration of the two charges.

Figure 3.8a-f shows calculated results for two particles, p1 and p2, assumed to possess the same amount of charge for different spatial positions.

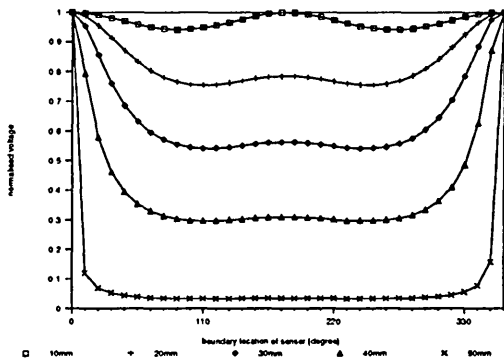


Figure 3.8(a) p1 fixed at (10mm,180) and p2 moving from 10mm towards 50mm on 0° radius.

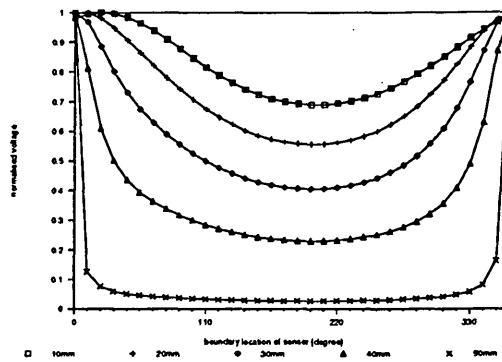


Figure 3.8(b) p1 fixed at (10mm,45) and p2 moving from 10mm towards 50mm on 0° radius.

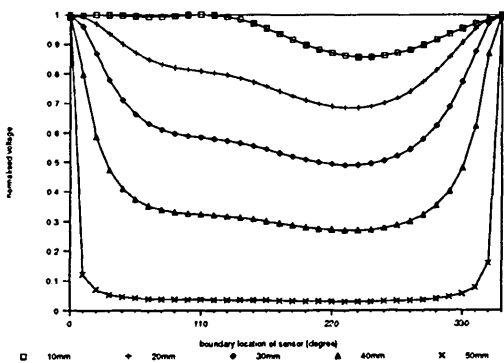


Figure 3.8(c) p1 fixed at (10mm,135) and p2 moving from 10mm towards 50mm on 0° radius.

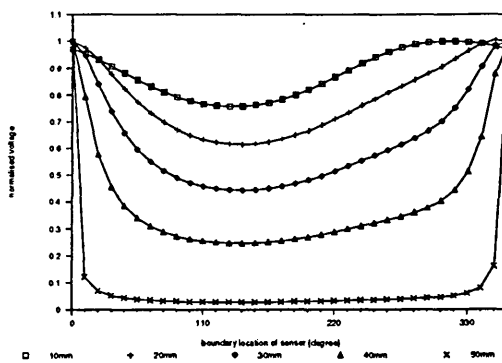


Figure 3.8(d) p1 fixed at (10mm,270) and p2 moving from 10mm towards 50mm on 0° radius.

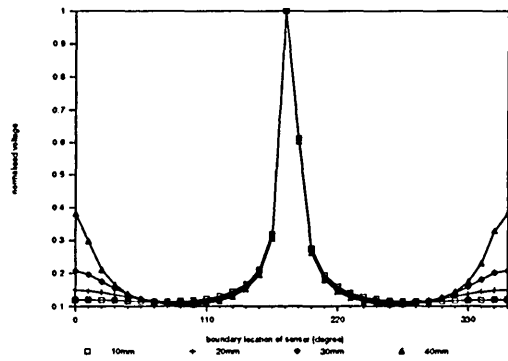


Figure 3.8(e) p1 fixed at (50mm,180) and p2 moving from 10mm towards 50mm on 0° radius.

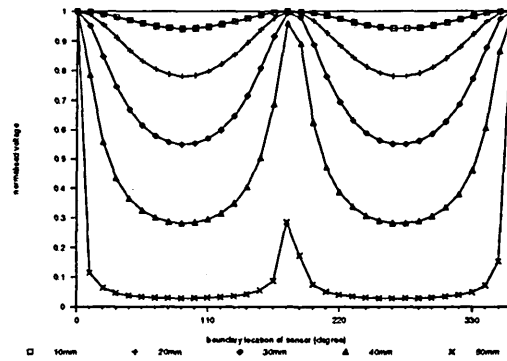


Figure 3.8(f) p1 and p2 moving from 10mm towards 50mm position on the 180° and 0° radius.

Figure 3.8. Results showing calculated sensor outputs for a two particle model.

The results of the simulations show that, with the location of particle p1 fixed and p2 moving radially outwards towards the pipe wall, the voltage profile of the two-particle system is definable by two distinct features:

1. When the two particles are similar distances from the pipe wall two distinct peaks are observed. These peaks occur at the sensors on the same radii as the particles. For instance, in figure 3.8a, particle p1 is fixed at 10mm on the 180° radius while p2 moves towards the sensor in the opposite direction which gives a maximum voltage on the 180° sensor. This peak value shifts towards the closest sensor approached by the moving particle p2, figures 3.8b-d.
2. The range of maximum and minimum normalised values increases as the particle p2 gets closer to the sensor, as would have been expected.

In figure 3.8e, particle p1 is placed very near the sensor ($r_1=50\text{mm}$) at the 180° position. Moving particle p2 has no significant effect in changing the voltage profile until it is at a comparable distance to a sensor. Moving the two particles symmetrically in opposite directions produces the voltage profile shown in figure 3.8f. The two peaks are fixed but the range increases as the particles move towards the wall.

3.4 The multi-particle charge model.

The potential at a point (sensor) due to the total charge on a volume of charge is given by [Johnk 1988],

$$u_i = k \iiint \frac{\rho_v}{r_i} dV \quad (3.14)$$

where the integration extends over the entire volume occupied by the charge and

$$k = 1/4\pi\epsilon_0\epsilon$$

and r_i is the distance of the charge to the i 'th sensor, while V is the sensing volume defined by the pipe radius r , the pipe angular distance α and axial sensing distance x .

From equation 3.14,

$$\begin{aligned} \rho_v &= \frac{\text{amount of charge}}{\text{volume of material}} \\ &= \frac{Q}{V} \end{aligned}$$

$$\rho_v = \frac{Q}{A_f x} = \frac{\rho_s}{x} \quad (3.15)$$

where A_f = area of material flow and ρ_s is the surface charge density since it is the total charge (Q) over surface area (A_f) in equation 3.15. This result applies the divergence theorem [Duckworth 1960] when a transform between a surface integral and a volume integral is required. Then,

$$\rho_s = \frac{Q}{A_f}$$

assuming there is no change of concentration in the volume of flow considered.

$$\frac{A_f}{A} \approx \sigma \quad (3.16)$$

approximates to the instantaneous solids loading where A is the cross sectional area of the pipe. Therefore,

$$Q = \rho_s \sigma A \quad (3.17)$$

can be assumed constant and equation 3.14 becomes

$$\begin{aligned}
u_i &= k \frac{Q}{r_i} \\
U_i &= G u_i \\
&= \frac{k_g Q}{r_i}
\end{aligned} \tag{3.18}$$

The voltage U_i for each sensor i , is obtained from the potential by introducing a gain term G which depends on the resistance and capacitance used in the circuit to transduce the input from the probe to the data acquisition system (section 5.1). This gain term can be modelled [Gajeswski 1989] and should be investigated further (section 8.2.1).

By plotting the voltage readings against the sensor location the effective charge source is located. In order to check this proposition the following cases are considered:

1. Uniform, annular and core flows.

In these cases, the charge will be symmetrical about the central axis and effectively at the centre, $(r, \theta) = origin$. At $r = 0$ and $\theta = 0$,

$$r_i = \sqrt{r^2 + R^2 - 2rR \cos(\theta - \alpha)} \tag{3.19}$$

gives $r_i = R$, therefore $U_i = constant$.

2. Half flow.

For $r = 0.5R$,

when $\theta = 0$ on the reference axis.

$$r_i = \sqrt{\left(\frac{1}{4}R^2 + R^2 - 2 \cdot R^2 \cdot \cos(\theta - \alpha)\right)} \quad (3.20)$$

$$= R\left(\frac{5}{4} + \cos \alpha\right)^{0.5} \quad (3.21)$$

When all sensor voltages are normalised to the maximum voltage, then,

$$U_{i,normalised} = \frac{r_{max}}{r_i} \quad (3.22)$$

$$= \frac{(1.25 + \cos 0)^{0.5}}{(1.25 + \cos \alpha_i)^{0.5}} \quad (3.23)$$

$$= 1.5(1.25 + \cos \alpha_i)^{-0.5} \quad (3.24)$$

The normalization in equation 3.24 cancels out the constant terms. The following derivations show the result without normalization but require the constant quantities, including the charge density, to be known.

From equations (3.17) and (3.18), a relation to find the solid volume loading σ can be derived as shown below.

$$\begin{aligned} U &= \frac{k_g Q}{r_i} \\ &= \frac{k_g \sigma A \rho_s}{r_i} \\ \sigma &= \frac{r_i U_i}{k_g A \rho_s} \\ \therefore \sigma &= k_d r_i U_i \end{aligned} \quad (3.25)$$

For the full, core and annular flow, charge is assumed to be effectively at the centre. The equation 3.25 is rearranged to become,

$$U_i = \frac{\sigma}{k_d} \cdot \frac{1}{r_i} \quad (3.26)$$

For half flow, assuming the lumped charge is at 0.5R on the reference axis,

$$r_i = R(1.25 + \cos \alpha)^{0.5} \quad (3.27)$$

as shown in section 3.4. Hence,

$$U_i = \frac{\sigma}{k_d R} (1.25 + \cos \alpha)^{-0.5} \quad (3.28)$$

The result of this equation is similar to equation 3.24, amplified by the constant terms.

3.5 Mass flowrate model.

The mass flow rate is found from the relation,

$$\dot{m}_i = A_f v_i \rho \quad (3.29)$$

$$= \sigma A v_i \rho \quad (3.30)$$

where A_f is the area of flow at velocity v_i in pipe of cross section A. The ratio of flow area over pipe area is σ .

Substitute for σ from equation (3.26). Then

$$\dot{m}_i = A \rho v_i \frac{r_i U_i}{k A \rho_s} \quad (3.31)$$

$$\therefore \dot{m}_i = k_m v_i r_i U_i \quad (3.32)$$

Substituting for r_i from equation (3.32), the local mass flow rate for full, core and annular flows is given by,

$$\dot{m}_i = k_m v_i U_i R \quad (3.33)$$

The weighted sum for all the sensors relates to the average mass flow rate, for even distribution of particles.

Chapter 4

Signal Analysis Methods.

4.1 Introduction.

In this work three methods of analysis are used:

1. Cross-correlation of upstream and downstream signals for obtaining the velocity of solids flowing through the pipe, required in the calculation of the particulate mass flowrate.
2. Determination of power spectral density for sensor outputs, used in the analysis of the flow characteristics of the particulates .
3. Neural networks for identification of the flow regime from the distributed data from the measurement system.

4.2 Cross correlation and power spectral density.

These two techniques of analysis are well established in the literature. In this section, the definitions are presented.

The cross correlation function relating two signals $f_1(t)$ and $f_2(t)$ may be defined as [Beck and Plaskowski 1990]

$$r_{xy}(\tau) = \lim_{T_0 \rightarrow \infty} \frac{1}{T_0} \int_{-T_0/2}^{T_0/2} f_1(t) \cdot f_2(t + \tau) dt \quad (4.1)$$

where τ is a time shift imposed upon one of the signals. The value of τ corresponding to the peak of the cross correlation function is τ_m , which is physically realised in terms of the time taken by particles to travel between two sensors separated by a distance d , upstream and downstream, in the pipe, figure 4.1. This time delay is used to calculate the mean velocity of the particles between the sensors:

$$v = \frac{d}{\tau_m} \quad (4.2)$$

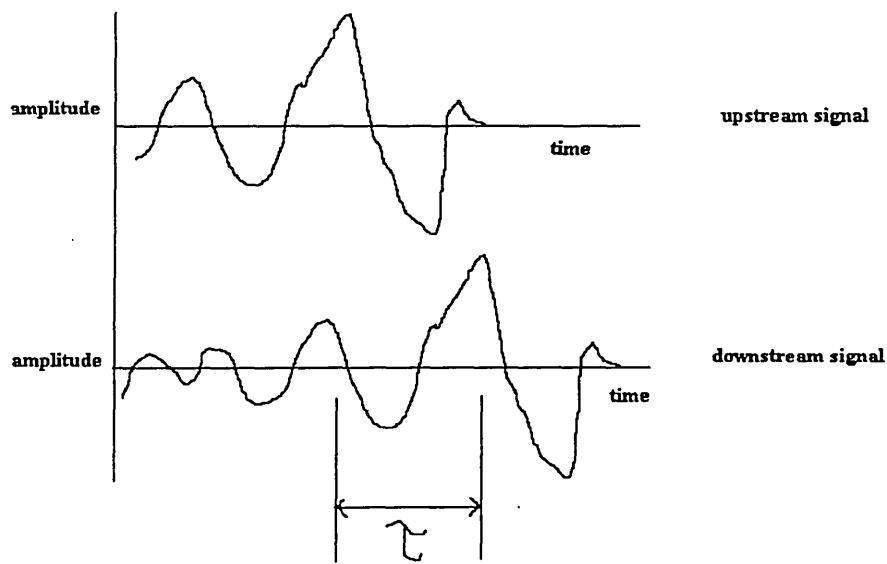


Figure 4.1a. Upstream and downstream signals.

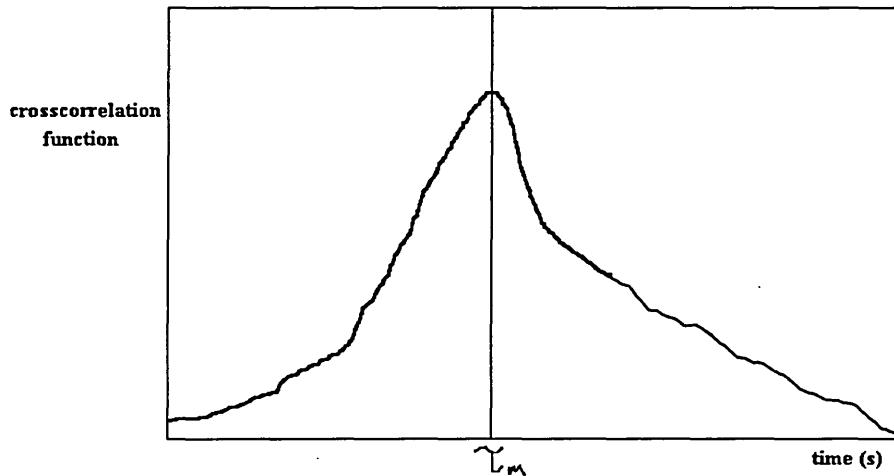


Figure 4.1b. Corresponding correlogram.

Figure 4.1. Cross correlation of two time varying signals.

The power spectral density function of a signal waveform gives the average power of the corresponding spectral components contained in the signal [Meade and Dillon 1986].

A general description of a signal in terms of Fourier analysis is given by the following relation for the harmonic series based on the fundamental frequency ω :

$$x(t) = A_0 + \sum_{m=1}^{\infty} A_m \cos(m\omega_0 t) + \sum_{m=1}^{\infty} B_m \sin(m\omega_0 t) \quad (4.3)$$

The coefficients A_m and B_m are respectively the Fourier cosine and sine coefficients representing the amplitudes of the various components used in the description of the signal. The power of the signal is given by:

$$P_x = A_0^2 + \frac{A_1^2}{2} + \frac{A_2^2}{2} \dots + \frac{B_1^2}{2} + \frac{B_2^2}{2} + \dots \quad (4.4)$$

The amplitude of the various terms indicates the average power of the spectral terms in the signal. This technique of analysis is useful in relating a signal to the underlying physical properties of a system [Lynn 1989], as has been demonstrated in some studies with flowmeter signals for condition monitoring [Higham et al 1986, Amadi-Echandu et al 1990].

4.3 Neural networks.

It is found [Kohonen 1984] that the various areas of the brain, especially of the cerebral cortex, are organised according to different sensory stimuli. Localised regions in the brain do different tasks such as speech, vision, action and so on. These regions may be modelled as feature maps. The model is derived from an idealisation of an abstraction of how a neuron might work. An important characteristic of these maps is the ordering of the basic processing units or neurons into an optimal topological order. This spatial ordering is necessary for an effective representation of information.

The maps formed in the brain are said to self-organise in such a way as to be able to relate the input signals to the specific regions on the maps. For example, in the auditory cortex it is possible to distinguish a spatial ordering of the neurons which reflects the frequency response of the auditory system. A tonotopic map exists that corresponds to a logarithmic scale of frequency where low frequency will generate response at one end of the cortex region and high frequencies at the opposite end.

4.3.1 The Kohonen network.

Kohonen [1984] formulated a self organising neural network architecture based on the close resemblance to the biological phenomenon of feature maps in the brain. This architecture consists of a layer of input neurons and an output layer of neurons, figure 4.2. Each neuron in the input layer is connected to every neuron in the output layer, and the strength of these interconnections, termed the weights, determine the relationship between an input pattern and the corresponding region of neurons in the output layer or map.

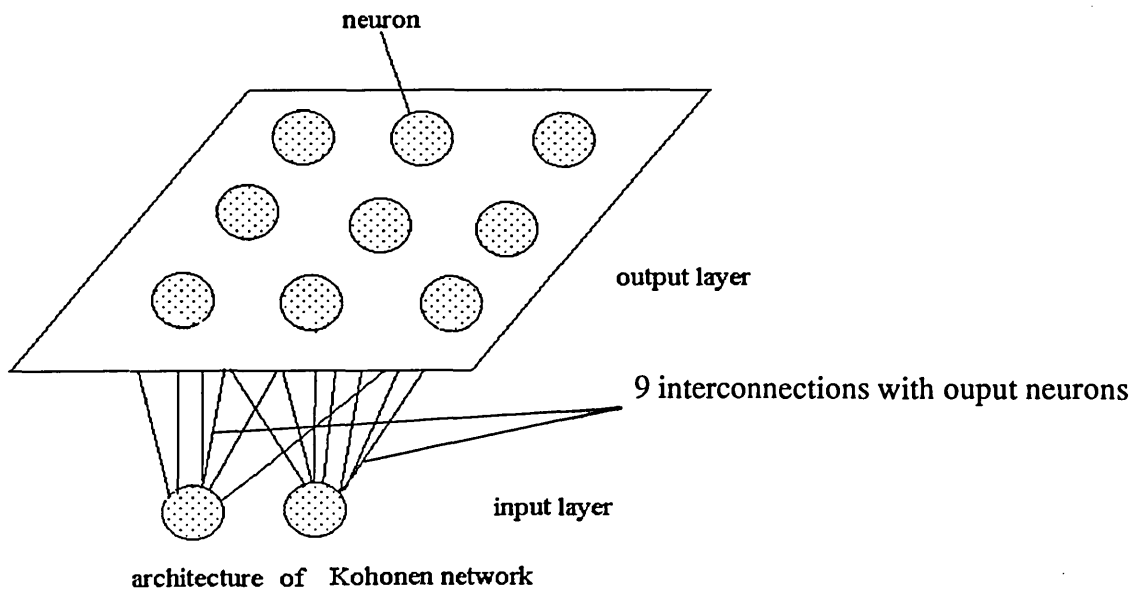


Figure 4.2. Architecture of Kohonen network.

He developed a self organising feature map based on a technique called vector quantisation [Kohonen 1988]. Essentially, vector quantisation forces the input signals to be mapped onto an output layer of processing elements, analogous to the neurons, in such a way as to make these elements selective and sensitive to particular characteristic features of the received signals. This is the basic adaptive capability of the whole system.

The network will respond to different inputs in an ordered fashion as if a continuous map of the input space were formed over the network. This can be explained from the fact that the weight vectors of neighbouring neurons are modified in the same direction until the values are smoothed. This smoothing process will continue until the weight vectors attain limit values which then define a vector quantisation of the input signal space where discrete regions are partitioned and thus a classification of all its vectors is formed.

Kohonen's learning rule uses the concept of competitive learning in a one-layer network. It is an unsupervised learning system because there is no training example of input with correct output. Hence, it develops its own classification rules.

Figure 4.3 shows the steps involved in the Kohonen learning algorithm. The rule works on the principle of competition between output nodes or processing elements. A winner from the layer of processing elements is chosen based on a best-match of the weight vectors with the presented input vector. The weight of this processing element (processing element) is strengthened by the following rule:

$$W_{i+1} = W_i + \alpha(X_i - W_i) \quad (4.5)$$

where α is a learning rate constant, W is the weight connecting input-output nodes and X is the input pattern, over a period of training step t .

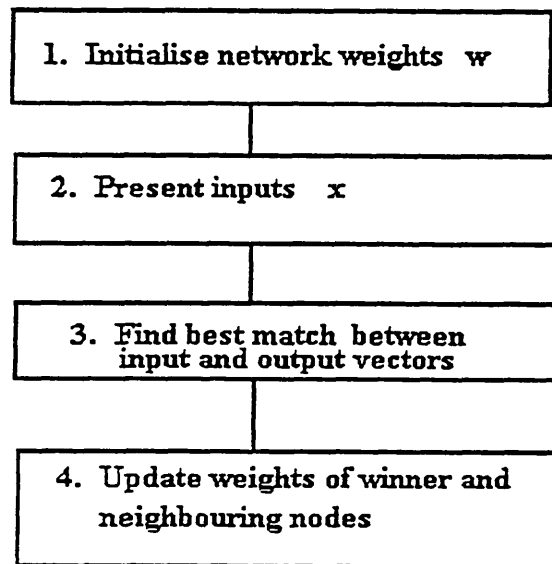


Figure 4.3. The Kohonen learning algorithm.

The action of the network is also said to behave in a "winner-take-all" competition where, given an input pattern, the output neuron with the weight vector closest to the input vector is selected as the winner. The winning node and its neighbouring neurons will modify its weight vector to align with the input vector.

The two very important parameters in the Kohonen network architecture are weight updating or learning rule and the topology of the neighbourhood neurons. The first parameter has been investigated by DeSieno [1988] and the second by Ritter et al [1992].

The next section will discuss the main experiments on the variants of self-organising maps and their learning algorithms with a view to adapting the network for flow identification from measured boundary data.

4.3.2 Learning parameters.

DeSieno [1988] developed a modification to the original Kohonen learning rule, which he described as conscience mechanism. He introduced a biased-competition amongst the output neurons (processing elements) such that the pe that has won will "feel guilty" and prevents itself from winning by exercising self-inhibition.

The goal of this mechanism is to bring all the pe's into the solution quickly by biasing the competition process so that each pe can win. The bias is chosen to be close to the $1/N$ probability desired for an optimal vector quantisation, that is, dividing the input vector space into N discrete, equiprobable regions where N is the number of neurons.

DeSieno achieved this by introducing these steps:

1. Find winning node i amongst neighbouring nodes j , using minimum Euclidian distance such that a winner is assigned unit value otherwise 0,

$$y_i = 1 \quad \text{if } ||W_i - X||^2 < ||W_j - X||^2 \quad \forall_j \neq i \quad (4.6)$$

$y_i = 0$, otherwise.

2. Develop a bias term for each pe based on the number of times it has won a competition:

$$p_{t+1} = p_t + B(y_i - p_t) \quad (4.7)$$

where $0 < B \ll 1$.

3. Then introduce a bias term b based on p, $b = C(1/N - p)$

Hence, a new biased competition is performed

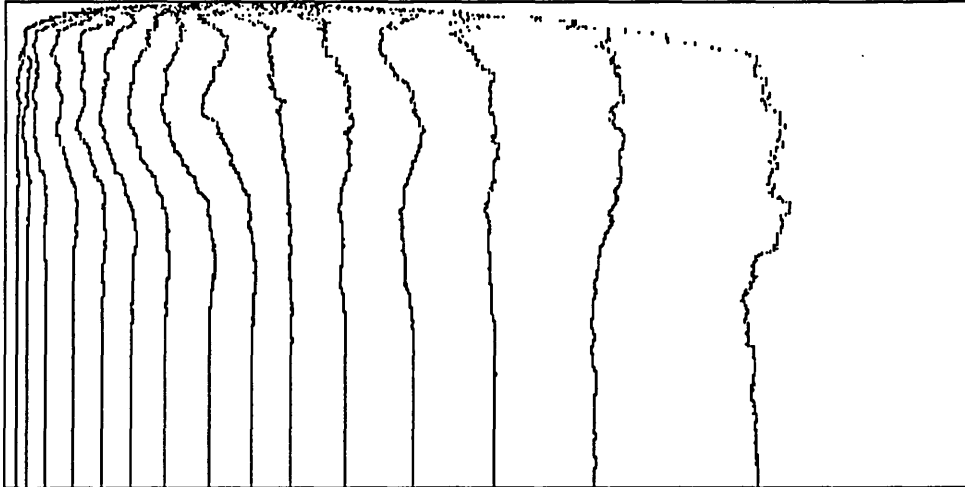
$$z_i = 1 \quad \text{if } |W_i - X|^2 - b_i \leq |W_j - X|^2 \quad \text{all } j \neq i \quad (4.8)$$

$z_i = 0$, otherwise.

4. Update the weights of the processing element winning this biased competition as follows:

$$W_i^{new} = W_i^{old} + A(X - W_i^{old})z_i \quad (4.9)$$

DeSieno's algorithm becomes the original Kohonen learning algorithm when the constant C is set to zero and is therefore a generalisation of Kohonen learning. In his experiments, DeSieno only updated the winning neuron.



```

count= 3200 sigma 0.01000 disorder = -0.00000 radius 0
w 7814 6134 5082 4238 3535 2972 2563 2123 1669 1320 1016 721 431 233 126
p 173 178 176 176 174 177 178 183 186 186 187 188 189 189 190
b 4928 4879 4902 4902 4922 4893 4882 4834 4805 4796 4787 4778 4769 4769 4760
q 203 209 207 207 205 208 209 214 217 218 220 220 221 221 221
press any key to go back to program

```

Figure 4.4. Change of weights on output neurons (15 nodes) with increasing training step in downward direction show 15 regions of equal probability. The weight w is adjusted by the bias term parameters p and b in (equation 4.7). The winning node frequency counter is q .

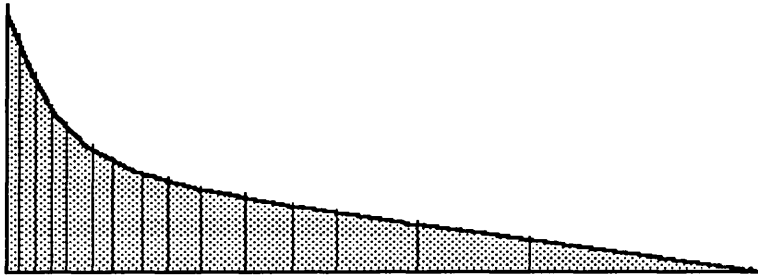


Figure 4.5. Probability density function showing regions of equal area under curve for an input consisting of the product of two random numbers. Each region is $1/N$, where N is the number of output nodes [DeSieno 1988].

Figure 4.4 shows the change in weights of each output neuron after 3000 training steps with an initial setting of 0.5. This shows the weights on the fifteen output neurons have formed fifteen regions that correspond to the $1/N$ regions of probability shown in figure 4.5. This demonstrates that the output neurons map the probability density function of the input pattern.

Ritter et al (1992) modified Kohonen learning by looking at how the neighbourhood pe's of a winning element are updated. They introduced a Gaussian-like function to update the weights of neighbouring pe's based on the distance from the winning pe, i.e.

$$W_r^{new} = W_r^{old} + \epsilon h_{rs} (X - W_r^{old}) \quad (4.10)$$

where $0 \leq h_{rs} \leq 1$ is a prespecified adjustment function of distance $|r-s|$ and ϵ is a learning step size. Then h_{rs} has its maximum at $r=s$ and decays to zero as $|r-s|$ increases. He chose

$$\epsilon_f = \epsilon_i (\epsilon_f / \epsilon_i)^{1/t_{max}} \quad (4.11)$$

where i and f are initial and final values over the maximum number of steps, t_{max}

$$h_{rs} = \exp(-||r - s||^2) \quad (4.12)$$

where r is the distance from the selected node, s .

This function is close to the Mexican hat shape (figure 4.6) without the negative dip and hence could also be called a Gaussian hat function. This function has the effect of cancelling out the inhibitive field and may produce erroneous results if used over a small network size. This problem is overcome by making sure the bell shape is symmetrical about the winning node.

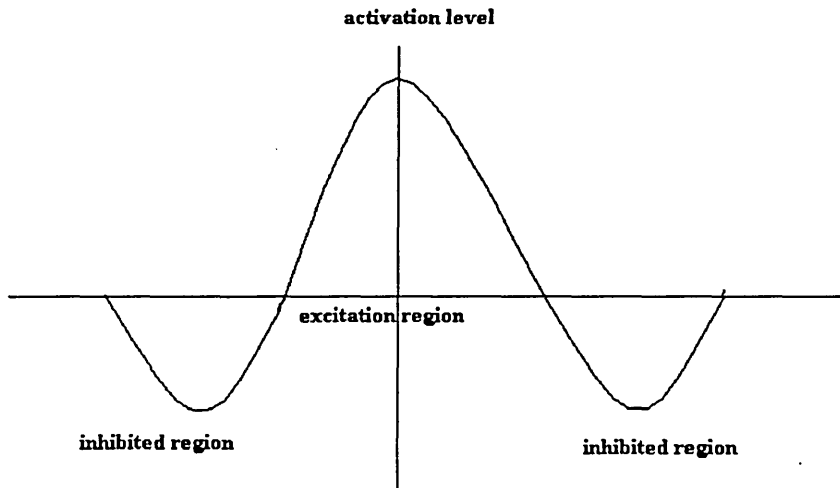


figure 4.6 Neural neighbourhood regions of excitation
and inhibition similar to a Mexican hat

Hence, incorporating both DeSieno's and Ritter et al's algorithms into the original Kohonen network, is convenient in representing the three important factors in Kohonen learning and allows experimentation on the parameters governing the performance of Kohonen learning:

1. learning rate of neurons
2. competition mechanism of neurons
3. neighbourhood update function

A study of the above parameters designed to investigate the Kohonen network performance with respect to accuracy and speed of convergence has been conducted. Eleven variations of the Kohonen learning rule consisting of different configurations of the 3 parameters were set up as shown in table 1.

Table 1: Variations of the Kohonen Network

Network Model	Variations of the Kohonen Network
1	K
2	C
3	K + H
4	K + L
5	H + L
6	C + H
7	C + L
8	H + L + C
9	H + L + N
10	C + H + N
11	C + N + L
Key: K = Kohonen; C = Biased Competition; N= Neighbourhood H = Gaussian Hat L = Exponential Learning	

The network used consists of a single layer output in one dimension, with 15 nodes on it. The reason for using a one dimensional layer is to demonstrate the closeness with which the Kohonen learning mechanism maps the input vector with a known probability distribution function, as used by DeSieno [1988].

The experiments were run for 15000 iterations for each network to allow for the slowest algorithm to be observed on the same scale. An empirical data set was used [DeSieno 1988]; a set of numbers which are products of two uniformly distributed random numbers.

The conscience mechanism parameters have values that was suggested by DeSieno. The function which the author chose to call a Gaussian hat function was originally used by Ritter et al[1992]. The initial decay and final values used were chosen after a few trials.

Accuracy was measured in terms of the mean squared error, defined as

$$\begin{aligned} error &= \text{sqr}(W_{calc} - W_{actual}) \\ MSE &= error / \text{no. of training} \end{aligned} \tag{4.13}$$

As shown in Table 2 and figure 4.7 networks 2,7 and 11 are conscience-mechanism networks combined with nothing (2), learning rate (7) and neighbourhood (10) functions.

The best result is the one from 10 with a marked speed of convergence of the neuron weights with input signal after 6000 iterations to reach a residual error of 0.03. The other two need more than 15000 training runs to converge to the same residual error.

Table 2: Ranking of results.	
Network	Error
10	0.0225
11	0.03
2	0.045
7	0.0525
3	0.33
5	0.33
6	0.33
8	0.33
9	0.6
1	0.75
4	0.81

This demonstrates the essential function of the neighbourhood around a winning node in determining a faster convergence. Low mean squared error means convergence is good and this is achieved in all three cases, which confirms the effectiveness of the conscience mechanism for good conversion of the weights with the input signal or vector.

The learning rate function used was exponentially decreasing with the number of training steps. Networks 4 and 7 show responses when this parameter was included in the Kohonen and conscience-mechanism learning rules. Network 5 is when the learning rate function is combined with a Gaussian hat function.

The result from network 5 is no convergence after the training period. The network 1, which is a pure Kohonen network, converges to about the same value as network 4 which means that the learning rate does not appear to be very significant. This is further supported from evidence between networks 7 and 2, which are conscience-mechanism networks with and without the learning rate function.

Network 11 is a network with the learning rate and Gaussian hat functions applied to the conscience-mechanism rule. The reason why only the conscience-mechanism is tested with this combination is because the Kohonen network is already shown to have a much slower convergence than the former.

Network 10 has the learning rate removed. The results of the simulation showed similar residual errors were achieved after the same period of training which only confirms the view that the neighbourhood function is the dominant determining factor in good performance.

Networks 3, 5 and 6 are embedded with Gaussian hat functions. It is found that none of them converge. This is because the Gaussian hat function runs the excitation field over the whole network layer and is contrary to the biologically known existence of an inhibitive field.

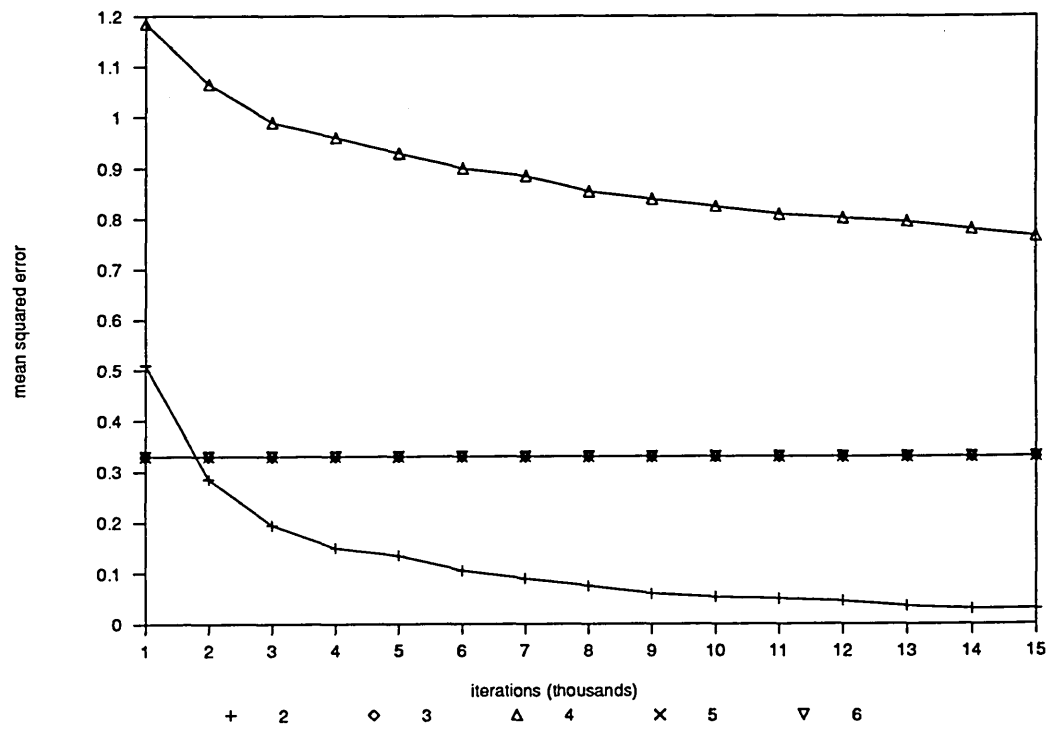


Figure 4.7a.

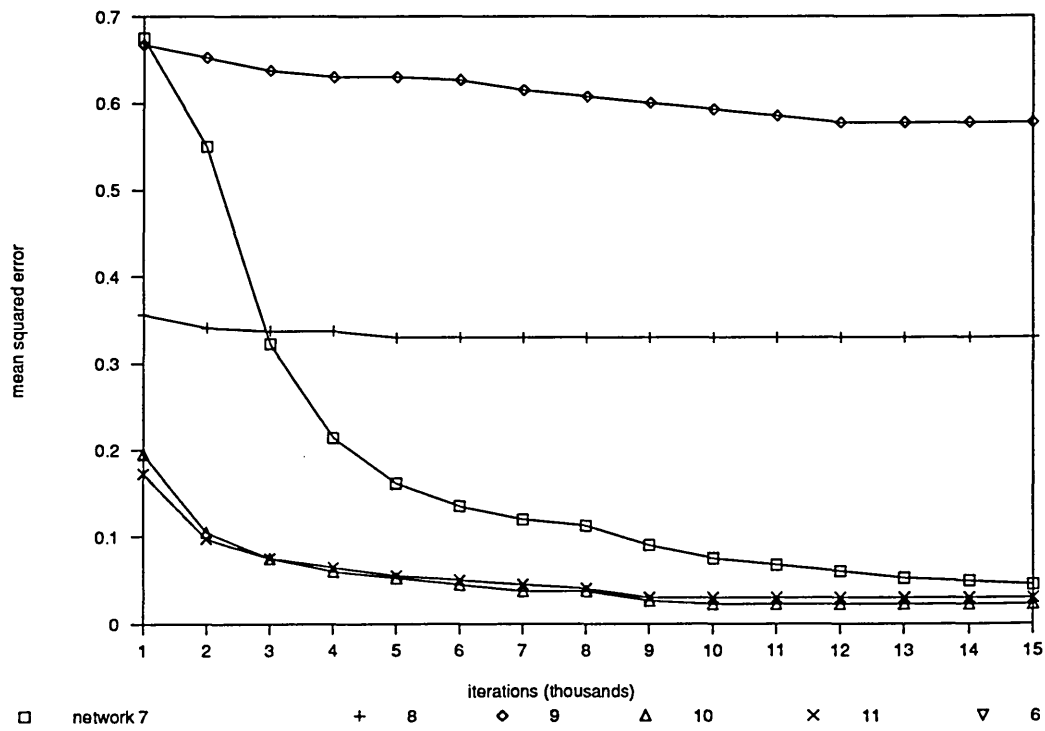


Figure 4.7b.

Figure 4.7. Accuracy and convergence of networks (labelled in legend) for 15,000 training steps.

4.3.3 Classification maps.

A set of experiments was designed to see the performance of four networks on mapping two-variable input patterns. The networks are based on the following mechanisms:

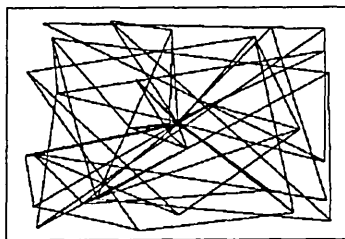
1. Conscience-mechanism
2. Symmetric neighbourhood Gaussian Hat
3. Kohonen
4. Modified Conscience

The objective of the experiments is to investigate the mapping capability of the Kohonen-type networks for high dimensional data. The kind of input pattern used is the type that is expected from process tomography measurements that are dependent on one another due to the laws of Physics. Hence these experiments are useful in giving an insight into how to adapt the networks for flow identification and image reconstruction.

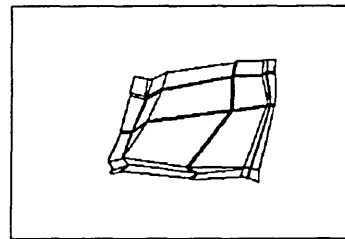
A two dimensional input pattern consists of randomly generated numbers from a uniform distribution of the following type, $x[1] = a$ and $x[2] = b$.

For each network the three input pattern space were applied. A training cycle of 10000 was used in each experiment. The output from each pattern is presented in such a way as to show how the two-variables in the input pattern are connected or related to each other. Hence this gives an indication of the network's capability to copy a given input pattern of known relationship between variables.

The performance of the four networks are shown in figures 4.8-11 for training periods of 2000, 4000, 6000, 8000, 10000 respectively.



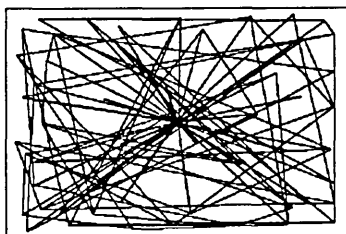
press return to continue



press return to continue

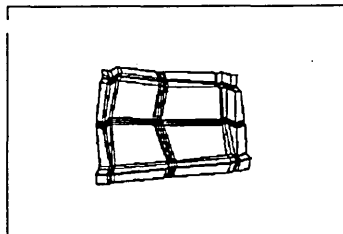
Figure 4.8a. 2000 training steps.

Figure 4.9a. 2000 training steps.



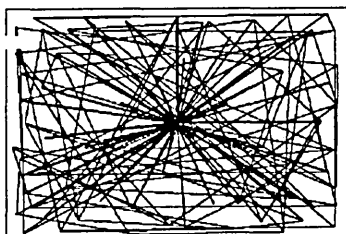
press return to continue

Figure 4.8b. 4000 training steps.



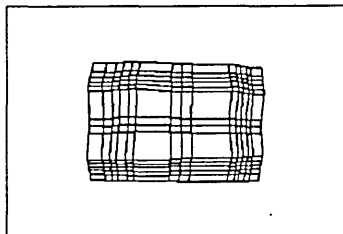
press return to continue

Figure 4.9b. 4000 training steps.



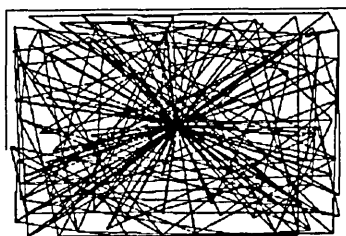
press return to continue

Figure 4.8c. 6000 training steps.



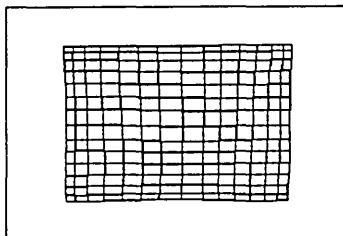
press return to continue

Figure 4.9c. 6000 training steps.



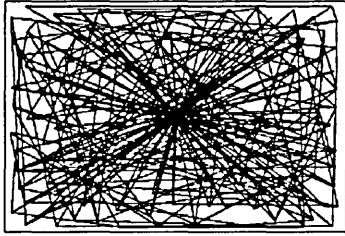
press return to continue

Figure 4.8d. 8000 training steps.



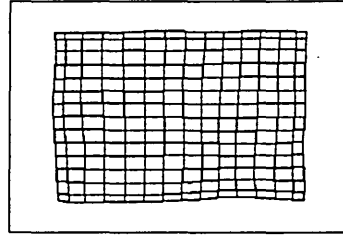
press return to continue

Figure 4.9d. 8000 training steps.



press return to continue

Figure 4.8e. 10000 training steps.



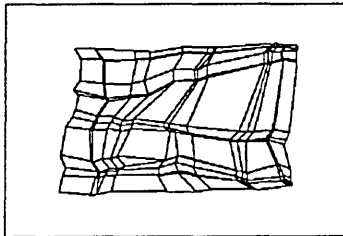
press return to continue

Figure 4.9e. 10000 training steps.

Figure 4.8. Conscience network training.

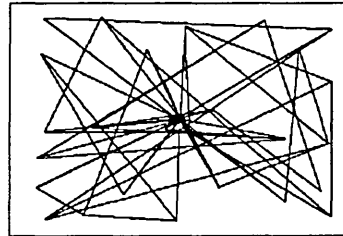
Figure 4.9. Gaussian-hat network training.

The maps in figures 4.8-11, show the distribution of weight vectors connecting neighbouring nodes. Vertical axes correspond to input values from the first input node and horizontal axes with the second. The variation of the map shows how weight values respond to each input over periods of training corresponding to 2000, 4000, 6000, 8000, 10000 learning cycles.



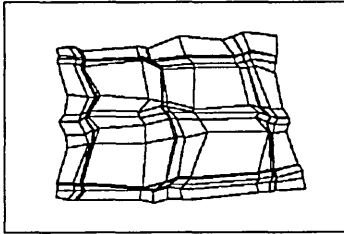
press return to continue

Figure 4.10a. 2000 training steps.



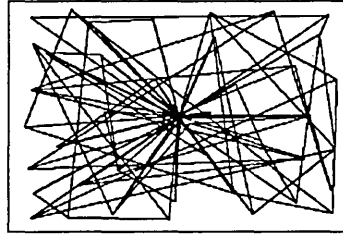
press return to continue

Figure 4.11a. 2000 training steps.



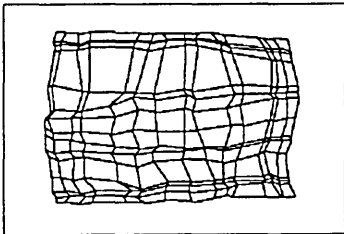
press return to continue

Figure 4.10b. 4000 training steps.



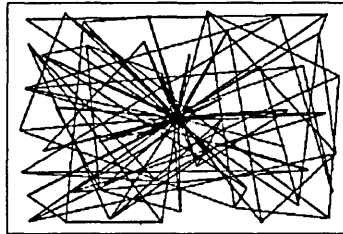
press return to continue

Figure 4.11b. 4000 training steps.



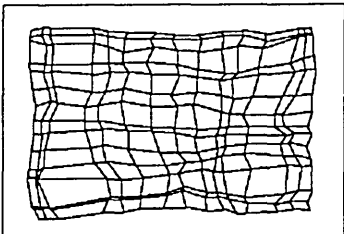
press return to continue

Figure 4.10c. 6000 training steps.



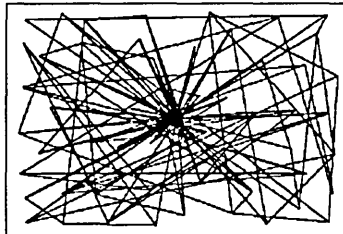
press return to continue

Figure 4.11c. 6000 training steps.



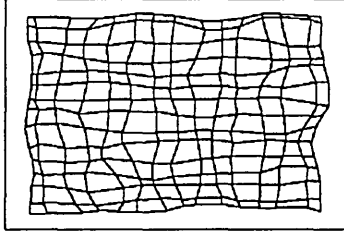
press return to continue

Figure 4.10d. 8000 training steps.

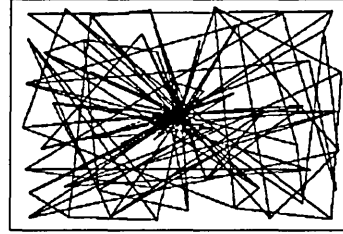


press return to continue

Figure 4.11d. 8000 training steps.



press return to continue



press return to continue

Figure 4.10e. 10000 training steps.

Figure 4.11e. 10000 training steps.

Figure 4.10. Response of output nodes for a Kohonen network.

Figure 4.11. Response of output nodes for a composite network.

The conscience network (figure 4.8) fails to map the input, as does the composite network (figure 4.11). The weights tend to cluster around the middle nodes on the output map. The Gaussian hat network (figure 4.9) performed better than the unmodified Kohonen network (figure 4.10) although the latter also map the input patterns successfully. These observations show a significant relationship between the mapping performance and the parameters of the network, namely the neighbourhood definition and the learning or weight updating mechanism.

The results show that the Gaussian hat neighbourhood helps to improve the Kohonen network. The control of this neighbourhood update, by increments based on a Gaussian function, is a close resemblance to the biological phenomenon, where there is a region of excitation near an activated neuron and an inhibition region away from that neighbourhood [Grossberg 1982].

The biased competition modification to the original Kohonen does not show any improvement, even when combined with the Gaussian hat neighbourhood in the

composite network (figure 4.11). Based on the experiments with a one-dimensional input, this result shows a weakness in the conscience mechanism for higher dimensional mapping. This is probably due to ordering of the nodes [Kohonen 1984] being a significant factor to achieve correct mapping. The mathematical proof of this observation is not in the scope of this research.

4.3.4 Regime identification from synthetic data.

An experiment was designed to test the performance of the neural network program in recognition of flow regimes. Experience using these artificial regime data would later be used for classification of flow regimes from experimental measurements.

The flow regimes are represented by threshold binary values so that where a sensor detects flow near it then a unity value is assigned, otherwise zero. The respective data representations are shown in figure 4.12. Three classes of regimes are to be identified by the neural network - full, half and stratified flow regimes. The training data consists of three data patterns which the network is trained to recognize over 5000 iterations.

The results of using test data show 100% success for clean signals, 100% for signals with 10% noise and 87.5% for signals with 20% noise. The noise term is introduced by inverting the values of the channels. For instance, a 10% noise would be two channels out of the sixteen being inverted randomly. Success rate is a measure of the correct identification of the signals tested.

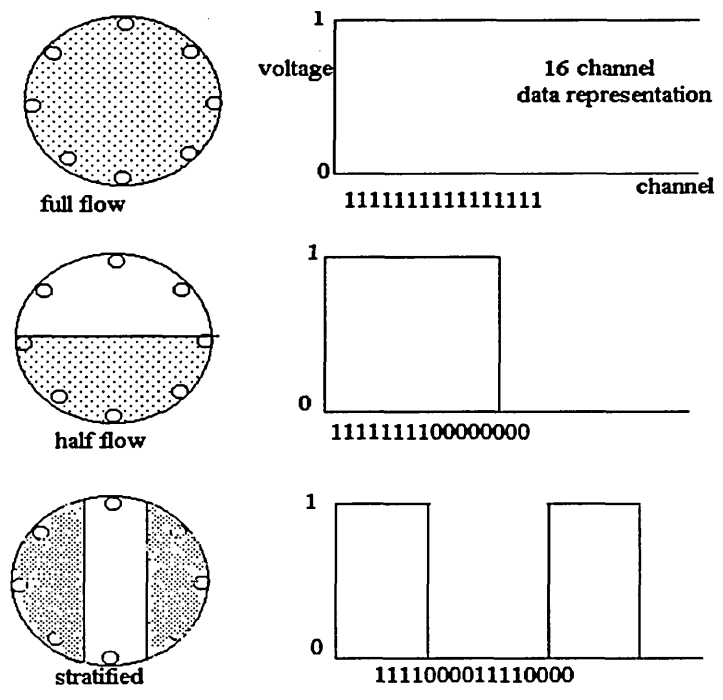


Figure 4.12. The data representation of artificial flow regimes.

Chapter 5

The Measurement System.

5.1 The transducer.

In electrodynamic sensing, the space charge due to the electrification of the conveying material induces a charge onto the electrodes. The location of the sensors on the circumference of the conveying pipe is non-intrusive to the flow. The electrodes are passive and should not disturb the electric field due to the net space charge carried by the flowing particulates.

The transducer system consists of two basic components: a 3mm, zinc-plated screw electrode as sensing device and the signal processing electronics. The connection between the screw sensor and the input to the buffer amplifier uses a driven guard technique (figure 5.1). In this way the effects due to stray capacitance is minimised and the sensitivity of the output measurement is ensured.

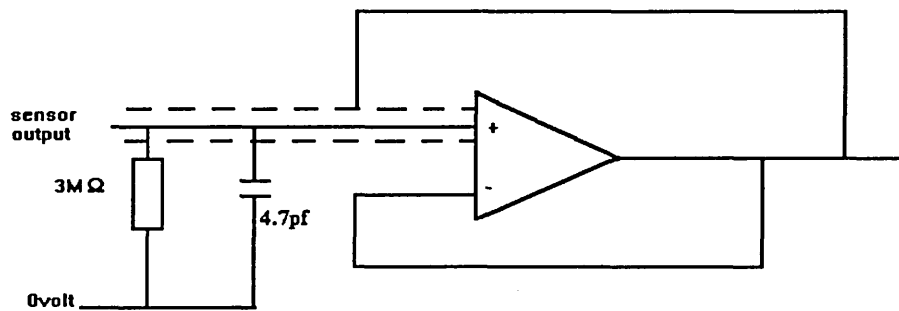


Figure 5.1: The transducer.

The particle size of the sand used in this work is mainly (50%) 300 μ m. The maximum amount of charge that a round, smooth particle of this size range will carry, is estimated by Shackleton [1981], to result in a voltage at the sensor in the order of 10^{-5} volts. The oscilloscopes and data acquisition system gave readings that were within the level of sensitivity required (100 mVolts). A complete measurement system would require higher gain amplifiers with ac coupling to cancel the dc offset.

The diameter of electrode used has an effect on the amount of charge induced on the transducer. The diameter used is 3mm and it is hemispherical in shape. The effects of electrode size have been investigated by Gregory(1987) and Beck(1986).

An approximate estimation of the frequency bandwidth of the signal may be obtained by assuming the particle only induces charge as it passes by the sensor,

$$T = \frac{d}{v} \quad (5.1)$$

for a particle small compared with the diameter d of the sensor (diameter of sensing area 3mm). The period of the signal is T and v is the particle velocity (5 ms⁻¹). For a larger particle the period T in this model will be increased due to the axial length l of the particle to

$$\text{Total time} = \frac{d}{v} + \frac{k \cdot l}{v} \quad (5.2)$$

where k is a modifying factor due to the charge field. Hence, the frequency of the signal is 265 Hz ($f = \frac{1}{2\pi T}$). Basically, the frequency is inversely proportional to the sensor diameter and directly proportional to the velocity of particle.

5.2 The 16-channel circular array sensor configuration.

Small electrodes, apart from being cheap and simple to construct, give discrete data from points around the circumference of a pipe. Sixteen electrodes (figure 5.2) are used in the measurement system, which means the data sampling has to be fast in order to determine simultaneously the boundary voltages at all the sensors, due to the charge on the flowing particle. A photograph of the sensor system is shown in Photo 1.

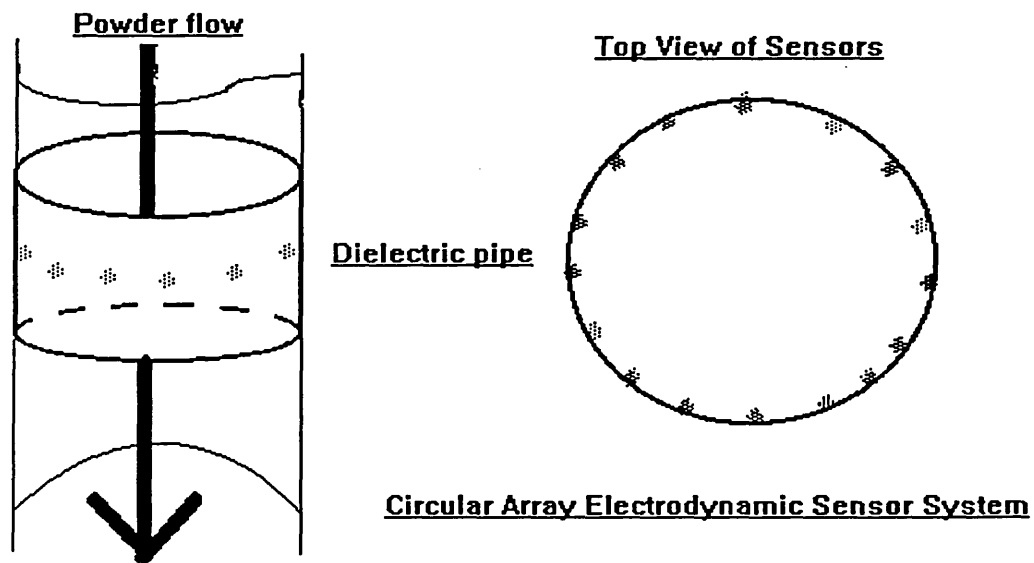


Figure 5.2. The sensor geometry.

In order to determine the velocity of the travelling particles, a cross correlation technique is adopted. By having two points, one upstream and the other downstream, separated by a half a pipe length, it is possible to determine the correlation between them (section 4.2, figure 5.3). The time delay between the signals from the two sensors is the time for the source of the signal to travel from one point to the other. Since the distance and time are known, the velocity can be determined in this manner [Beck and Plaskowski 1990].

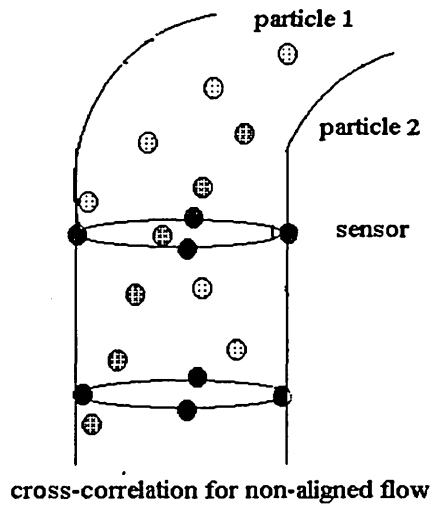
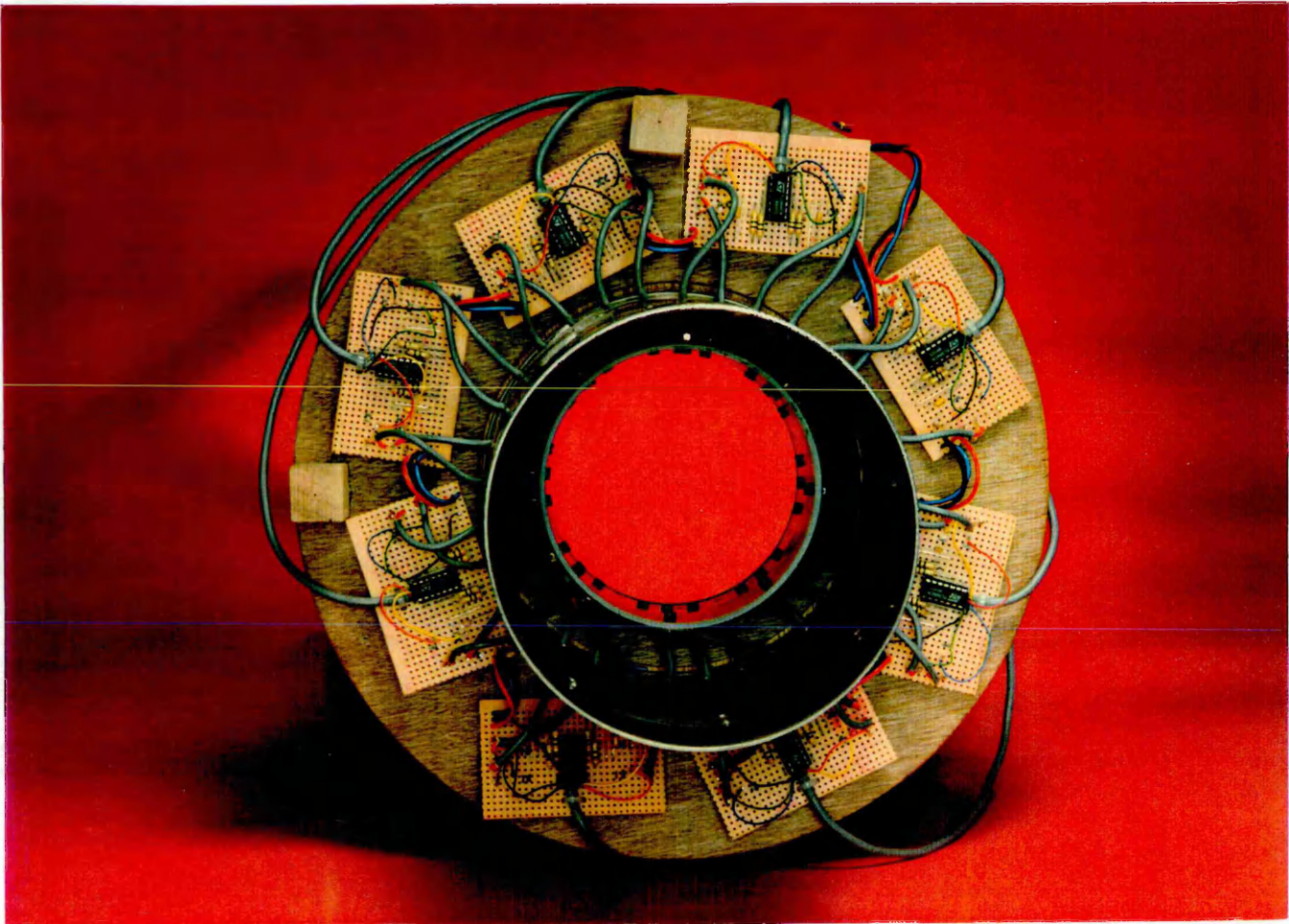


Figure 5.3. Cross correlation sensors positioned to investigate velocity distributions.

This work finds the cross correlation between eight points around the circumference of the conveying pipe with the corresponding eight points on a plane downstream of the axis of the pipe. These cross correlations enable a velocity profile near the boundary of the flow to be determined.

Photo 1. The electrodynamic sensor system



5.3 Data acquisition system.

The data-acquisition system is a Strawberry Flashcard12 data logging card with 16 input channels and 1 MHz sampling capability mounted in a PC. This is interfaced to data-acquisition software called Workbench V2.01 [Strawberry 1991]. The sensor outputs are interfaced to the data-acquisition system via analog input-output boards (figure 5.4).

16 channels are used and the maximum sampling rate per channel is 62.5 KHz. However, a 2KHz sampling rate is sufficient because the signal bandwidth is about 400Hz. The event captured is, in the bead case, a single fast event and in the sand-flow case, a continuous and noisy flow event. The software used is also limited in DMA access so only a maximum of 64K data could be captured.

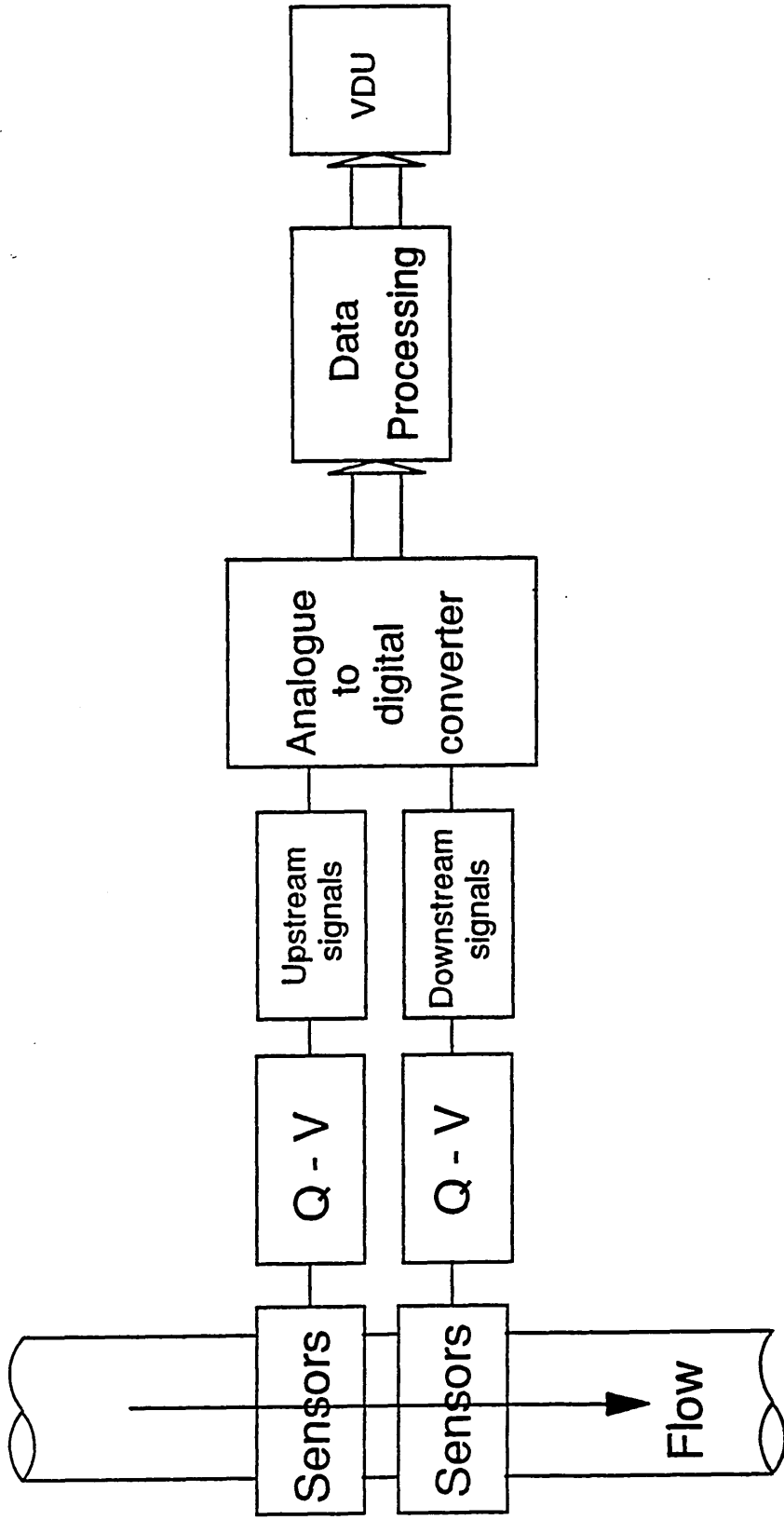


Figure 5.4 : The data acquisition system.

5.4 Signal processing software.

The software used for signal processing is called DaDisp v1.0 [1988]. This software is used for display and analysis of flow voltage profiles. A qualitative profile of the flow is produced. Figure 5.5 shows a typical data set for 16 transducers for a test using a single charged particle.

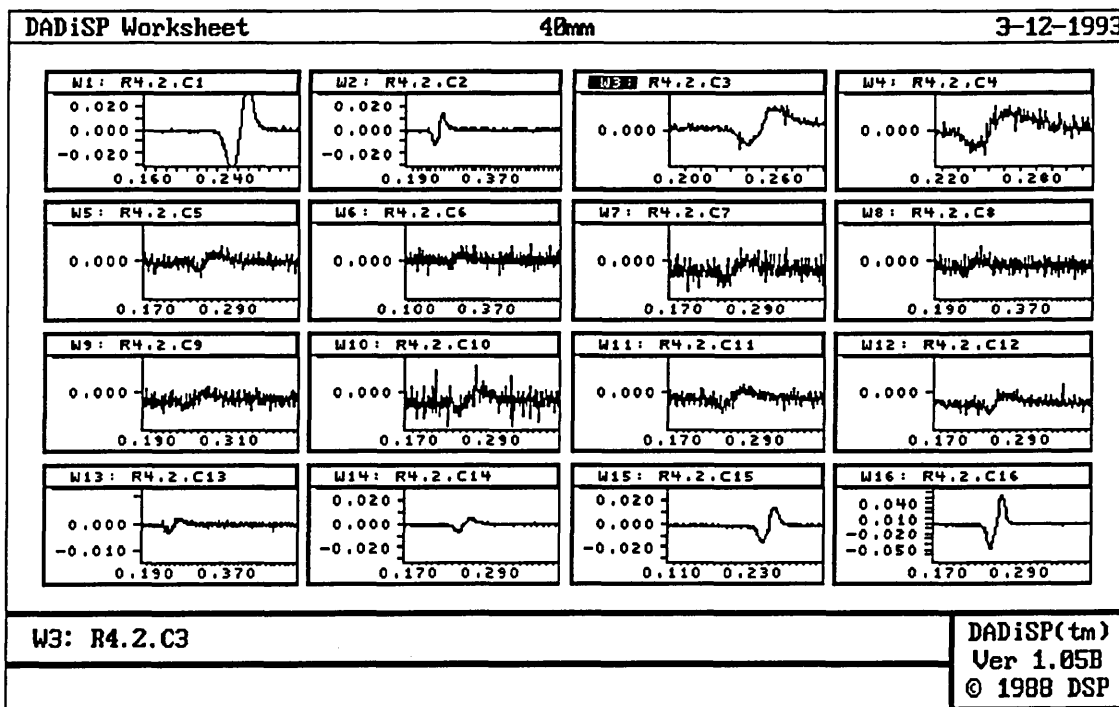


Figure 5.5. Typical display of 16 channels from the data acquisition system.

5.5 The bead flow rig.

An experimental rig is designed to investigate which model best simulated the phenomenon of induced potential on the electrodes. A bead made from plastic material is pre-charged by rubbing on wool and immediately dropped through a narrow 10mm non-conducting tube which guides the path of the particle through a PVC pipe of 100mm

diameter which acts as a measurement chamber. The pipe wall is mounted with 16 electrodes (3mm screws) located at equally spaced positions around the pipe wall in order to obtain a profile of the voltages on the boundary sensors. The measurement chamber is surrounded by a concentric earth screen. Figure 5.5 shows a schematic diagram of the experimental set up.

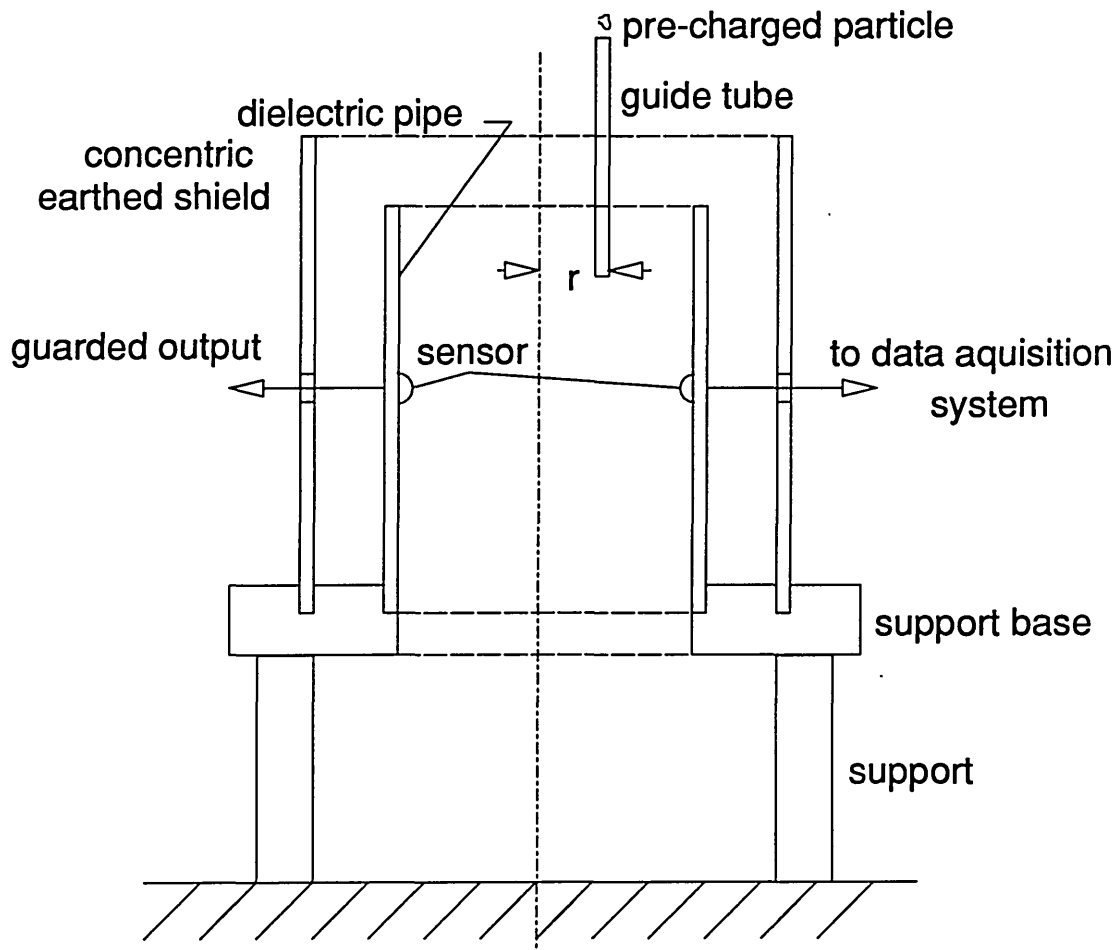


Figure 5.6 : The experimental rig for bead flow measurements.

The guide tube is clamped in a vertical position, above the sensing volume of the measurement chamber, by slipping it through a tight-fitting hole on a perspex lid designed

to sit on the pipe section. Several holes are made at fixed locations along a chosen radial axis so that the axial location of the bead passing through them is known. These holes are positioned relative to the centre at 0mm, 15mm, 22.5mm, 30mm and 37.5mm. On a dimensionless scale they are at locations 0, 0.3, 0.45, 0.6 and 0.75 from the centre of the pipe.

5.6 The sand flow rig.

The sand flow rig consists of three subsystems: a sand hopper, a screw feeder and a vertical pipe section. This is a batch, gravity conveying system and therefore sufficient amount of sand for a set of trial runs is required. The sand used has a mean size of 300 micron. The particle size distribution of sand is shown in figure 5.7.

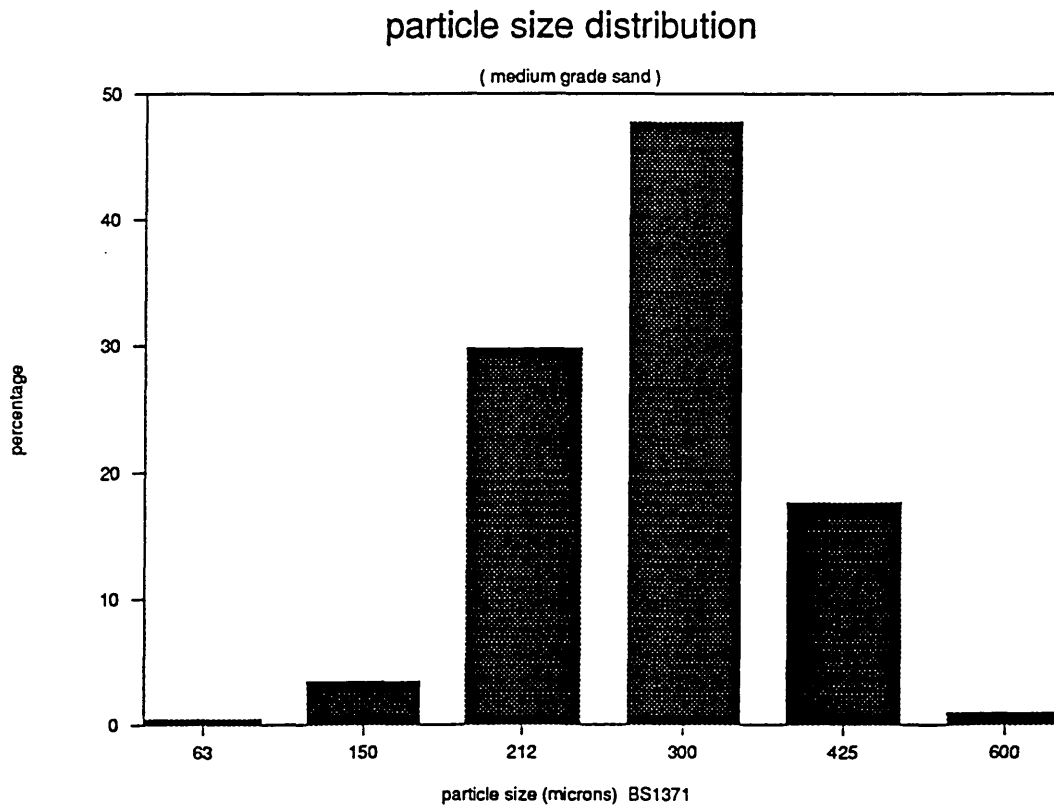


Figure 5.7. Particle size distribution of sand.

The sand flowrate is controlled by a screwfeeder whose speed of rotation is set by the control unit. A calibration of the actual mass flowrate and screwfeeder set rate is established by the collection of running sand over recorded time. The result of the calibration is shown in the graph in figure 5.8.

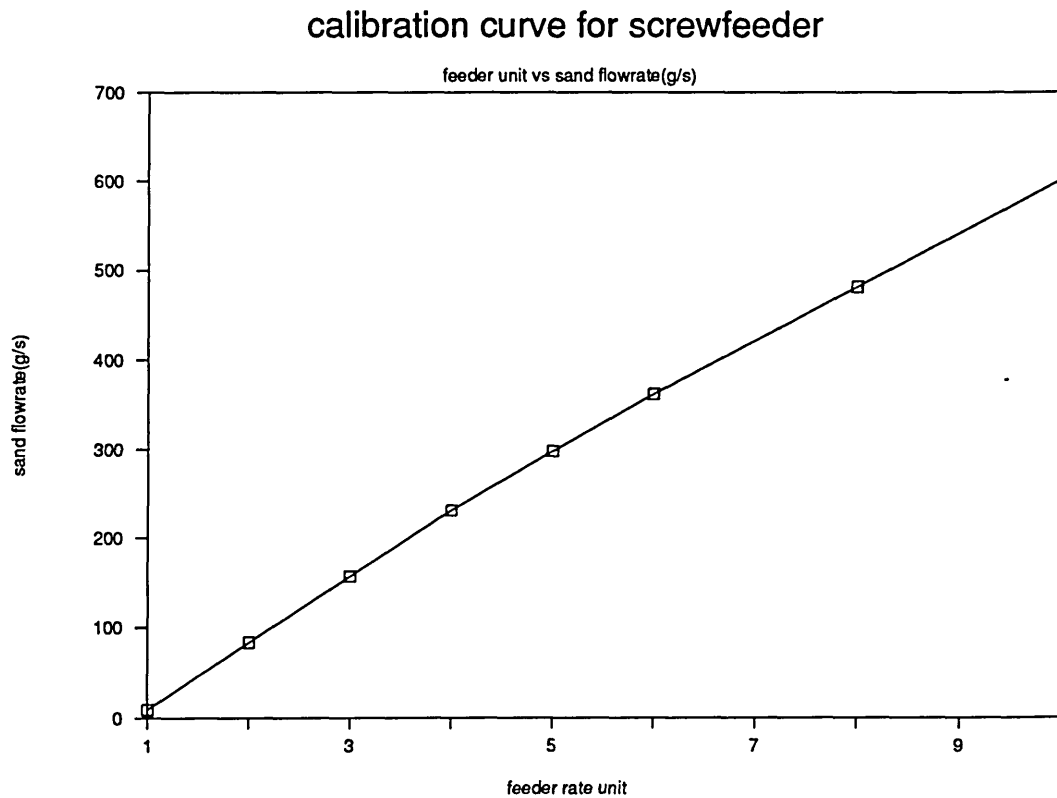


Figure 5.8. The calibration of the sand flow rig.

The screwfeeder does not give a uniform distribution of the sand over the cross-section of the pipe, the feed being richer near to the hopper side of the feeder screw. However,

as the results of the experiments (section 6.2) show, the transducers are sensitive to this uneven distribution which reinforces the concepts of the measurement system being used to discriminate concentration profiles.

The vertical pipe is of length 1.4m and diameter 100mm. The pipe exit nozzle may be fitted with baffles of different shapes to produce a range of flow regimes (section 5.7).

Because this system is based on gravity drop, the velocity of the volume of sand at a particular height can be estimated and compared with the measured velocity. Measurements by the transducer system are also checked in this way.

5.7 The flow models.

The system available is a batch system. A technique to artificially create flow regimes is devised by placing various shaped baffles in the path of the oncoming sand flow (figure 5.9). These baffles are effectively obstacles.

The regimes created and tested are:

1. Full flow.

This is generated by not putting any obstacle so that a full continuous flow is obtained.

2. Half flow.

This is created by the baffle blocking half the pipe diameter so that the other half will be clear for sand flow (figure 5.9).

3. Stratified flow.

A pyramid shaped baffle splits the pipe cross-section into two regions with flow on the sides but not through the middle, creating a pseudo-stratified flow regime.

4. Channel flow.

This is created by placing two pyramid shaped baffles in parallel which split the flow path into three regions.

5. Annular flow.

A cone shaped baffle in the middle of the flow path allows the sand flow by the sides and a ring or annular flow is generated.

6. Core flow.

This is the inverse case of the annular flow in that the sand is allowed to flow only through the middle of the pipe by placing a funnel in the flow path.

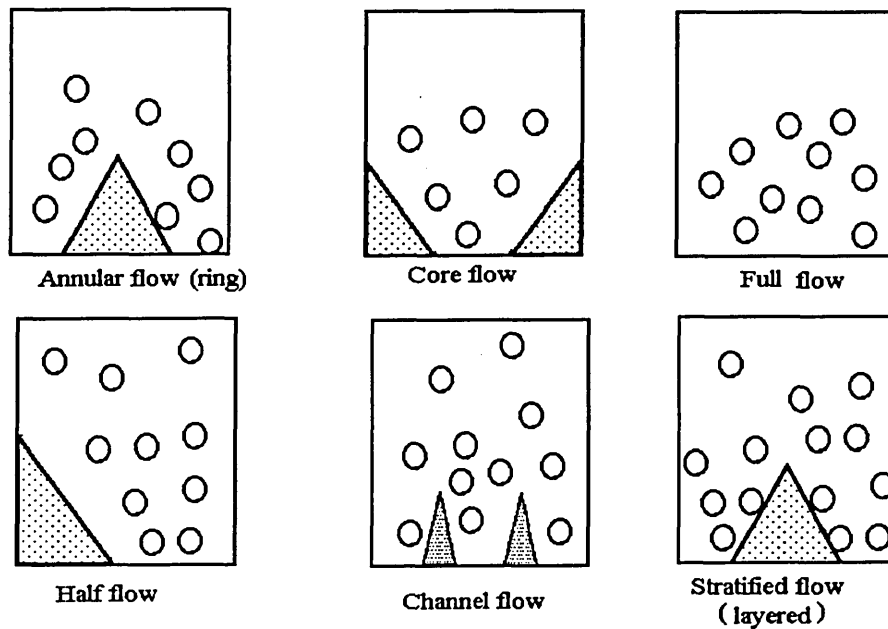


Figure 5.9 Diagram of baffle configurations for generating flow regimes.

Chapter 6

The Experiments and Results.

6.1 Introduction.

Three experiments are conducted:

1. to measure boundary voltages for the bead flow,
2. to measure boundary voltages for the sand flow,
3. to determine the velocity of sand flow by cross correlation.

From these measured data, other measurements are derived:

4. frequency spectra from flow signals,
5. flow regime patterns.

This chapter presents measured results as the primary data of the experiments. The extraction of secondary data by analysis are presented in the next chapter.

6.2 Single particle flow experiment.

The experiment using a bead is performed with two measurement systems:

1. The oscilloscope connected directly to the buffer amplifiers, and
2. The data acquisition system.

6.2.1 Bead flow measurements by oscilloscope.

The procedures of the experiment are as follows:

1. Rub the bead with wool several times.
2. Drop the bead through the guide tube held firmly at prespecified radial locations, along the vertical axis of the pipe.
3. Observe the response on the display and freeze the screen when peak voltages appear about the middle of the screen.
4. Take measurements for each channel by determining the peak amplitudes of the voltage recordings.
5. Repeat procedures 1-4 for other tube positions.
6. Repeat procedures 1-5 to ensure repeatability.

The peak voltage of each channel response is displayed and measured from the oscilloscope. The peak voltage is proportional to the strength of the induced charge on each sensor. The strength of the induced charge depends on the initial charge of the bead as well as the sensor to bead distance.

The data is processed statistically by determining the mean and standard deviation of the peak voltages. These values are used to plot the voltage profile of the pipe boundary. Normalised values are used as explained in section 3.2.2, as the charge on the bead is never the same in each run.

The results are plotted on special graphs (figure 3.4) where the predicted profiles are already plotted. The results are plotted in such a way that the sensor with maximum

value is fixed as the reference sensor at $\theta=0$ and the readings from the other sensors are then plotted on the graph in a cyclic manner. A typical result is shown in Figure 6.1.

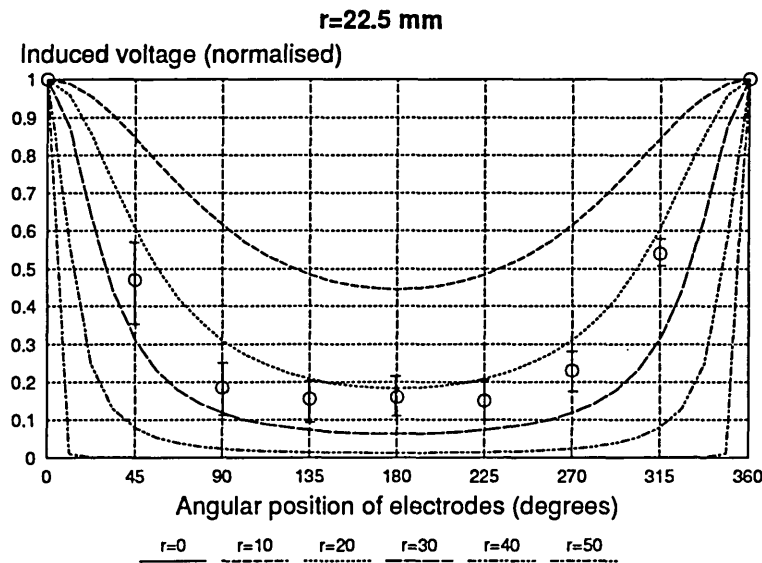


Figure 6.1 A typical result for bead flow at a specified spatial point.

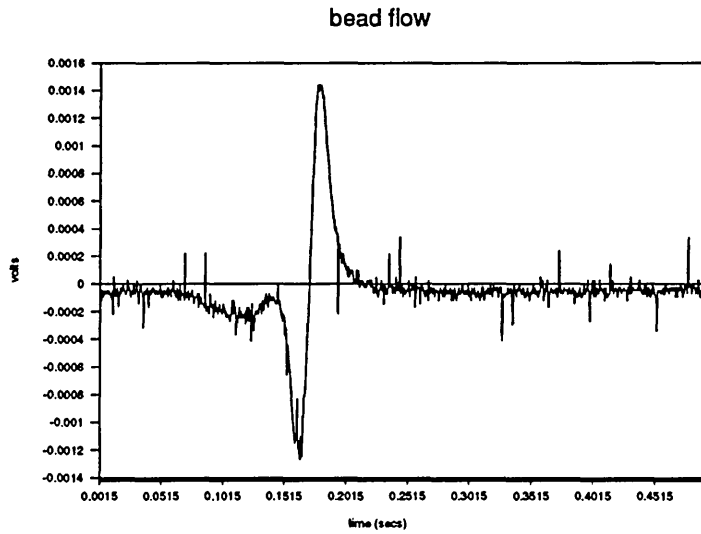
6.2.2 Results using the data acquisition system.

The procedure for the above experiment is repeated using the data acquisition system.

6.2.2.1 Sensor response in time domain.

A typical response of the electrodynamic sensor to a moving, charged bead, is presented in figure 6.2. The amplitude of this measurement depends on the total amount of charge carried by the bead and its distance from the sensor.

Figure 6.2. Response of a sensor to charged particle flow.



6.2.2.2 Spatial profile from sensor output.

The response from each sensor is normalised (section 3.3.2) and the following plots are obtained for different spatial positions of bead drop through the pipe (figure 6.3).

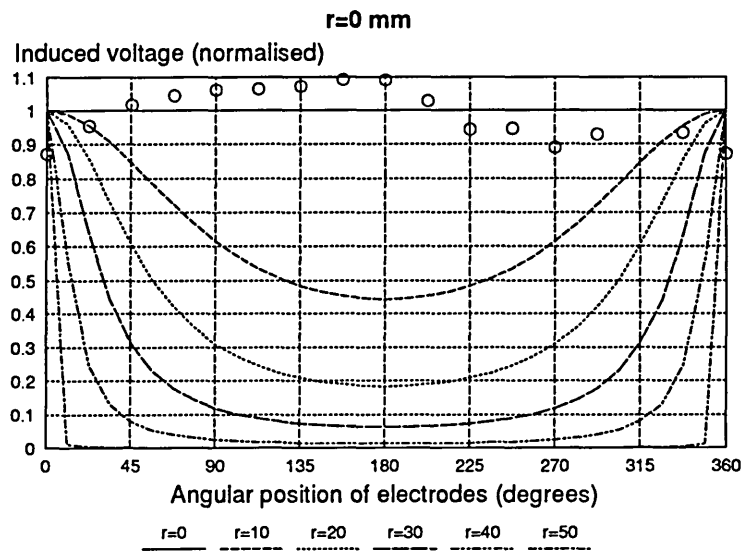


Figure 6.3a Bead flow through centre of pipe, radius $r=0$.

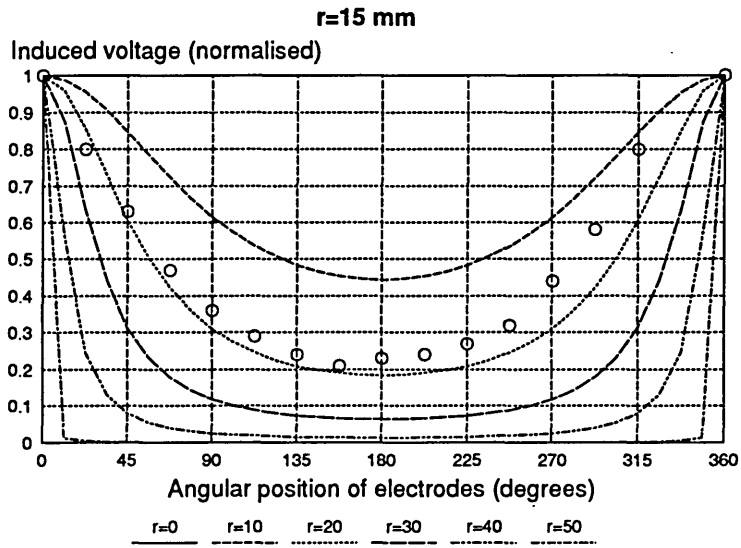


Figure 6.3b Bead flow through r=10mm of pipe.

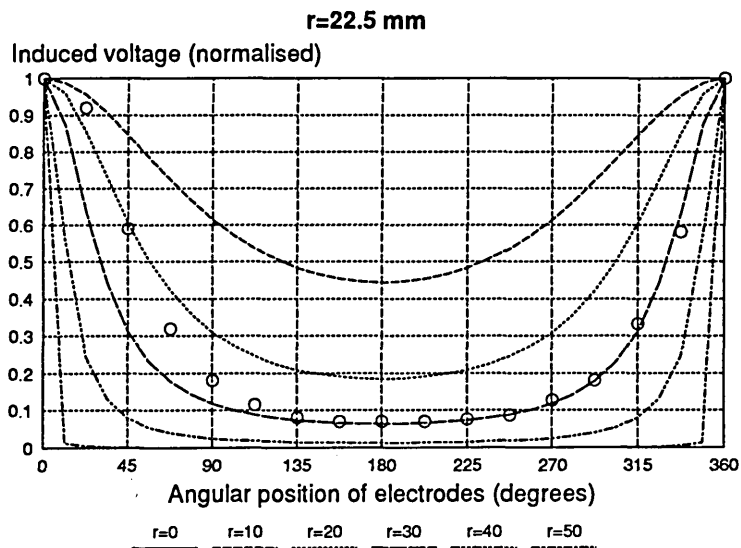


Figure 6.3c Bead flow through r=22.5mm of pipe.

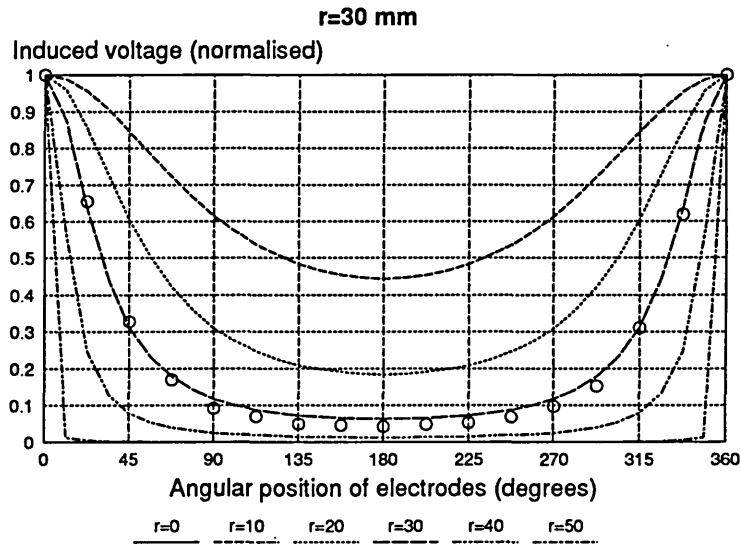


Figure 6.3d Bead flow through r=30mm of pipe.

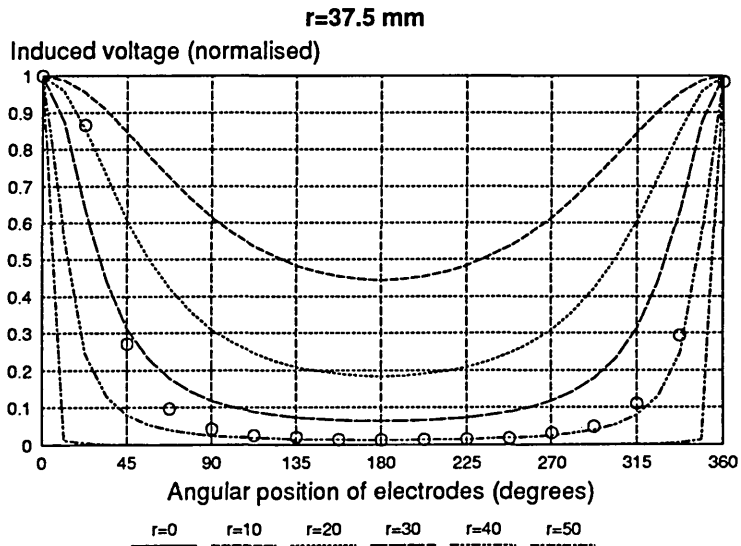


Figure 6.3e Bead flow through 37.5mm of pipe.

The results show reasonable agreement with the induction model (section 3.2.2).

6.3 Boundary voltage measurements of sand flow.

6.3.1 The procedures.

In the multi-particle flow experiment, the sand flow rig discussed in sections 5.7 and 5.8 is used. The experimental procedure is to measure the sensor signals using the data acquisition system for a range of flowrates, for each artificially created flow regime.

6.3.2 Sensor response to flow noise.

Typical responses from the sensor system when sand particles flow past are shown in figure 6.4.

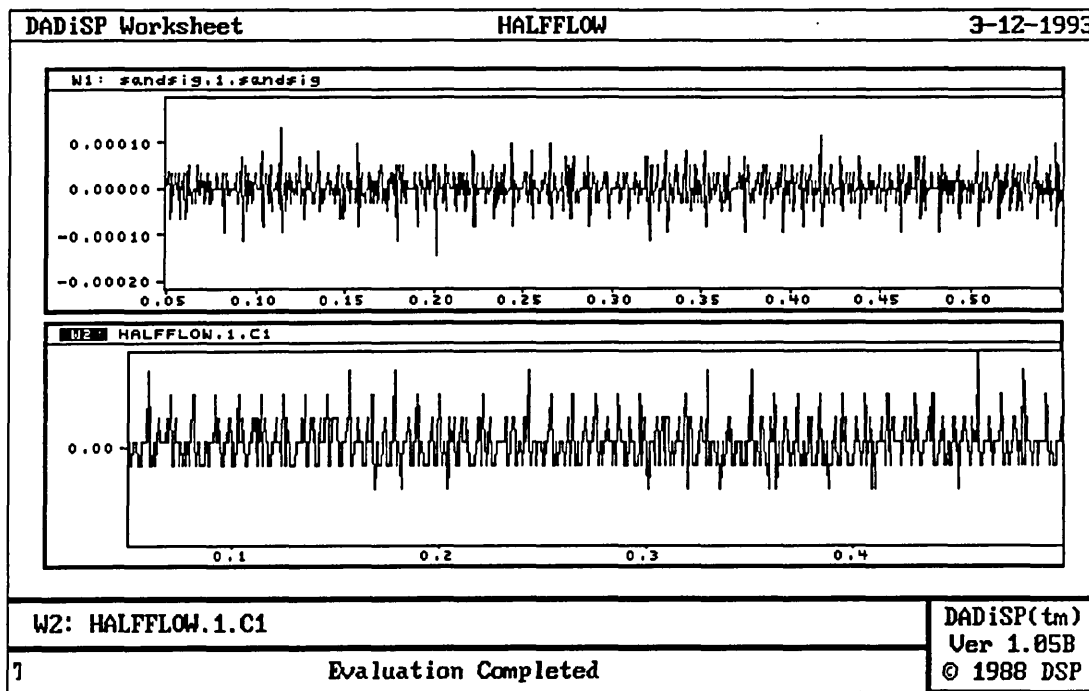


Figure 6.4. Sensor response to flow noise shown for two channels.

The readings from each sensor are time averaged and the results show consistency over the duration of a test (figure 6.5).

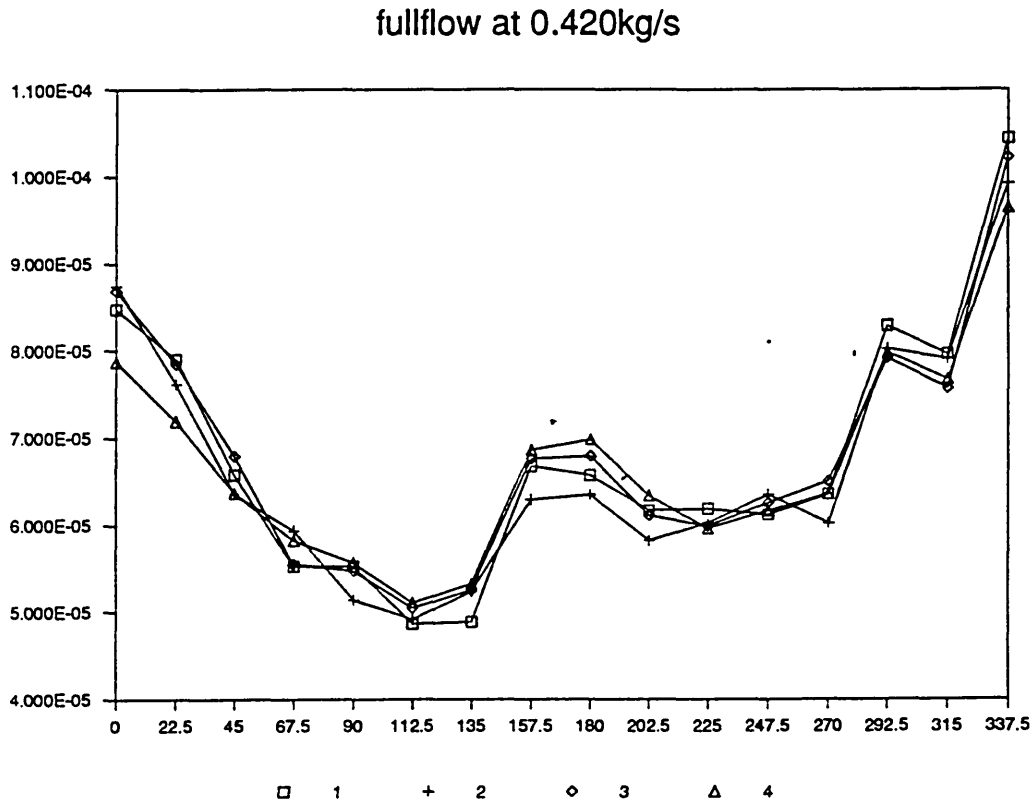


Figure 6.5. Voltage profile of full flow for 4 averaged values.

6.3.3 Flow regime profiles.

6.3.3.1 Full flow

The results summarised in figure 6.6 are for the full flow regime measurement. They show higher readings between 315° and 45° which indicates the presence of a greater flow of sand particles in this region of the pipe. Lower readings between 45° and 135° correspond to less sand particles flowing. The way the sand particles are

delivered by the screwfeeder causes this lopsided delivery of sand particles.

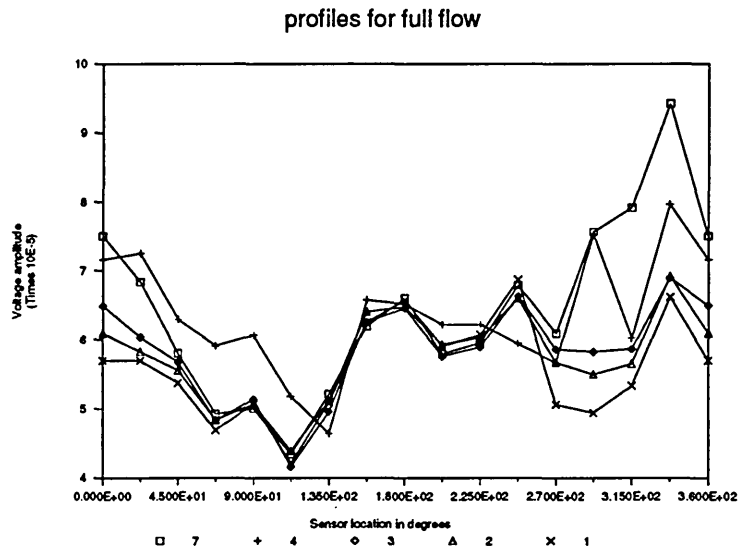
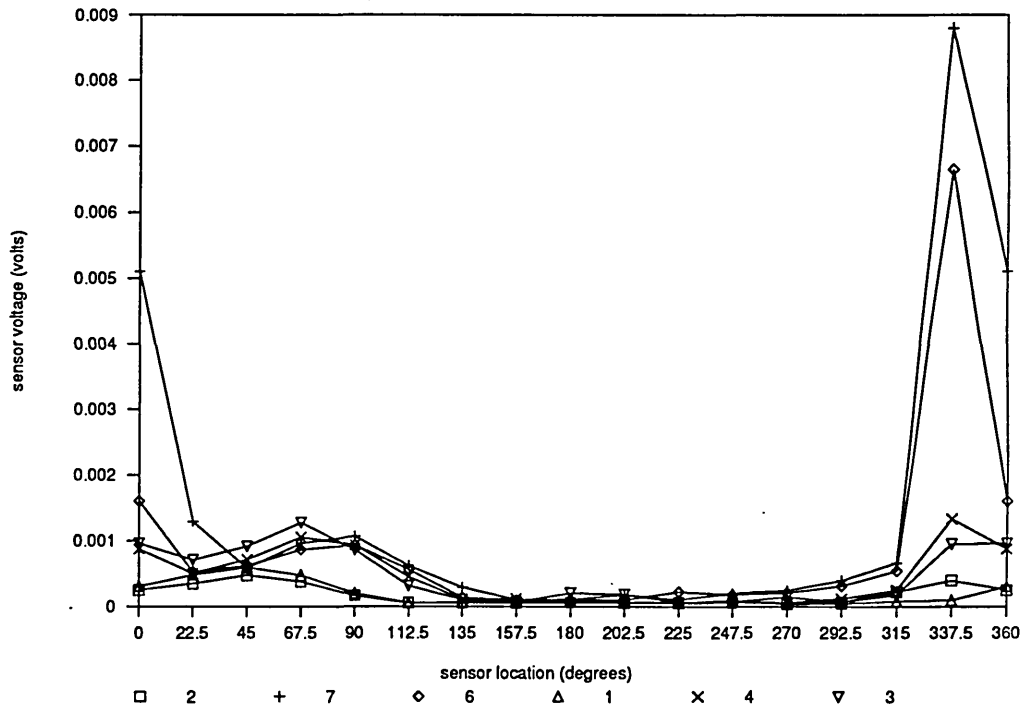


Figure 6.6. Voltage profile of full flow for different flowrates.

6.3.3.2 Half flow

The readings in figure 6.7 are produced by sand particles flowing in the clear half of the pipe, the other half being blocked by the designated baffle (section 5.6). It shows a clear pattern of a profile where between 292.5° and 112.5° the readings are increasing with flowrate. However, between 135° and 270°, little change of amplitude with flowrate is observed.

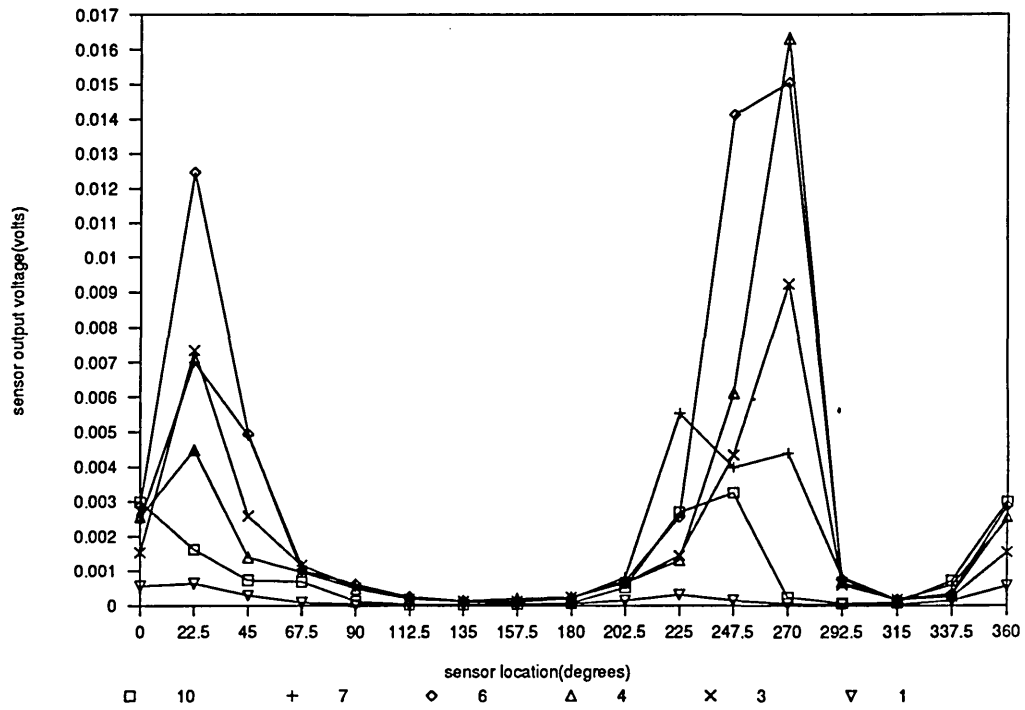
Figure 6.7 Voltage profile of half flow regime for different flowrates, shown in legend as feeder rate unit (1 unit=60 g/s).



6.3.3.3 Stratified flow

The results in figure 6.8 show the particles are concentrated in two distinct regions, which are created by the stratified flow baffle.

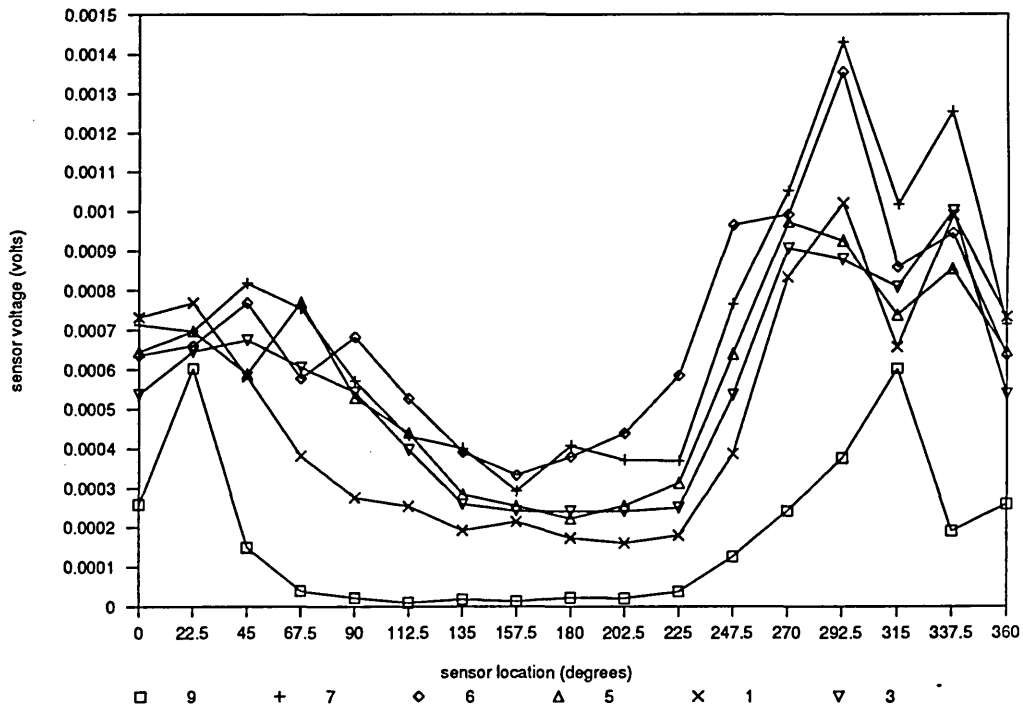
Figure 6.8: Voltage profile of stratified flow for different flowrates, shown in legend as rate unit (1 unit=60 g/s).



6.3.3.4 Annular flow

The annular flow (figure 6.9) shows an increase in amplitude with increased flow rate until 420 gs^{-1} flowrate. At 540 gs^{-1} , the amplitudes drop drastically.

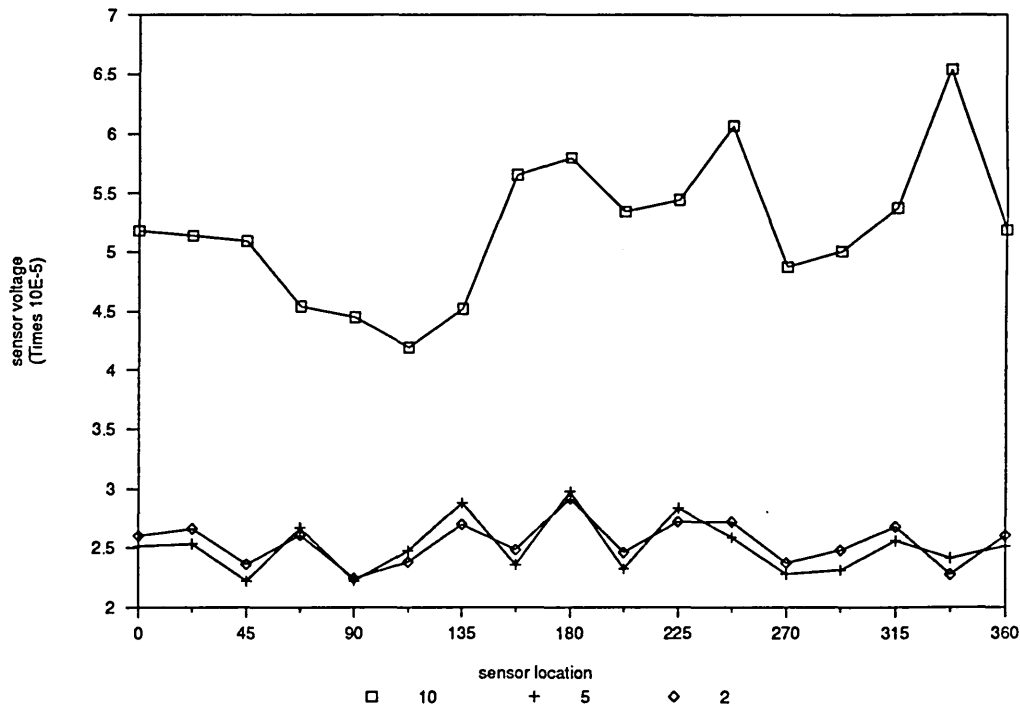
Figure 6.9 Voltage profile of annular flow regime for different flowrates, shown in legend as rate unit (1 unit=60. g/s).



6.3.3.5 Core flow

In the core flow (figure 6.10), the readings correspond to particles flowing through an area of flow in the middle region of the pipe. The transducer readings are uniform at each flowrate tested. Only three flowrates are presented here. The results indicate a sharp increase in amplitude after the 0.3kgs^{-1} unit flowrate.

Figure 6.10 Voltage profile of core flow regime.



6.4 Velocity measurements of sand flow.

6.4.1 The procedures.

Cross correlation of the signals from upstream and downstream sensors are performed to obtain the transit time [Beck and Plaskowski 1990]. This is done for all pairs of corresponding sensors on the pipe boundary.

6.4.2 Cross correlation results.

The cross correlation results are shown for two contrasting regimes: the continuous full flow and the stratified flow. These have been selected to demonstrate the extreme results obtained between good correlation with continuous flow and degraded corre-

lation with stratified flow. The reasons for this variation is discussed in chapter 7.

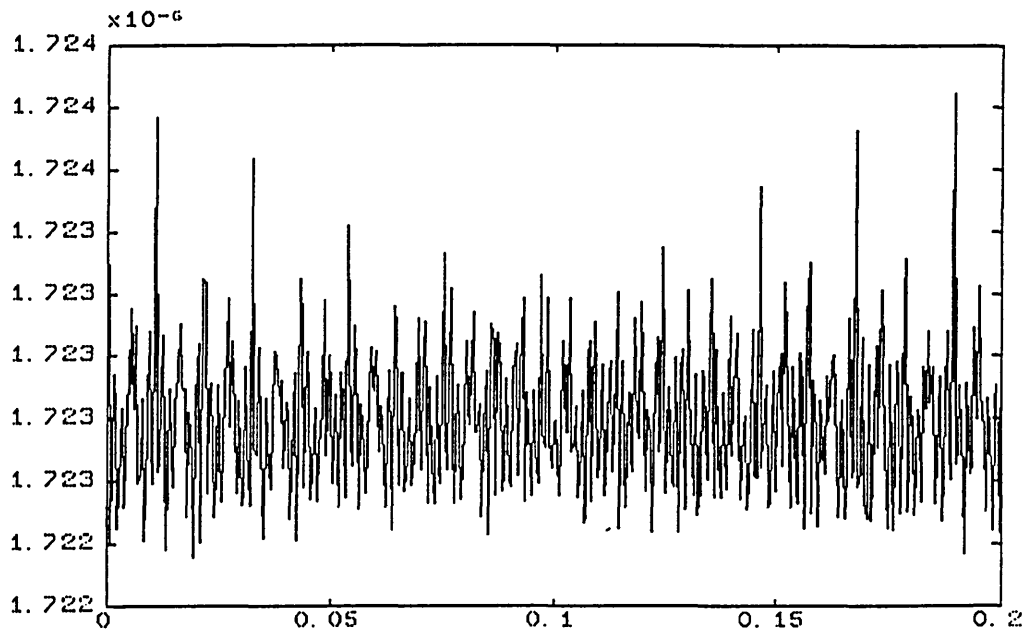


Figure 6.11. Cross correlation of full flow
x-axis: time, y-axis: volt2 (correlation function not normalised)

The cross correlation shown in figure 6.11 is for full flow. The first major peak on the correlogram gives a transit time of 0.01s. The subsequent peaks are due to the pulsations in the flow discussed in section 5.6.

From the transit time, the velocity is found from,

$$\begin{aligned} v &= \frac{d}{\tau_m} \\ &= \frac{0.045}{0.01} \\ &= 4.5ms^{-1} \end{aligned}$$

where d is the gap between upstream and downstream sensors, τ_m is the transit time for the signal to pass between the two sensors and v is the mean velocity of the sand passing them.

Two cross correlation results are presented for stratified flow, representing the dense phase (figure 6.12) and the lean phase (figure 6.13) flow conditions. Figure 6.12 shows a wide peak, suggesting that the particles have a range of velocities. Smaller peaks are superimposed on the main curve at 0.01s and 0.03s, suggesting the presence of two specific velocities (sections 7.5 and 7.6). Figure 6.13 shows no correlation because of the absence of solids in this section of the pipe.

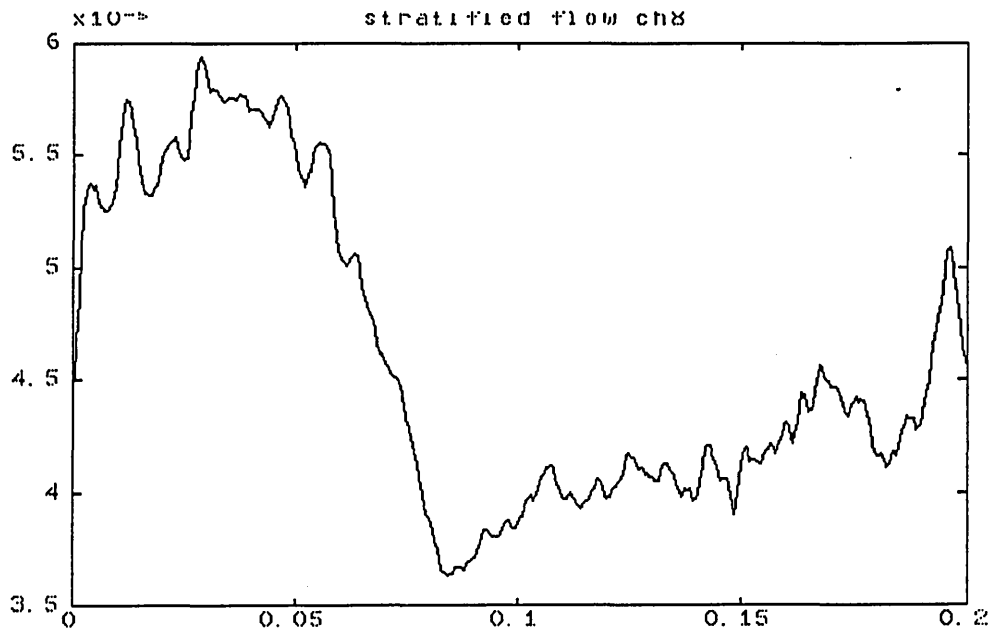


Figure 6.12. Cross correlation of dense side of stratified flow.

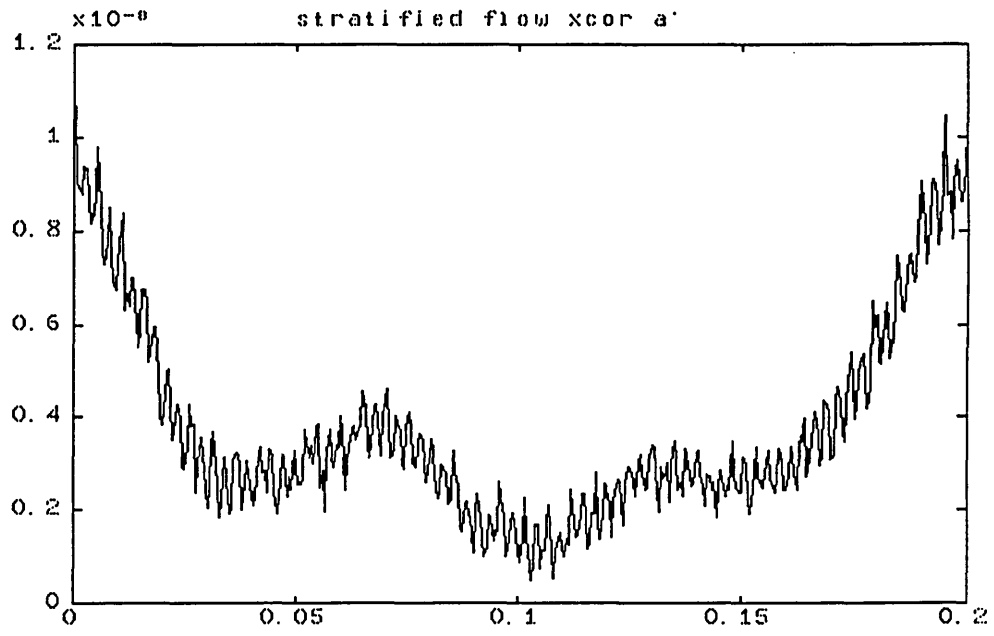


Figure 6.13. Cross correlation of lean side of stratified flow.

Chapter 7

Analysis of Results.

7.1 Introduction.

In this chapter, an analysis of the results from the experiments are presented. The single particle flow results are first analysed (section 7.2) to determine the relationships between the position of the charged particle relative to the sensors and to the sensor outputs.

The sand flow results are then analysed. The analysis of the sand flow results aims to:

1. determine the relationship between particle locations and sensor outputs (section 7.3),
2. identify the spatial patterns from the voltage profiles for flow regime identification by the neural network program (section 7.4),
3. analyse the measured data in terms of its frequency spectra to investigate relationships between the particle size distribution and the sensor outputs (section 7.5),
4. determine a relation for the local mass flow rate from measurements of velocity and voltages (section 7.6),
5. reconstruct the flow image in terms of concentration and particle size distribution by a ratio backprojection method (section 7.7).

7.2 Single particle flow.

The bead enables the effect on the sensor system of a single charged particle to be investigated.

7.2.1 Verification of induction model.

The results shown in figures 6.13 show broad agreement (within 10% of predicted value) with the induction model (section 3.2.2). Two forms of error occurred:

1. random errors due to differences between the bead outside diameter (8 mm) and the guide tube bore (13 mm) and,
2. systematic errors due to the guide tube not being vertical. For bead drop through the centre of a tube.

The random errors were minimised by repeating the measurements, however the systematic error still occurred (shown in figure 6.13a) even though a spirit level was used to set up the guide tube.

7.2.2 Particle location from normalised voltage profile.

The results obtained for the single particle model (section 3.2) and experiments (section 6.2) provide two relationships which may be used for locating the axial position of the particle. These are:

1. between the sensor voltage amplitude and the particle linear distance from the sensors (figure 7.1), and

2. between the particle spatial (angular) position and the voltage profile (figure 6.3).

The normalised ratios eliminate unknowns in the model (sections 3.2, 3.3, equations 3.3 and 3.5). The ratio technique allows location of the particle's position regardless of the charge induced into the sensors (figure 7.1).

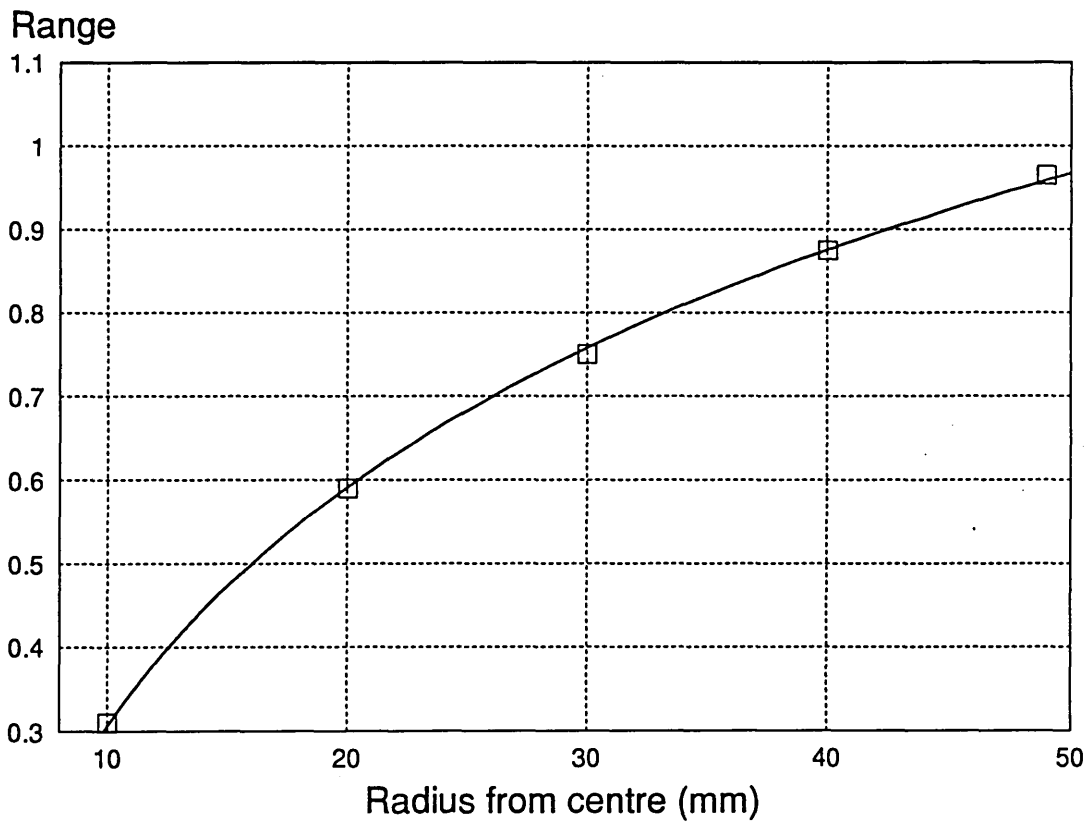


Figure 7.1 Relationship between normalised voltage and particle location from centre of pipe.

7.2.3 Spectral analysis for a single bead.

A frequency analysis is made for each of the recorded voltage signals (section 6.2.2.1) using the power spectral density [DaDisp,1988] (section 4.2). For a specific test the recording with the largest voltage amplitude is selected. The maximum-power frequency, which is the highest power in the power spectrum for this recording, is plotted against the distance of the bead from a sensor. This analysis is repeated for the different axial bead positions. The results for these bead flows are shown in figure 7.2.

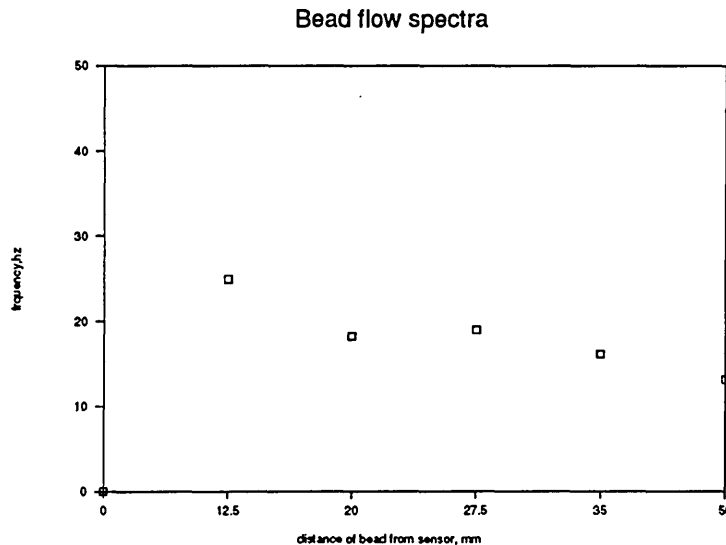


Figure 7.2. Frequency of the component with the highest power versus bead radial position.

The results show a higher frequency signal when the bead is nearer the sensor (figure 7.2). This agrees with calculations by Beck(1986), which predicted a non-linear relationship between the charged particle and the distance from the sensor.

The maximum-power frequency, which is the component with the highest power from these measurements on a single particle show an inverse relationship between frequency and particle distance from the sensor. The frequencies range between 15-30 Hz over a 50mm distance (section 6.2.2.3).

In this work, the size of bead used is 8mm, which produces a peak frequency of 20 Hz when 50mm from the sensor. Sand particles with known size distribution, mainly (48%) 300 micron, give a peak frequency of 550 Hz. (This information supports the simple model of equation 5.2 since a lower peak frequency is obtained from signals derived from the bead compared with sand. The ratio of bead size to sand diameter is 26.7 and the ratio of peak frequency for the sand to the peak frequency of the bead is 27.5.). Beck [1986] presents the calculated relationship of peak frequency with sensor to particle distance sketched in figure 7.3.

The significance of these results is:

1. for a fixed particle size and velocity, there is a relationship between the signal frequency component with the highest power and the particle position in space (figure 7.2).
2. for a fixed particle velocity there is a relationship between the frequency of the component with the highest power and the particle size distribution.

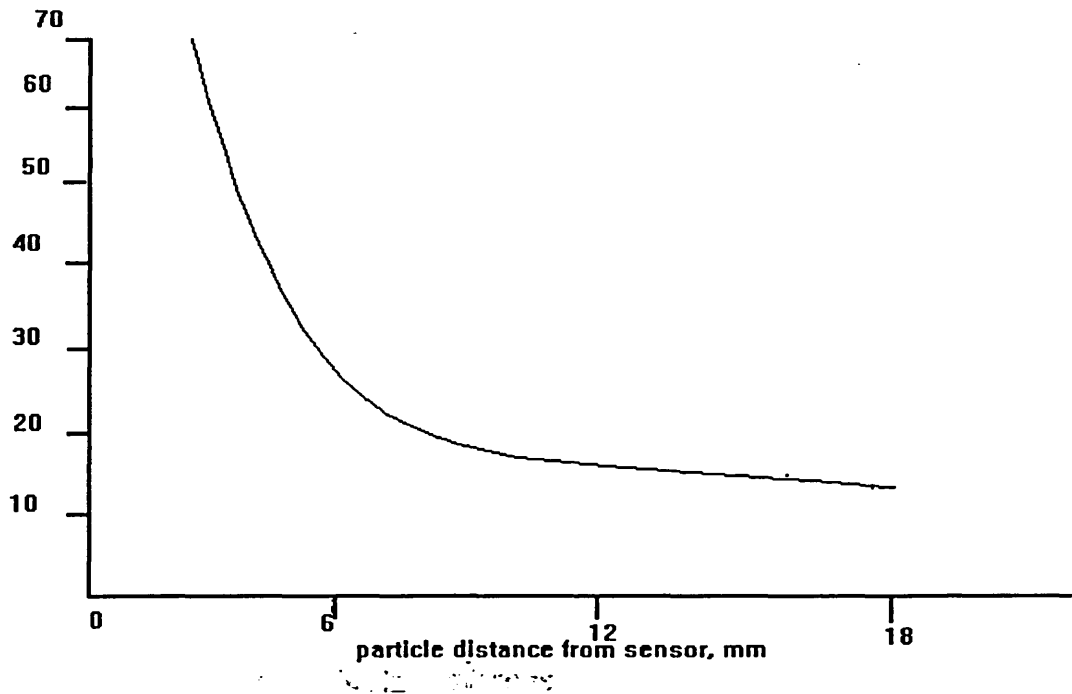


Figure 7.3 Relationship of peak frequency (Hz per m/s) on y axis and particle to sensor distance (mm) (Beck 1986).

7.3 Voltage profiles for sand flow.

The results in section 6.3.2.2 show the voltage profiles for the flow regimes tested. This section compares these results, using normalised scales, with the predicted voltage profiles, obtained using either the single particle (section 3.2) or the two particle (section 3.3) models. The discussion on the change in voltage measurements with flowrate is presented in section (7.6).

7.3.1 Full flow.

The recorded measurements show consistency in value (figure 6.6), although the boundary voltage profile suggests the delivery of sand to be denser on the side nearer to the screw feeder.

The models predict a uniform profile for the boundary voltages for full flow since the net charge carried by the volume of charged particles is effectively concentrated at the centre of the conveying pipe (figures 3.4, 3.8f and equation 3.19). Normalization of these data gives consistent flow patterns over the range of flowrates provided by this particular flowrig (figure 7.4).

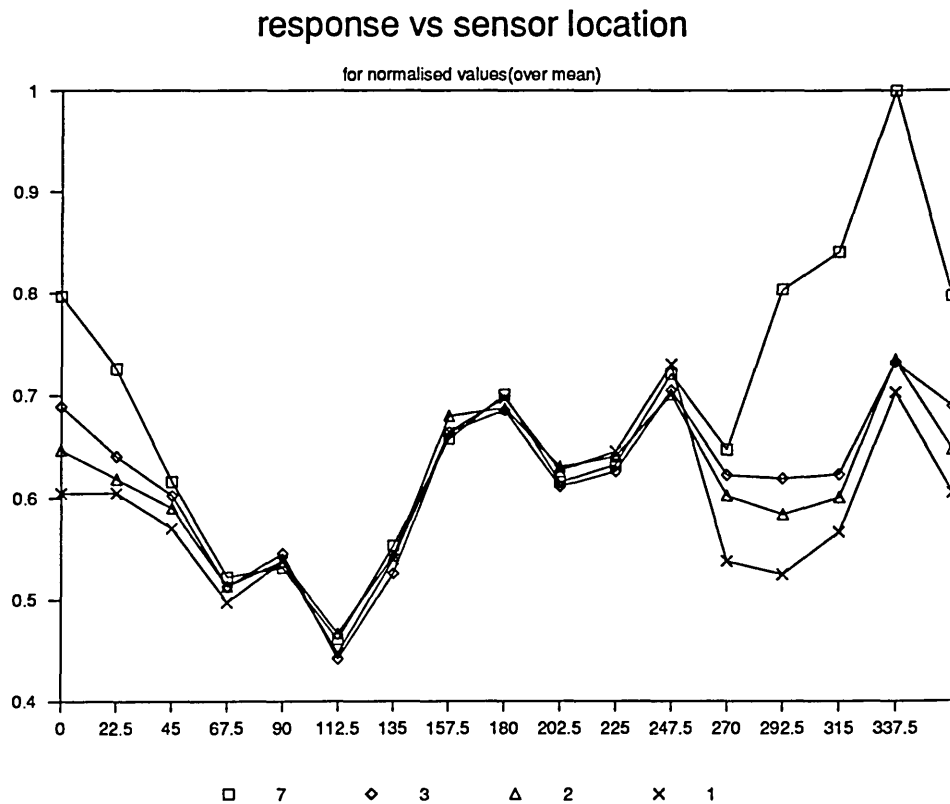


Figure 7.4. The full flow regime pattern.

7.3.2 Half flow.

The range of maximum to minimum readings is highest at about 337.5° (figure 7.5). This range is higher than for the full flow regime (figure 6.10) since the particles are concentrated in one half of the pipe. On a normalised scale, the single-particle model predicts a similar voltage profile when the particle is nearer the sensors in one half of the pipe.

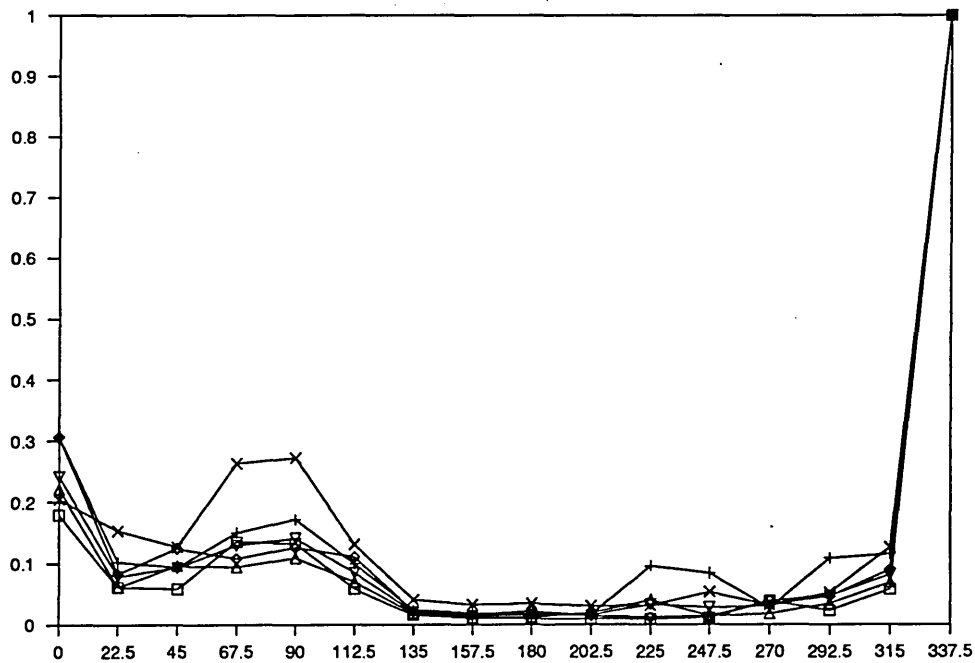


Figure 7.5. The half flow regime pattern.

7.3.3 Stratified flow.

From the measurements in section 6.3.3.3, the boundary voltage profile shows two distinct peaks. The consistency of these peaks over the range of flowrates tested is shown in figure 7.6. The prediction by the two particle model also shows a similar pattern (section 3.2.3).

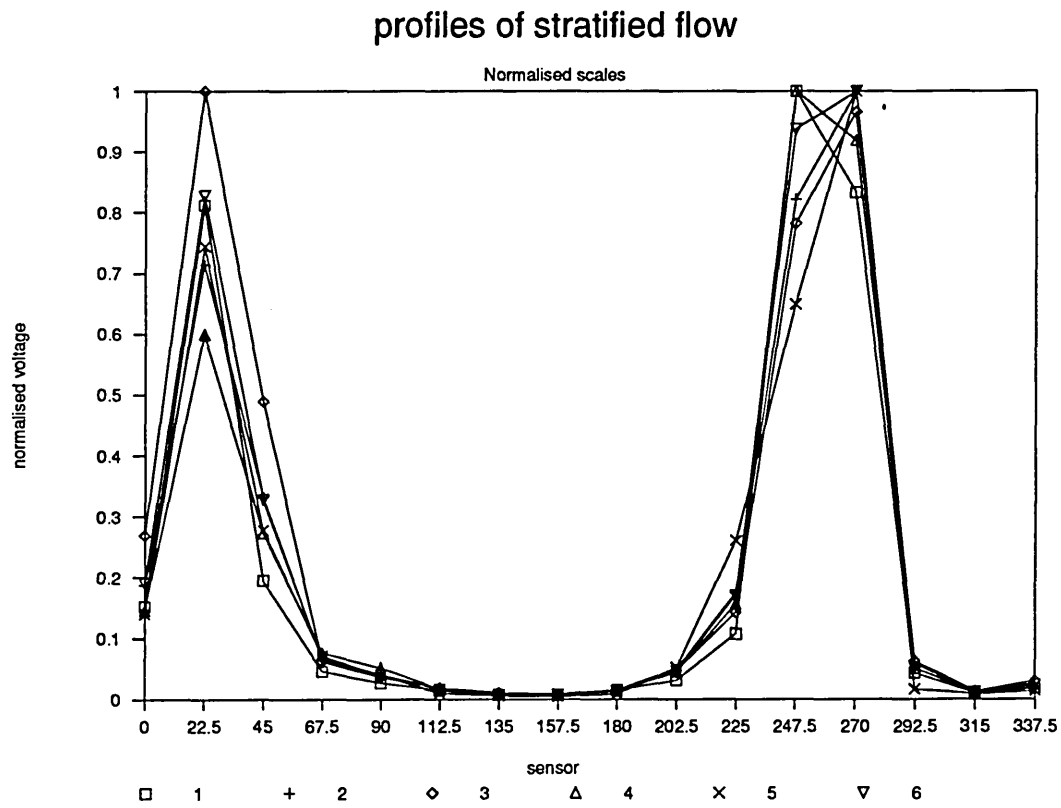


Figure 7.6. The stratified flow regime pattern.

7.3.4 Annular flow.

In annular flow, the normalised readings (figure 7.7) vary in a cyclic manner above or below the mean value. In the idealised model, the predicted voltage profile is a straight line representing a uniform profile. The variation from the model is due to the uneven delivery of sand discussed in section 7.3.5.

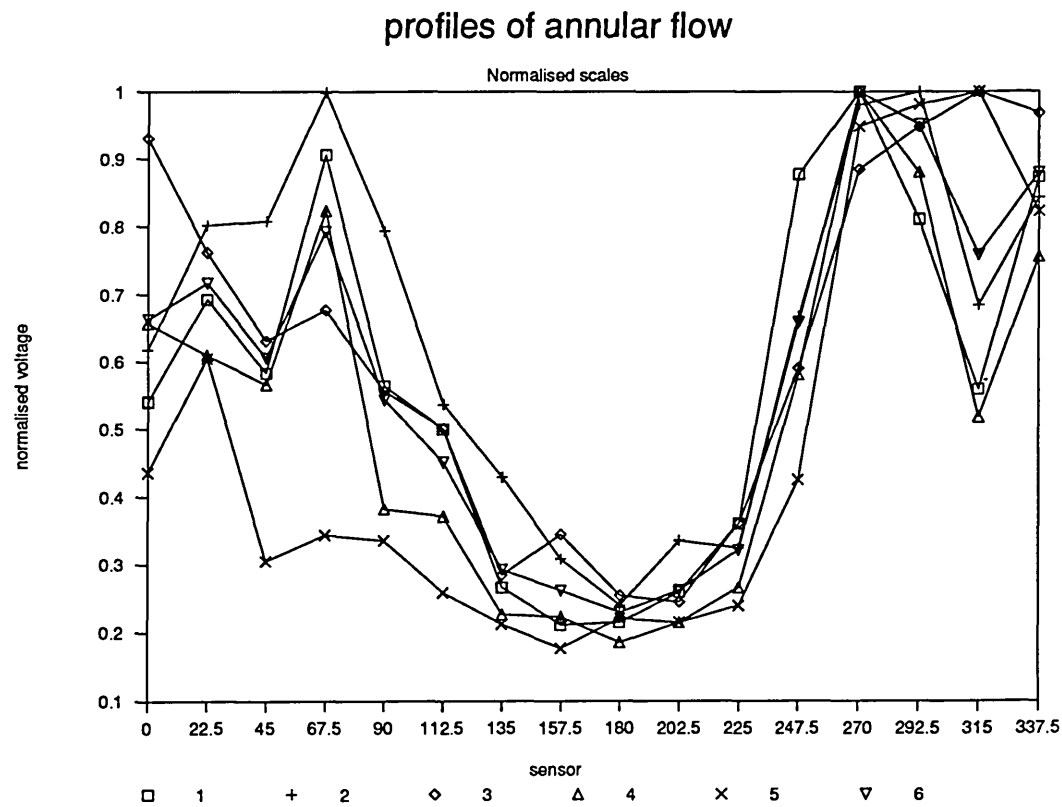


Figure 7.7. The annular flow regime pattern.

7.3.5 Discussion on flow profiles.

The voltage profiles shown in figures 7.4 to 7.7, are directly related to the distance of the charged sand particles from the sensors around the pipe boundary. This profile

represents an image of the sand distribution near to the periphery of the pipe but not across the plane of the sensors, which is the final aim of tomographic imaging. This limited image, which may be derived by using simple, ratio techniques (section 7.1) is, nevertheless, useful for flow regime recognition and will be discussed further (section 7.4). The cross-sectional image requires a reconstruction algorithm with a more rigorous model in order to produce images from boundary data. However, the results of this work have been used to demonstrate a ratio back projection technique of cross-sectional image reconstruction from boundary data (section 7.7).

The flow regimes are distinguishable as follows:

1. The amplitudes obtained were highest for annular, then full flow followed by core flow, although the profiles are similar. The order of magnitudes were 10^{-2} volts, 10^{-3} volts and 10^{-4} volts respectively for the three cases of flow over the range of flowrates used.
2. The profiles of half and stratified flows have single and double peaks respectively.

The corresponding curves generated using the two particle model (section 3.3) are smoother since 32 sensors have been used in the calculations. The curves from the measurements may be improved by mounting more sensors on the pipe wall and averaging the flow signals over a longer period.

7.3.6 Comparison of models with sand flow results.

The two-particle model (section 3.3) may be used to predict the normalised boundary voltages for different flow regimes. Placing both particles in the middle of the pipe,

simulates the full (section 7.3.1), core and annular (section 7.3.4) flows because the charge is effectively concentrated in one particle at the centre. By placing the two particles in one half of the pipe, simulates the half flow regime (section 7.3.2). Then, by placing one particle in each half of the pipe cross-section, the stratified flow (section 7.3.3) is modelled. When the two particles are combined together, the two particle model effectively reduces to the form of the single particle model (section 3.2).

7.4 Flow regime identification from measured data.

The analysis of the sand flow results (section 7.3) indicates consistent patterns of profiles being obtained for the test flow regime over the range of flowrates measured. This is important since it allows identification of flow regimes using neural networks without requiring the amplitudes to be taken into account.

The main interest in flow regime identification is to discriminate between the different flow spatial patterns represented by the boundary voltage data. The measurements obtained are normalised over the maximum voltage amplitude of a set of data in the 16-channel configuration (section 3.2.2). This enables the recognition of flow regime patterns by neural networks.

7.4.1 The training patterns.

The training patterns tested consist of three patterns of normalised voltage profiles for the full, half and stratified flows. The annular and core flow patterns are similar in form to the full flow pattern and hence other secondary discrimination techniques are more suitable, for instance the checking of amplitude levels (section 7.3.5).

The training patterns (figure 7.8) are taken from normalised profiles of each flow regime. Figure 7.9 shows the variations in the training data due to noise in the voltage signals obtained from the data acquisition system. The training patterns are taken from the range of flowrates and not limited to one particular flowrate since the patterns are independent of flowrate (section 7.3).

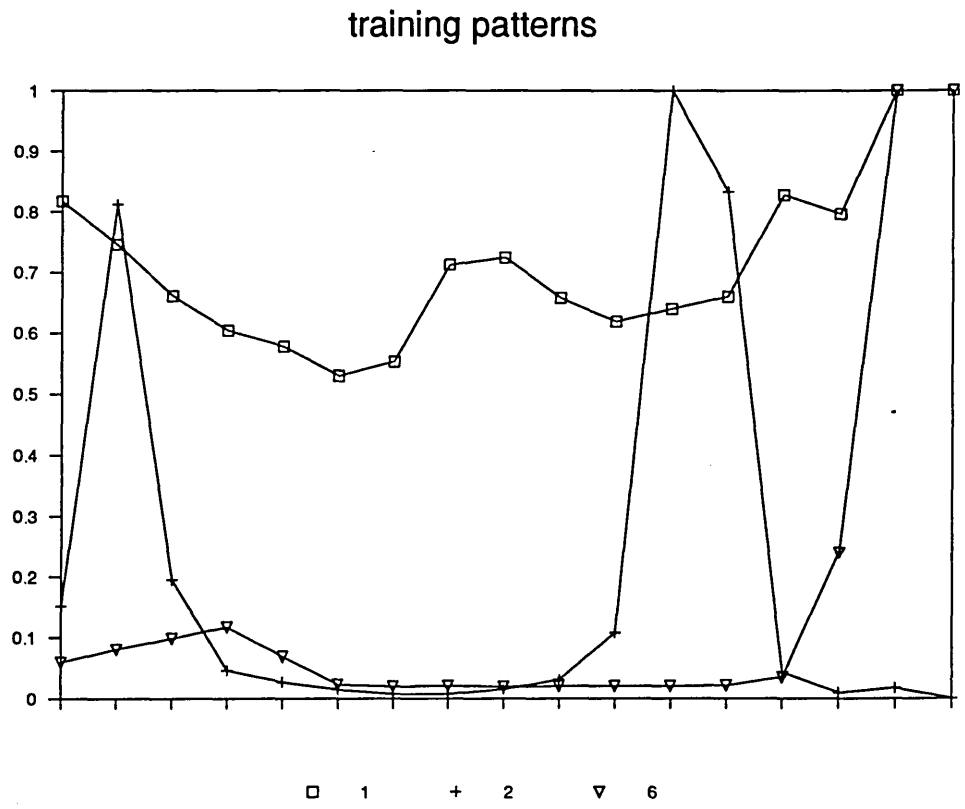


Figure 7.8 The training patterns.

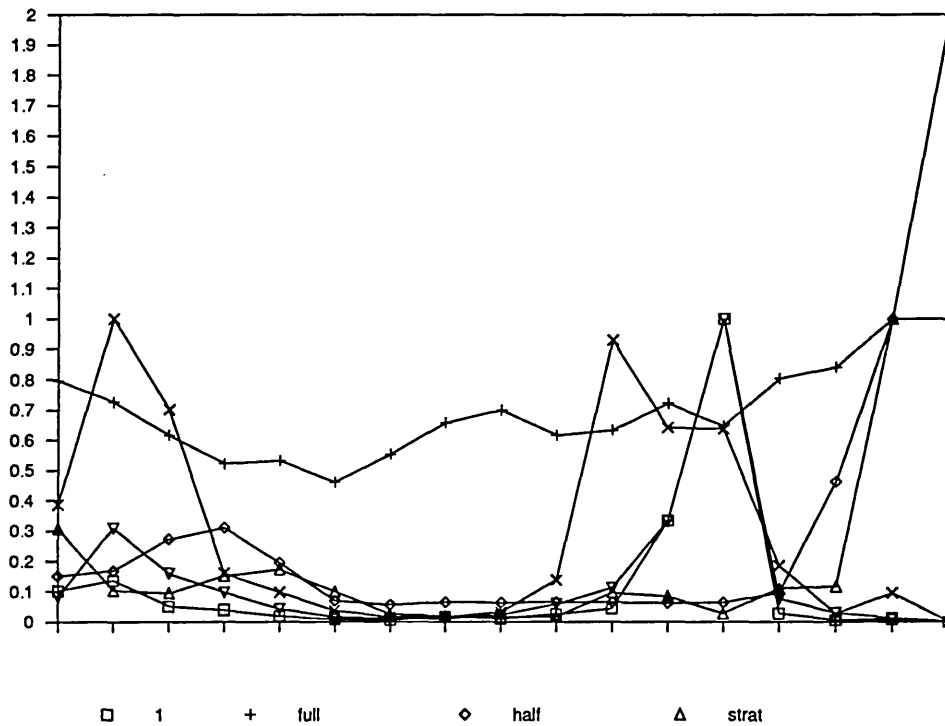


Figure 7.9 The training data set.

This implies that calibration in terms of the varying flowrate is not required for identification purposes of these three flow regimes. The initial exercise of using the threshold values shown in section 4.3 has demonstrated the neural network's ability to recognize patterns of the three flow regimes. The program developed in section 4.3 is used in the tests with real data (7.4.3). The tests in section 4.3 show that the modified Kohonen network, using the Gaussian hat neighbourhood updating rule gives improved performance and is the system used in the following tests.

7.4.2 The neural map classifier.

The training phase requires the input patterns to be trained on the network until the nodes on the network have achieved weight vectors that are sensitive to the test inputs (section 4.3). The idealised flow regime tests presented in section 4.3.3 have been used to train and test a network. The network program written for classification of the flow patterns uses a simple neural map classifier (figure 7.10), when an output node responds to a presented input, a '1' is shown, otherwise a '0'. A neighbourhood that is close to this node in terms of the match of weight vectors is also displayed in the same way.

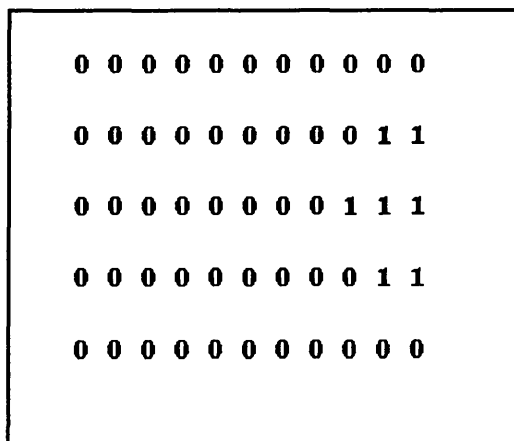


Figure 7.10 Neural map classifier showing regions of activation by 1's corresponding with a matching input on a 5x10 map.

The training examines the effect of 5000, 10000 and 25000 iterations. Two-regime and three-regime identification tests are performed. Mixed patterns are used in the training to allow the network to learn the patterns randomly and not in a particular sequence. An output neural map of 10 X 10 nodes is used as the neural network classifier.

7.4.3 The test patterns.

In the two-regime identification test, the results show over 90% correct identification (Table 7.1 row A). The full flow regime is easily separated from either the stratified or half flow regimes. This result is obtained by testing with a new set of normalised flow data. Success is defined as the correct classification of the flow regime by the output node on the neural map, associated with the input flow data. Two tests were performed and the following results are achieved:

	Regime	Data set	Success	%
A	full	14	13	92.9
	half	15	15	100.0
B	half	35	27	77.14
	stratified	12	4	33.33

Table 7.1. Two regime test results for (A):full and half; (B): half and stratified

The stratified and half flow regimes are difficult to classify separately (Table 7.1 row B). More training sets are required to improve the efficiency of separating the two

patterns which appear to be similar. This is because the neural network used is noise tolerant and it could not differentiate the two similar patterns. Only 30% success rate is achieved within the training conditions described.

Regime	Test set	full class	half class	stratified class	%
full	18	11	6	1	61.1
half	47	-	31	26	67.0
stratified	47	10	13	24	51.1

Table 7.2. Results for three regime identification

The analysis of the regime identification results (Table 7.2) shows the problems involved in classifying real data. In the idealised tests (section 4.3.3) over 85% correct classification is achieved even with 20% noise. The results with noise, as in this measurement set, show only 50-70% correct classification, even with a longer training time of 25000 iterations. More control is needed of the training and neural network parameters in order to achieve better classification performance.

7.5 Velocity and mass flowrate estimations.

The model developed in section 3.6 (equation 3.33) shows a relationship for the local and totalised mass flowrate derived from the voltage amplitude of sensor (U_i), velocity (v_i) and flow regime factor (k_m). The following is the analysis of the results from measurements discussed in section 6.3.

7.5.1 Velocity from cross correlation.

The analysis of the full flow cross correlations shows a transit time of 0.01s (figure 6.11), corresponding to a velocity of 4.5 ms^{-1} . It is observed that there are repeated peaks with slightly smaller correlation amplitudes which are attributed to the cyclic nature of the sand flow pulsations.

Analysis of the stratified flow also gives a correlation time delay of 0.01s where there is most flow (section 6.5.2) and no correlation on the side with little flow (blocked by the baffle). A wide peak is observed for the stratified flow (figure 7.13) because of the presence of a range of particle velocities caused by interaction with rebounding particles which have collided with the baffles (section 7.5.3). Had the baffles been placed further upstream, the particles may have reached a more uniform velocity and the boundary pair of sensors should give better correlations.

The cross-correlation analysis to obtain transit time measurements for velocity calculations gave these main results:

1. In continuous and homogenous flow, the correlations are consistent and repeatable by all the sensors used
2. In stratified flow, the correlations give spatial variation of velocities

7.5.2 Mass flowrate from velocity and voltage measurements.

The equation 3.33 suggests that the local mass flowrates may be totalised to provide the total mass flowrate. The experimental setup did not provide good cross correlations (and hence velocity) for the purpose of calculating mass flow rate, because of the close

proximity of the baffles to the sensors (section 7.5.1). However, results for the voltage measurements can be used to show the feasibility of obtaining totalised mass flowrates from localised flowrates around the boundary sensors.

The mass flow rates obtained from the graphs of totalised voltage amplitudes against flow rate for different flow regimes provide gradients, termed slope factors, that correspond with the individual flow regimes.

For the full flow, figure 7.11, there is a linear increase of totalised voltage, which is proportional to mass flow rate until the flow rate is 0.3 kg/s, as shown by the mass flow rate model (equation 3.33). The gradient of the linear regression line fitted to the points is 0.040 V/kg/s. For feed rates greater than 0.3kg/s the totalised voltage decreases.

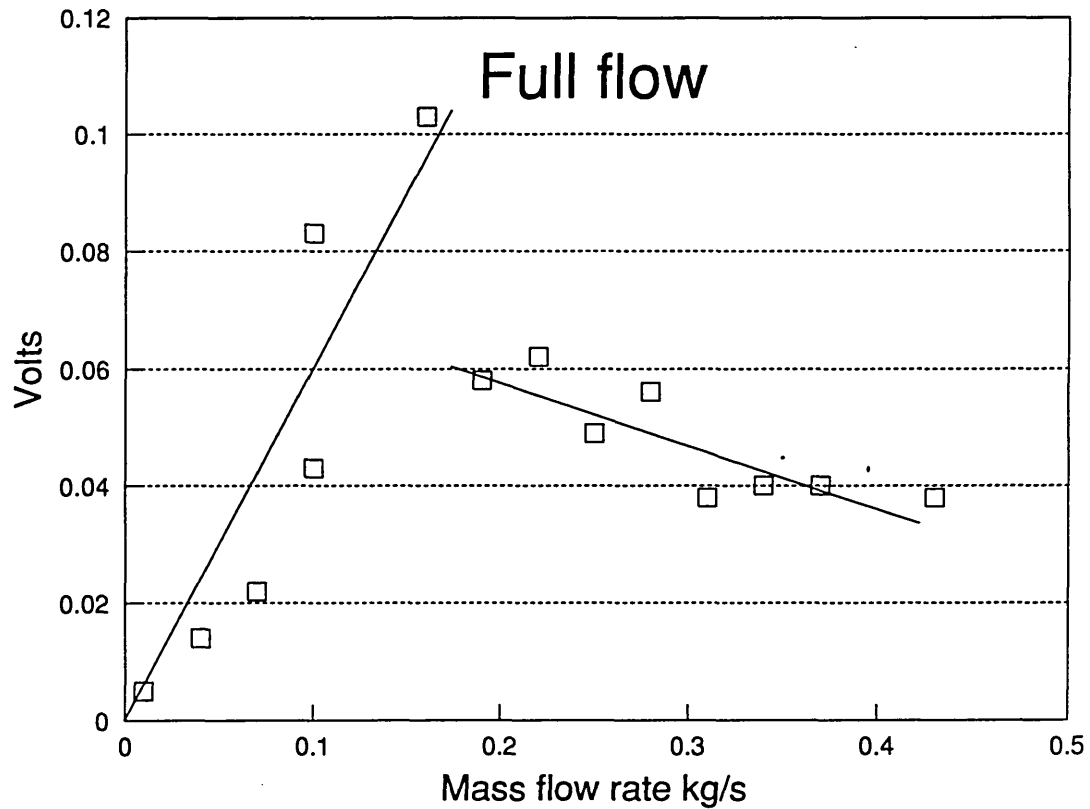


Figure 7.11 Totalised sensor voltage (y axis)
versus flowrate (x axis) for full flow.

For the annular flow, figure 7.12, the totalised voltage increases with the solids flow rate until the rate is 0.3 kg/s^{-1} , after which the totalised voltage decreases. This reduction is attributed to the increased particle interaction with the baffles at the higher flow rates. The gradient of the linear regression line fitted to the points is 0.040 V/kg/s .

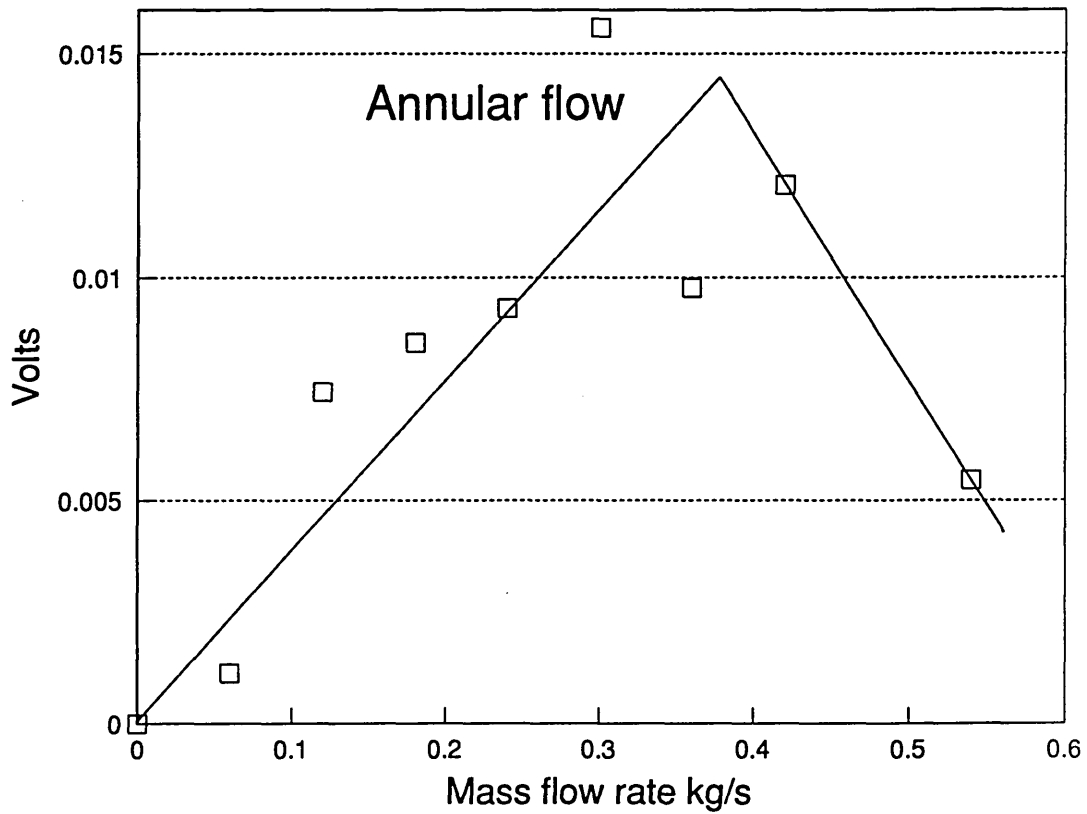


Figure 7.12 Totalised sensor voltage (y axis)
versus flowrate (x axis) for annular flow.

For half flow, figure 7.13, the voltages increase with increases in solids flow rate until 0.360kg/s^{-1} flowrate after which they reduce. This result is in agreement with the results shown in figure 7.12 for the annular flow. The gradient of the linear regression line fitted to the points is 0.044 V/kg/s .

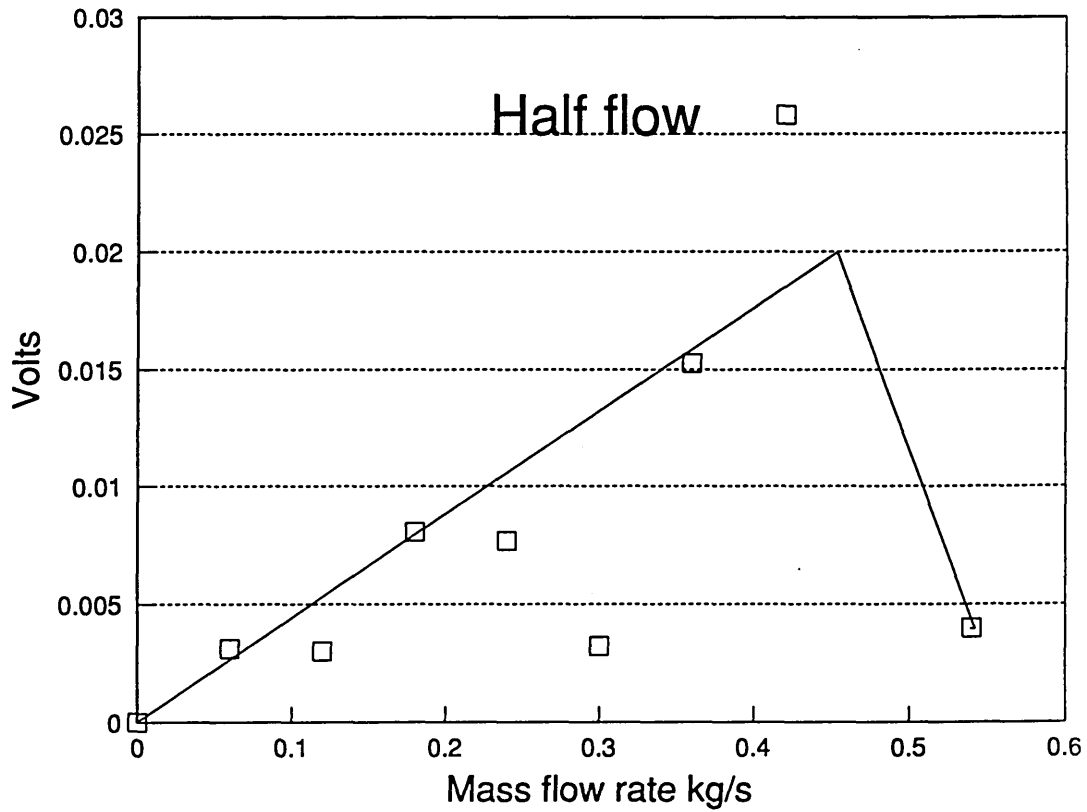


Figure 7.13 Totalised sensor voltage (y axis)
versus flowrate (x axis) for half flow.

For the stratified flow, figure 7.14, the amplitude increases with feedrate as in the cases for annular and half flows. The gradient of the linear regression line fitted to the points is 0.161 V/kg/s.

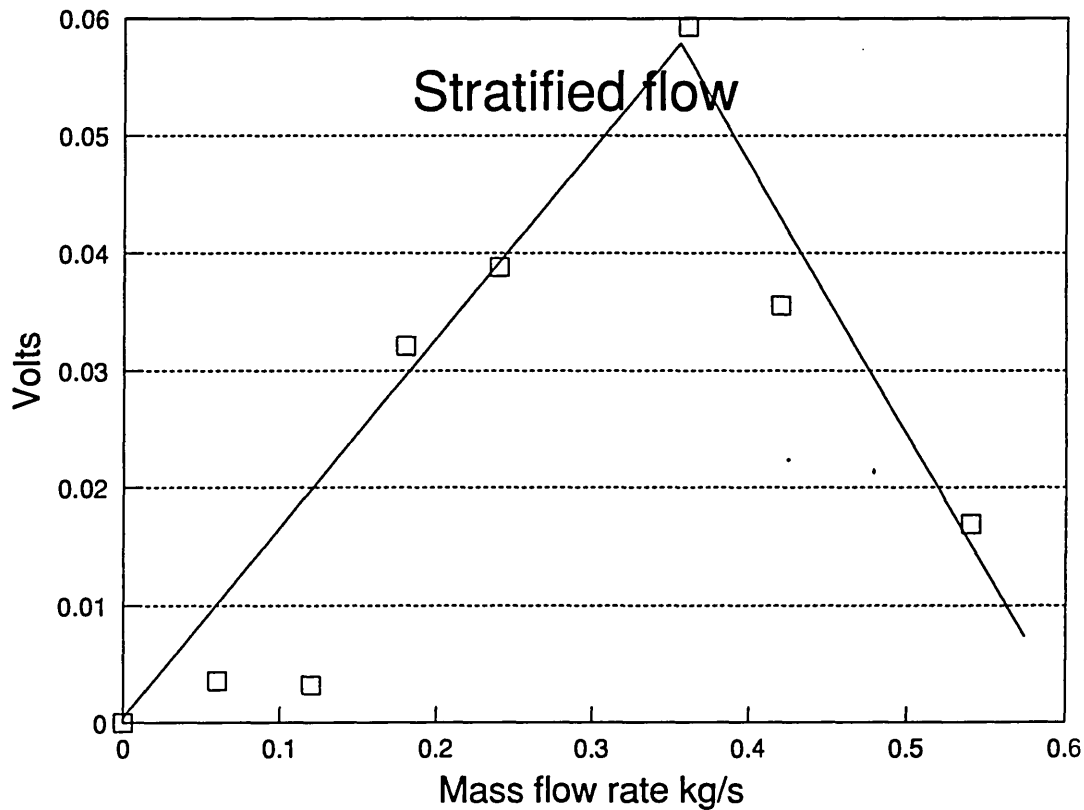


Figure 7.14 Totalised sensor voltage (y axis) versus flowrate (x axis) for stratified flow.

More experiments are required to verify the results obtained in this initial investigation pertaining to the determination of velocity and mass flow rate distributions within a pipe cross-section. The results obtained so far only show boundary local velocities but not internal spatial velocity distribution as required for tomography.

7.5.3 Effects of baffles on velocity and mass flowrate.

The relationships between flowrate and sensor amplitude readings are linear up to a certain mass flow range after which the outputs fall. This phenomenon is not due to saturation of the sensors however it may be due to some of the following reasons.

1. Initially the output of a sensor, which is measuring the randomly varying signals occurring in conveyors with pneumatically conveyed solids, increases with flow rate. It then reaches a plateau and gradually decreases back to zero as the flow rate increases further [Green 1981].
2. The process of agglomeration, which increases with flow rate [Lapple 1970], causes heterogeneous flow regions to occur [Li et al 1991].
3. Particle which collide with the baffles may rebound and collide with free falling particles. The angle and velocity of rebound is dependent on the shape of the baffle; the number of interactions is dependent on solids flow rate.

In full flow, sand particles drop at a relatively uniform velocity since the height of drop is fixed and no obstacle is put in the path of the sand. In other flows, when baffles are placed 100mm above the sensor plane to create artificial regimes, the effects of sand bouncing off the sides of the baffles create:

1. variation of particle velocities across the plane of the sensors,
2. agglomeration of the particles, the presence of clusters is inferred from the investigating of the spectral density (section 7.6).

7.6 Spectral analysis of electrodynamic signals.

7.6.1 Power spectrum of flow signals.

The measurements from the sensors are converted into power spectral density (PSD) graphs using the DaDisp software [DaDisp 1988]. These graphs are analysed to extract

salient features, mainly the maximum power frequency and the frequencies at which significant peaks occur. This section presents the analysis of these features in relation to the flow conditions.

7.6.1.1 Full flow.

The spectra shown in figure 7.15 are relatively independent of solids feed rate. However there is a slight reduction of the dominant frequency at the highest feed rate. The windows W1 to W5, which correspond to increasing flowrates from 0.060 to 0.420kgs⁻¹, show little change in the power spectrum. However, windows W6 to W8 show the spectrum for 0.540kgs⁻¹ for different sensor positions show consistency in the shift of frequency power to the lower frequency range.

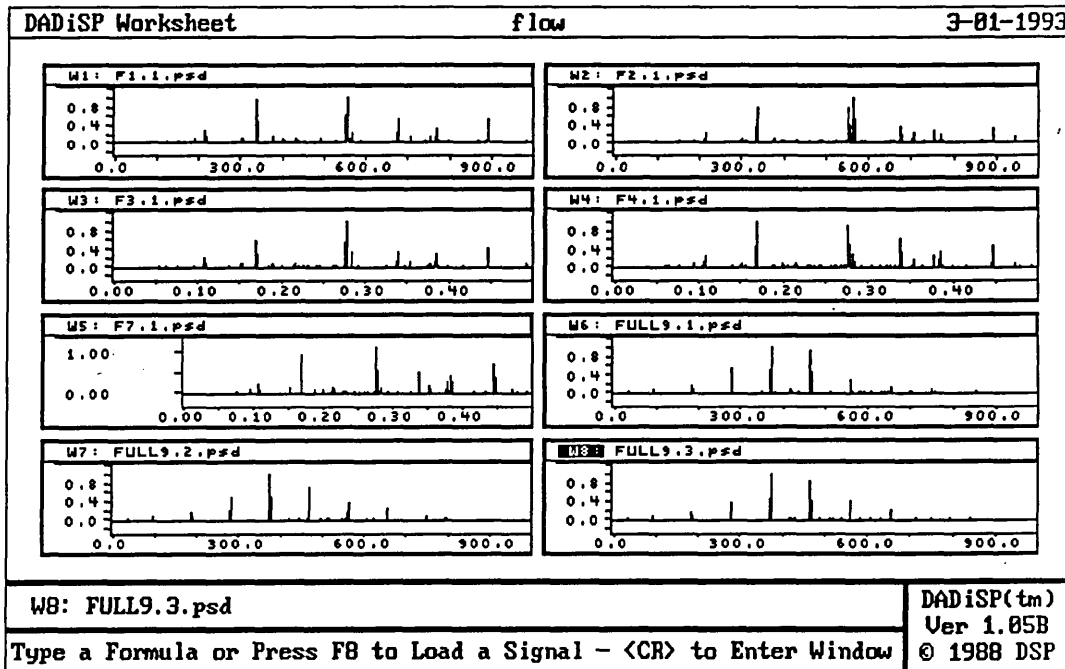


Figure 7.15. A relative psd for full flow.

These results are summarised in figure 7.16. In this graph, only the two largest spectral lines are shown. The main peak frequencies do not change with flowrate and remain constant at about 550Hz with a second peak at 300Hz for all flowrates tested. From the particle size distribution (figure 5.7), the particles are mainly about 300 μ m (48%) and 200 μ m (30%) in diameter. This suggests that two particle size ranges are dominant in the signal justified by equation 5.2.

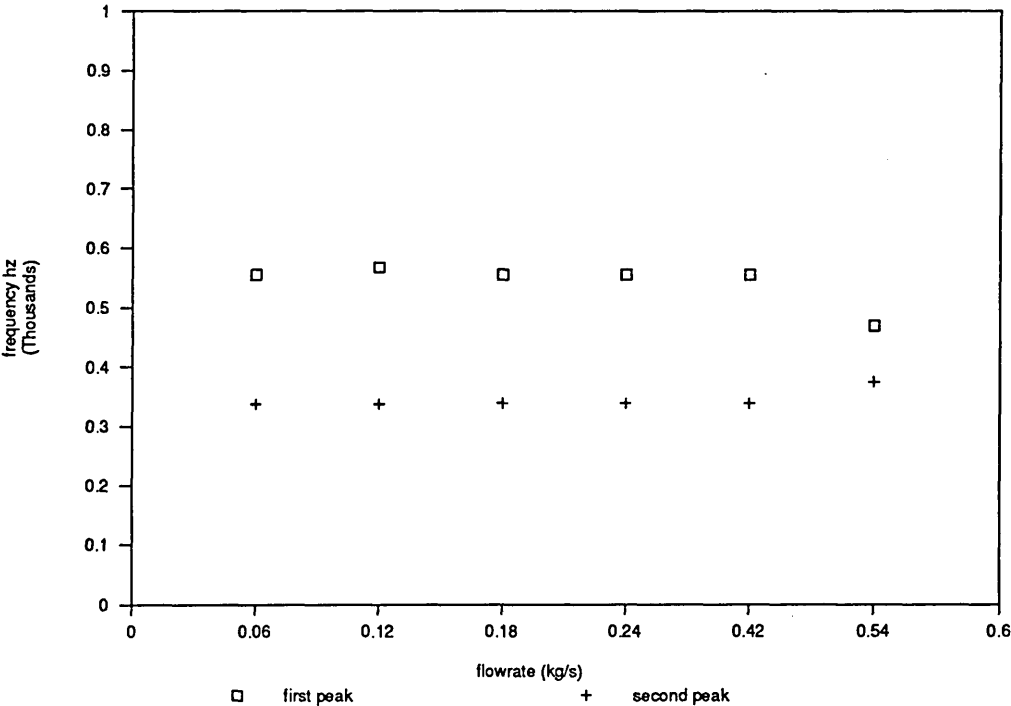


Figure 7.16. Maximum power frequencies from signal spectra with change of flowrate - full flow.

7.6.1.2 Half flow.

In the graphs shown in figure 7.17 a cyclic observation is presented corresponding with the boundary location of the sensors. The results show flow is dense in windows 15 to 7. Lean flow occurs between windows 8 to 14. The power spectrum extends over a wide range of frequencies for the sensors near to the flow, but only individual lines exist for the sensors remote from the flow.

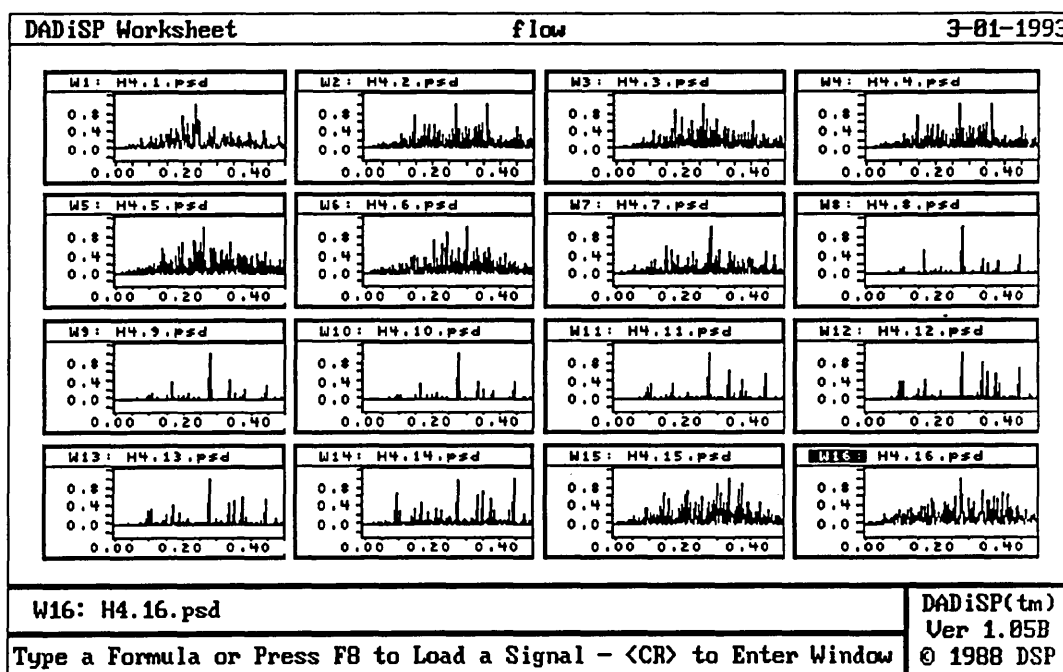


Figure 7.17. Relative psd of half flow.

A large peak at 550 Hz is observed. As for full flow, this is a dominant frequency relating to a dominant size range in the particle distribution. The range of spectra shown arises due to the presence of the baffle, which alters the velocity range of the particles by several mechanisms [Gadhetsroni 1982].

7.6.1.2.1 Collisions.

Many of the particles fall and strike the baffle. These particles may rebound and continue to fall at reduced speed or collide. These collisions may be with other particles or the pipe wall resulting in a range of velocities. Some particles will have low velocities others may exceed that of the free falling particles.

7.6.1.2.2 Hydrodynamics.

The particles are forced into closer proximity by the baffle. This may reduce the hydrodynamic resistance resulting in an increased velocity.

7.6.1.2.3 Clustering.

Increased proximity of the particles may lead to clustering, and if the charges on the particles are modified or lost in collisions with the wall or baffle to agglomeration [Li et al 1991]. This is only probable at the higher flow rates and should result in a decrease in the level of charge with increased mass flow rate.

The agglomeration process clusters particles together as shown in figure 7.18. Particles can cluster in a line, a plane or a volume to form larger particles of different sizes and shapes.

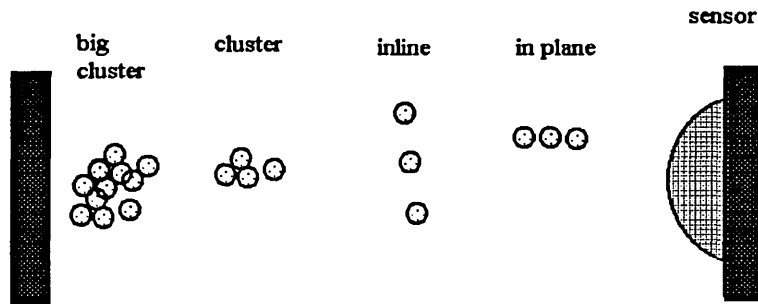


Figure 7.18. Clustering formation of particles [Li et al 1991].

7.6.1.3 Annular flow.

Figures 7.19 and 7.20 are for annular flow. In window 1 of figure 7.18, for flow rate of 0.060 kgs^{-1} , the PSD's are maximum at 340Hz (0.17×2000) and 540 Hz. At increased flow rates the range of spectra increases in a similar manner to that observed in section 7.6.1.2.

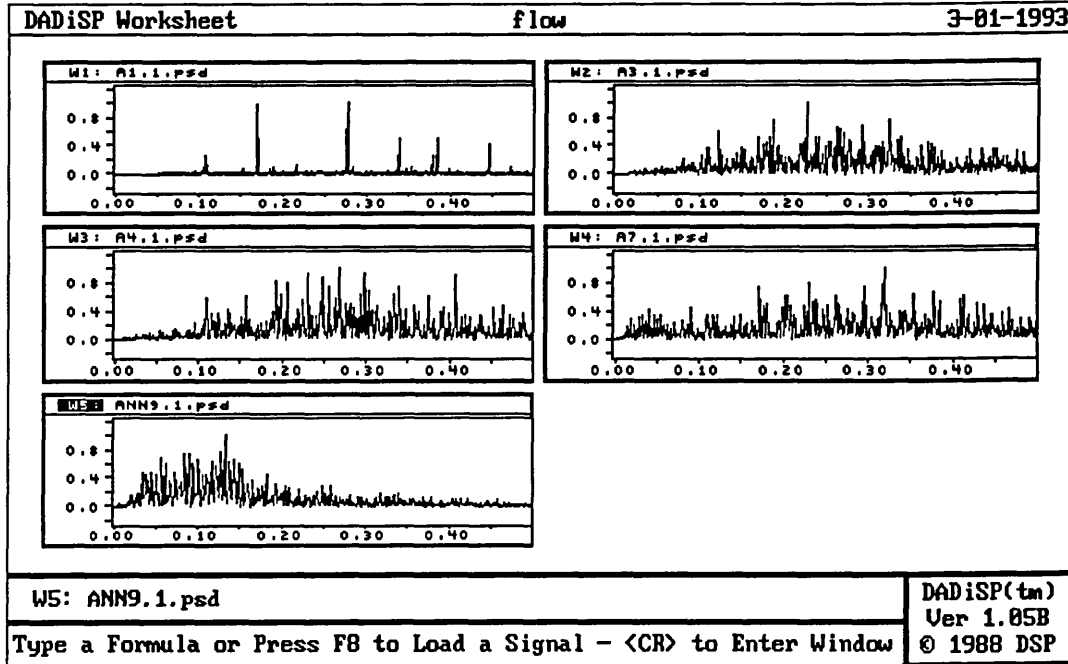


Figure 7.19. A relative power spectral density plot

Y axis is relative psd and x axis is x 2000 Hz (annular flow).

Figure 7.20 shows the power spectrum for one sensor at high flow rate. There is a noticeable downward shift in the energy distribution of the spectra. This result may be explained by the discussions presented in sections 7.6.1.2.1 and 7.6.1.2.3

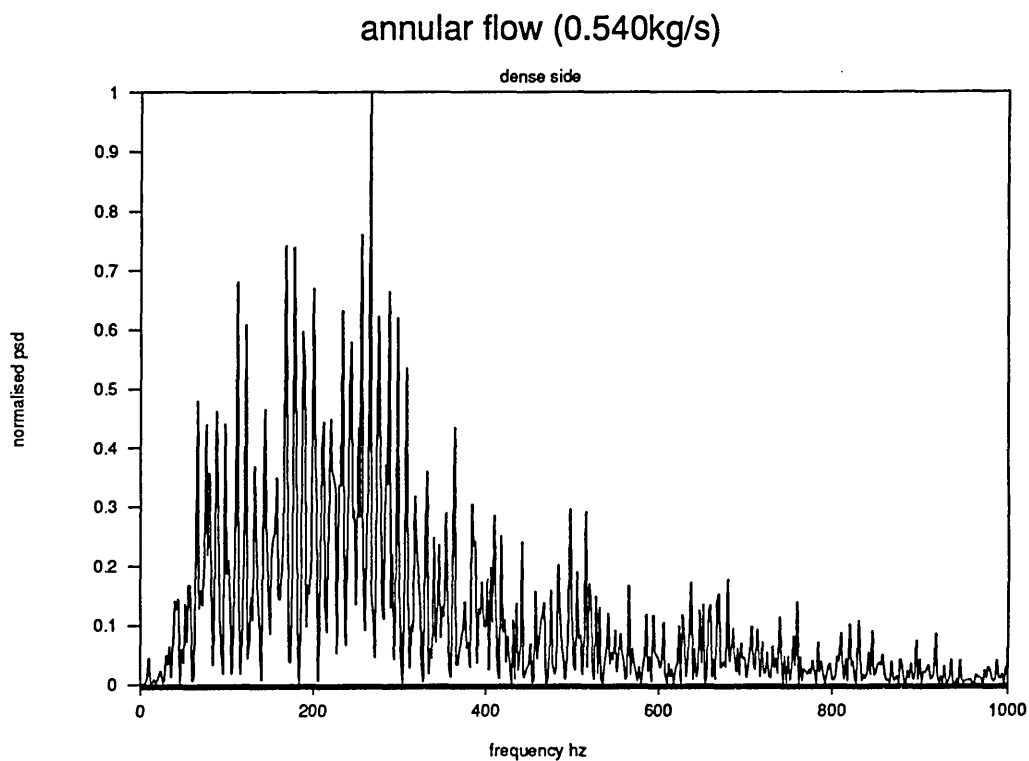


Figure 7.20. Peak frequency spectra for annular flow
at 0.540kg/s^{-1} flowrate.

The results shown in figure 7.21 indicate a linear increase in peak frequency with increase in flowrate (section 7.6.1.2.2). However, at higher flowrates and concentration, the peak frequency drops, which support the proposition of agglomeration described in section 7.6.1.2.3.

Spectra of annular flow

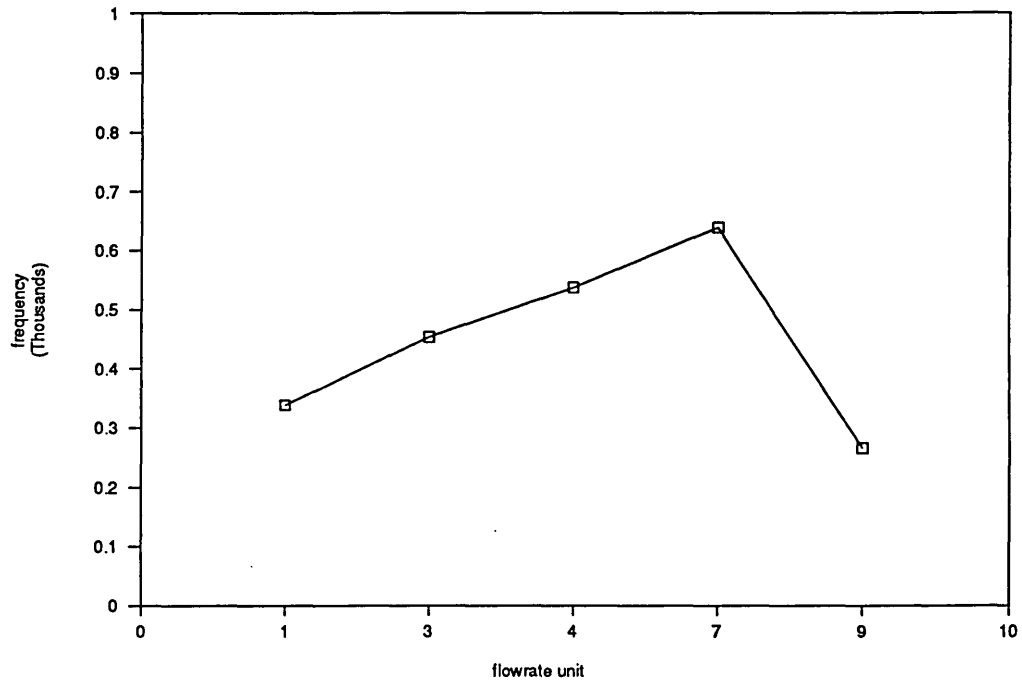


Figure 7.21. Power frequency from signal spectra with change of flowrate - annular flow.

7.6.1.4 Core flow.

In core flow (figure 7.22), more spectral lines are observed at lower frequencies as the flowrate increases.

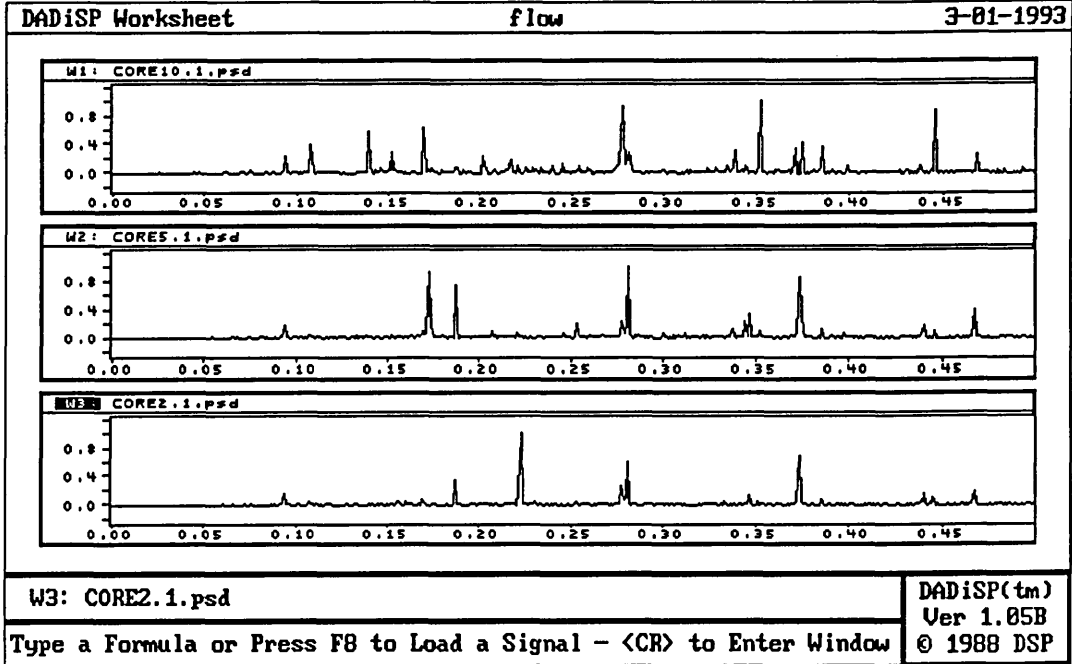


Figure 7.22. Relative psd of core flow.

The figure 7.23 shows a similar result to annular flow but without the drop in power frequency at higher flowrates.

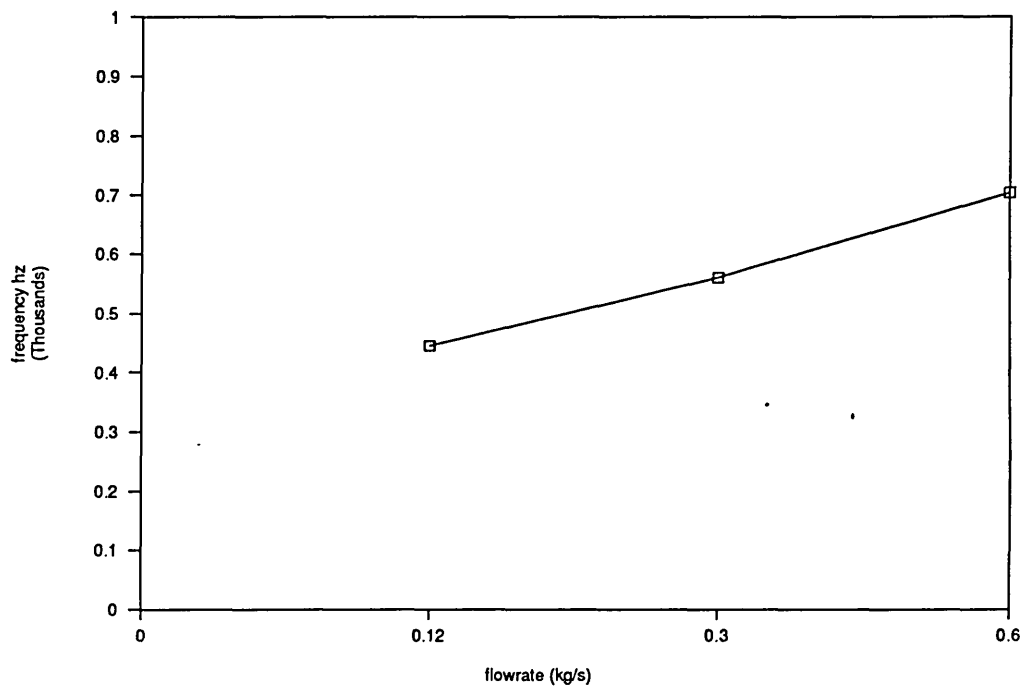


Figure 7.23 Peak frequency from signal spectra
with change of flowrate - core flow.

7.6.1.5 Stratified flow.

The power spectrum for stratified flow shown in figure 7.24 shows a similar type of response to half flow (section 7.6.1.2). The lean flow regions again shows a maximum power frequency at 550 Hz. The two regions of dense flow correspond with the two regions of dense spectra.

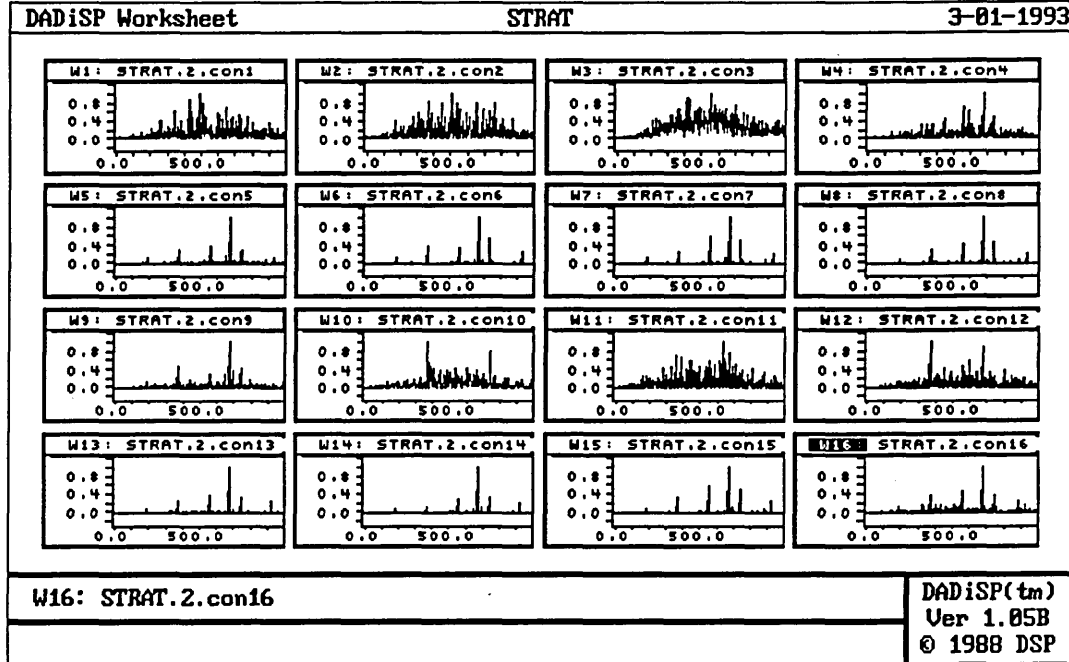


Figure 7.24. Relative spectra of Stratified flow.

7.7 Ratio backprojection for empirically-based image reconstruction.

The currently available methods for image reconstruction [Dyakowski 1993] are based on measurements made on the boundary of the conveyor. These values are fed into optimization models, generally called forward problem models. These models, based on Poisson's equation, describe an ideal relationship between, for instance, the measurements obtained and an electrical property such as electrical resistivity (electrical impedance tomography) or dielectric permittivity distribution (electrical capacitance tomography). Although a model-based method may be used for electrical charge tomography, an empirically based image reconstruction of particle flow from their charge distribution is demonstrated (section 7.7.2). The single particle flow reconstruction is discussed to highlight the principles in the ratio back-projection technique.

7.7.1 Single particle flow reconstruction.

To reconstruct the flow, the position of a particle (r, α) is found as follows:

1. From the voltage profile around the boundary of the pipe wall obtained by the technique described in section 6.2, the position where the maximum voltage is measured suggests which sensor is closest to the charged particle inside the pipe. In a single particle situation, a minimum voltage on the sensor diametrically opposite this maximum confirms where the charge is located.
2. In order to determine the radial position of the charge, a comparison is used. The minimum to maximum ratio is calculated. This is then plotted on figure 7.1 to obtain the range. Knowing the range value gives the radial position of the charge. The task of determining the particle position, r and α , is then achieved in reconstructing the image of the particle.

A direct analytical solution to the problem of the single charged particle in a circular boundary exists.

For each sensor,

$$v_i = -qk/D_i^2,$$

as derived in equation (4.3) . Hence,

$$v_1 D_1^2 = -qk$$

$$v_2 D_2^2 = -qk$$

.

.

.

$$v_n D_n^2 = -qk$$

Where $D_i^2 = r^2 + R^2 - 2rR \cos(\theta - \alpha_i)$.

Since the pipe radius (R), the sensor positions (θ) on the boundary are known from equipment geometry and the voltage v from measurements by each sensor, solving simultaneous equations gives the particle location, r and α . For each charge, there are three unknowns q, r, α . Three sensors are required to locate each charge so that simultaneous equations for three unknowns can be solved.

The analytical solution is complicated by the nonlinear relationship of the variables. This becomes more cumbersome as the number of particles used is increased.

7.7.2 Sand flow reconstruction.

The basis for reconstruction is in using ratio back-projection of information extracted from the measured signals:

1. The normalised boundary voltage profile provides spatial position of the flow (section 7.3),

2. The velocity profile provides local mass flow rates and concentration (section 7.5).

The ratio back-projection works on the principle that there is a relationship between the measured voltage and the position (and hence, distribution) of the solids on the cross-sectional plane of the sensors (section 7.3). The plane is divided and identified by a square mesh. To obtain the concentration map, the voltage profiles are used since they are directly related to flowrates (section 7.5).

The algorithm is:

1. From the voltage profile, determine the position of the pseudo-particle(s) (sections 3.2 and 3.3) from the ratio of maximum-minimum range with distance relationship.
2. From this profile, obtain the position of the nearest sensor(s) to the particle(s).
3. Identify the flow regime from the normalised voltage profile (section 4.3 and 7.3).
4. Use the ratio relationships between normalised voltage amplitude and particle distance to generate average concentrations for each section of the mesh in the cross section (figure 7.25).
5. Estimate the flowrate from the graphs of totalised voltage and flowrates for an identified flow regime (section 7.5).

The results shown (figure 7.26) is a reconstruction of the relative concentration distribution of the half flow (section 7.3.2). However, improved control of the experimental conditions is required to produce an image of higher resolution (section 8).

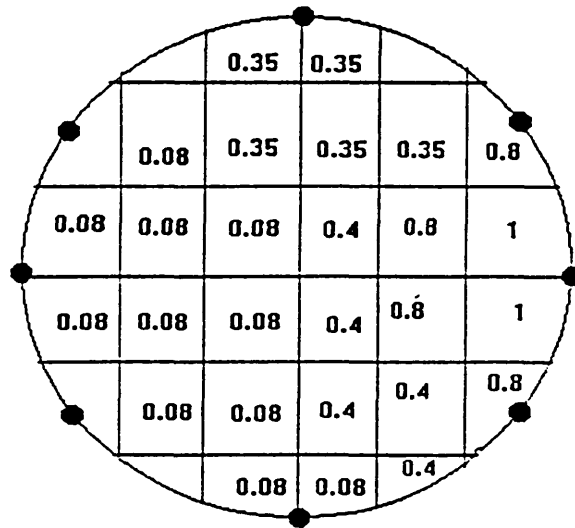


Figure 7.25 Relative charge distribution from ratio of normalised voltages to maximum normalised voltage.

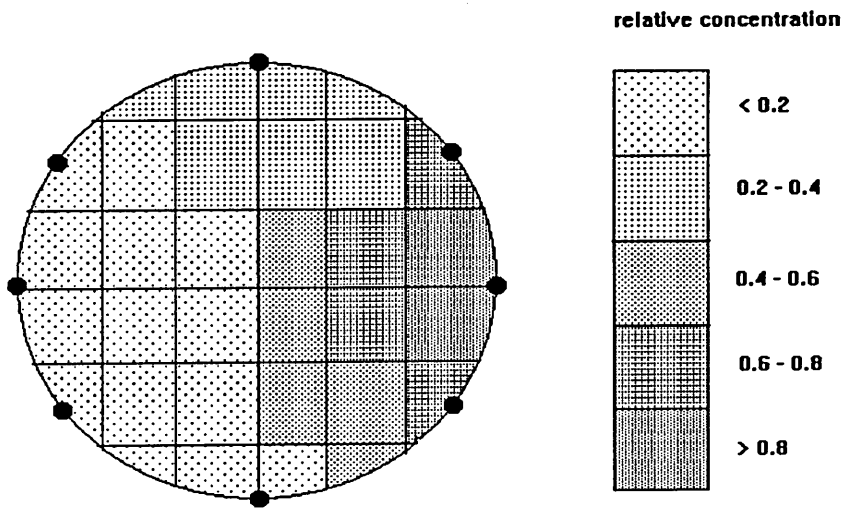


Figure 7.26. Concentration maps by reconstruction from measured data.

Chapter 8

Conclusions and Recommendations for Further Work.

8.1 General conclusions.

The specific aims and objectives of the thesis have been achieved as follows:

8.1.1 Single particle models.

Several models have been developed and evaluated. For the single particle, an induction model (section 3.2.2), a field model (section 3.2.3) and a moving particle model (section 3.2.4) have been investigated.

A comparison of the field and induction models using measured data (section 6.2) shows that induction is the primary method of coupling between the charge and the sensor. The induction model requires refinement, further work on this is suggested (section 8.2.1).

The moving particle model (figure 3.7) provides qualitative agreement with measured results (figure 6.2).

8.1.2 Two particle model.

A two particle model is developed (section 3.3) based on the single particle induction model. This model is useful in describing the flow regimes generated by the flowing sand (section 7.3).

8.1.3 Multiparticle model.

Equation 3.18 of section 3.4 relates the sensor potential to the transducer output voltage by a gain term which depends on the resistance and capacitance of the transducer circuit. The equivalent circuit of this impedance should be modelled to determine this gain term analytically (section 8.2.1).

The relationship between individual sensor output and mass flow rate is provided by the mass flow rate model (section 3.6). Totalised voltages are compared with mass flow rates of sand for four different flow regimes (section 7.5). Linear relationships are presented in all cases for flow rates up to 0.36 kg/s, at higher flow rates the linear relationship breaks down. This is explained by the discussion presented in section 7.6.1.2.

8.1.4 Neural network models.

Several variations of the original Kohonen self organising neural network have been tested (section 4.3) for performance of speed of convergence and correctness of mapping known inputs (figures 4.7 to 4.11). The parameters varied include the learning rate, neighbourhood updating function and competition mechanism. Controlling the neighbourhood by a Gaussian hat function provided the best results for the set of models tested. Using a biased competition mechanism performed well for a one-dimensional input mapping but not for higher dimensions. Tests with idealised flow regimes show over 95% success in correct classification which degrades to 85% with the introduction of 20% noise (section 4.3.4).

8.1.5 Electrodynamic transducers.

The electronic transducers consisted of buffer amplifiers with a guarded input interfacing directly to a data capture system (section 5.1).

However the work demonstrates the feasibility of using electrodynamic sensors to image dry particulates. These sensors are sensitive to the spatial variations of particle concentration inherent in real flows (section 6.3). An improved measurement system based on a specification derived from the work in this thesis is now designed and being evaluated [Alton 1993] and includes the incorporation of a fast data acquisition system (typically $3.5\mu\text{s}$).

8.1.6 Artificial flow regimes.

Different artificial flow regimes were produced by inserting baffles into the flow pipe (section 5.7). The regimes simulated by this technique included core, annular, stratified and half flows. These flows are necessary in order to investigate the effectiveness of the neural networks in identifying different flow conditions and to ensure that the sensors produced signals suitable for image reconstruction. The signals from the sensors show that the hopper feed system is not ideal (the feed is not uniformly distributed over the pipe cross section (section 6.3)) and the baffles were too close to the sensors. Section 8.2.2 provides suggestions to improve the flow conditions.

8.1.7 Boundary voltage profiles of sand flow.

The voltage profiles obtained show reproducible patterns (sections 6.3 and 7.3). These patterns of profiles are in general agreement with the profiles predicted by the single and two particle models (figure 3.8).

8.1.8 Flow regime identification.

A neural network programme (section 4.3.2) is used to classify flow data into several defined flow regimes (section 7.4). The success rate in identifying between full, half and stratified flows varied between 50% to 70%. The regime identification supplies information required for the determination of concentration and mass flowrate by identifying the appropriate gain term (equation 3.33 and section 7.5.2).

8.1.9 Velocity determination.

Cross correlation is used to determine the local velocity of flowing sand at different positions around the periphery of the flow pipe (section 6.4). Correlations deteriorate with obstructed flow due to interactions with the baffle (section 7.5). Suggestions on the use of correlation in this system is discussed in section 8.2.6.

8.1.10 Spectral analysis.

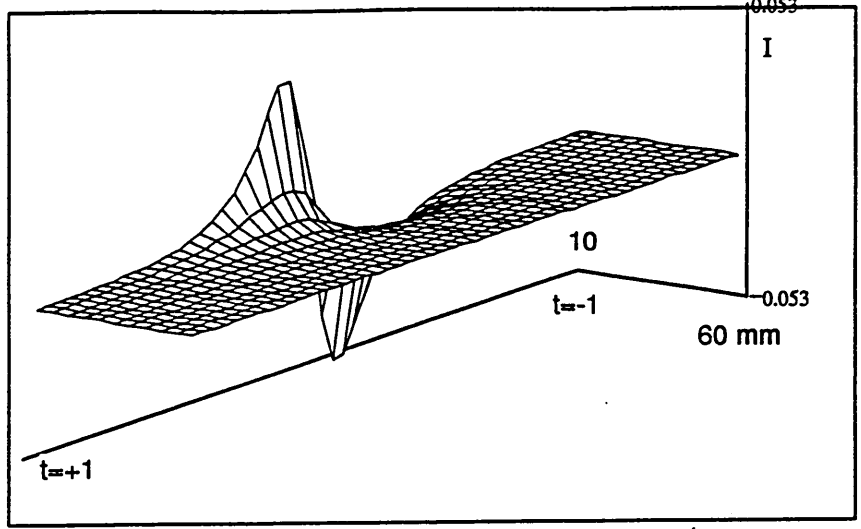
The spectra obtained from signals corresponding to low rates of flow were typified by single, well defined lines (section 7.6). The frequencies of these lines correspond to the two major particle sizes of the sand (figure 5.7). The spectral analysis carried out on the measured signals during the tests on the artificially produced flow regimes showed a noticeable shift to lower frequencies at higher feed rates. Two reasons for this shift are proposed (section 7.6), but further work is required (section 8.2.9).

radius from sensor (cm/s)

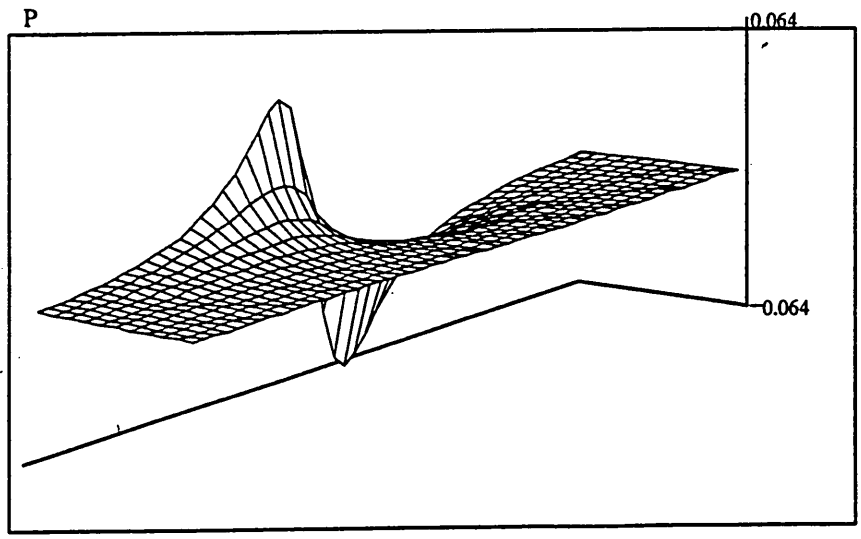
$$i := 0..N \quad j := 0..M \quad t_i := -1 + .04 \cdot i \quad r_j := 0.5 \cdot j + 1$$

$$f(t,r) := \frac{t}{[(r)^2 + 36 \cdot t^2]^2} \quad g(t,r) := \frac{t}{[(r)^2 + 36 \cdot t^2]^{1.5}} \quad h(t,r) := \frac{t \cdot r}{[(r)^2 + 36 \cdot t^2]^{2.5}}$$

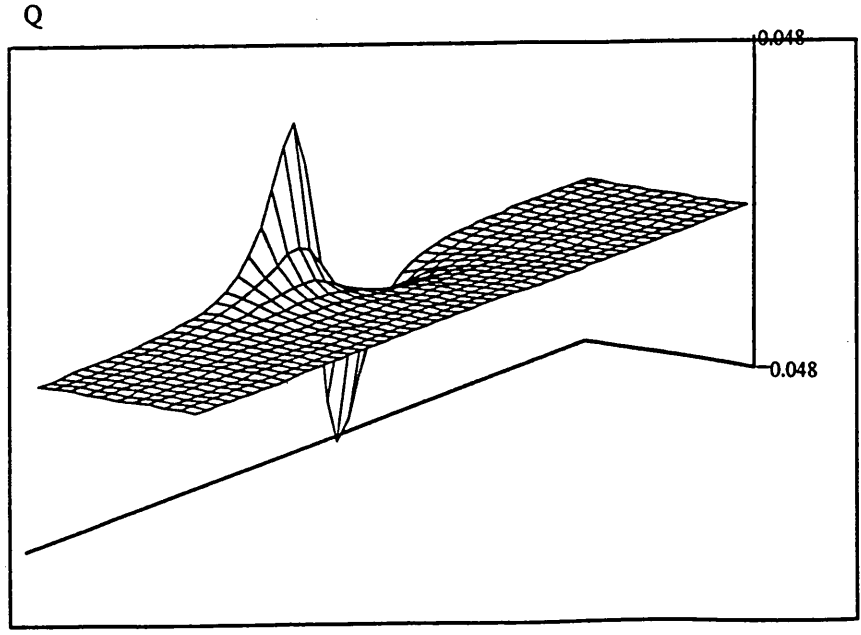
$$P_{(i,j)} := f(t_i, r_j) \quad Q_{(i,j)} := g(t_i, r_j) \quad R_{(i,j)} := h(t_i, r_j)$$



Bidin (1993)



Gregory (1987)



Beck (1986)

R

Figure 8.1 Comparison of Electrodynamic Models.

8.1.11 Image reconstruction.

An algorithm for image reconstruction based on ratio back projection is demonstrated (section 7.7). A coarse map of the concentration is obtained using this algorithm. Further work on reconstruction methods is proposed (section 8.2.7).

8.2 Suggestions for further work.

8.2.1 The mathematical models.

1. Several single particle dynamic models [Gregory 1987, Beck 1986, Bidin 1993] have been developed. Preliminary results of comparative tests are shown in figure 8.1. Many qualitative similarities appear to exist between the models and a detailed quantitative investigation is required. The variations between these induction models is primarily due to the various assumptions taken in their development. More controlled experiments should be made to determine the merits and limits of each model for future development of the image reconstruction algorithm.
2. Modelling of the gain term in equation 3.18 to relate the sensor output voltage and the equivalent circuit of the sensing mechanism, would provide a better basis for an improved design of the transducer electronics.

8.2.2 Improvements to the flow rig.

1. To maximise the probability that the baffles produce the required flow profiles, a distributor should be placed near the top of the pipe under the screw feeder to even out the sand flow.

2. The baffles should be placed at different heights up the tube to investigate the effect of pipe length on reproduction of flow regimes which are useful for developing process tomography systems. When the baffle is placed high up the pipe its effect on inter particle collisions occurring near to the sensors is reduced, which should provide more uniform flow rates with the required spatial distributions. This repositioning may enable further information to be obtained from cross correlations and spectral analysis.

3. The pipe section of the flow rig should be inclined at different angles to the vertical and the effects of sliding flow and increased local concentrations, which may contact the sensors, be investigated. This may be a suitable simulation to represent particle flow around a bend.

8.2.3 Sensor systems.

1. The electrodynamic sensor can only be used with flow rates up to 0.4 kg/s when the baffles are used before the gain characteristic becomes negative. Capacitive systems are less sensitive than electrodynamic, therefore investigate the use a combined capacitance and electrodynamic bimodal sensor system for applications over a wide range of flows.

2. The electronic design of the system can be optimized to include fast data acquisition and signal processing chips. The sampling time of the data capturing system should be improved to allow information on higher velocity flows to be collected. Direct memory access should be incorporated so more data can be stored to enable better averaging of the correlations and voltage profiles. Correlations and averaging could be done by dedicated signal processing circuits, which would speed up the overall system.

3. The number of sensors in an array should be extended until there is no discernible difference between adjacent pairs. This will enable the maximum amount of data to be collected for use in image reconstructions. Each sensor is providing a view, an increase in the number of views generally helps to improve the image resolution (Plaskowski et al 1992).

8.2.4 Range of flows.

The measurement system should be investigated for velocity and sand concentrations which are varied over a wide range. This will require the use of other flow systems such as fluidised bed and blow tanks. This would provide variations in the flow regimes of both vertical and horizontal pneumatic transport.

8.2.5 Neural networks.

1. The training of the neural networks should be improved to achieve higher rates of success in the identification of flow regimes. This may be achieved by using voltage

profiles that are averaged over a longer sampling time so that the variations of a pattern are minimised. More regimes should be introduced for the network to learn and classify in order to broaden the range of applications of the measurement system.

2. Use neural networks for identification in the frequency domain in order to separate regimes that would otherwise have non-contrasting patterns. The frequency domain characteristics of the signal would allow the neural networks to spot contrasts that perhaps would not be detected in the time domain signals. The spectral analysis of full, core and annular flows are shown to be different and would provide a starting point for further investigation into identification of flow characteristics in the frequency domain.

8.2.6 Cross correlation.

1. The cross correlation can be improved by hardware correlators or special digital signal processing chips embedded in the data acquisition system. The cross correlation of pairs of sensors around the pipe boundary should improve with better flow conditions, perhaps using the improved positioning of the baffles suggested in section 8.2.1.

2. With improved resolution of the reconstructed tomograms and two arrays of sensors it may be possible to provide velocity profiles of the flow. This would require cross correlation of pixels representing the upstream and downstream slices to be made. By correlating off axis pixels swirl velocities may be obtainable.

8.2.7 Reconstruction algorithms.

1. The image reconstruction can be improved by considering forward models based on the Poisson equation to represent charge distribution in a volume:

$$\frac{\partial^2\Phi}{\partial x^2} + \frac{\partial^2\Phi}{\partial y^2} + \frac{\partial^2\Phi}{\partial z^2} = -\frac{\rho_v}{\epsilon_0} \quad (8.1)$$

This problem requires a high computation power to achieve a solution within reasonable time. This is because the cross sectional plane of the sensor is divided into mesh sections to represent the distribution of charge. The task is to find each charge from the equation 8.1 and to test if the solution converges by comparing voltages obtained from experiments and calculations in an iterative way.

2. The optimized model suggested in section 8.2.1 should be used to obtain a direct analytical solution of the inverse problem. The number of particles that this approach can be used for should be investigated and combined with an investigation of the optimum number of sensors (section 8.2.3).

8.2.8 Particle sizing.

1. The investigation into the spectra of electrodynamic signals using power spectral density techniques has shown potential for use in the characterisation of particles by size distribution (section 7.6). The spectra obtained show a consistency over a large range of flowrates. Further more controlled experiments, in terms of the particle sizes used, should be investigated for relating electrodynamic spectral data to particle characteristics.

2. A change in process condition may cause different regimes of flow to be created and the spatial size distribution may shift over the cross sectional area being investigated. In this instance, the use of size distribution maps would be useful because the actual distribution of particles may affect the final product quality.

3. Experiments should be made to investigate the physical and electrical properties of particles that contribute to the different frequencies in the spectra. For instance, different materials have different dielectric relaxation times and frequencies [Etuke et al 1993]. This occurs when polarization of the dipoles in a given dielectric field fails to follow an applied alternating electric field. The knowledge of relaxation processes may hold the key to the structural and molecular nature of various materials [Birks 1961].

8.2.9 Effect of particle size.

1. Investigate the effects of size on signal amplitudes and frequency by using materials of narrow size distribution over a wide range of particle sizes from sub micron up to centimetre diameter.

2. Test with granular materials of millimetre size range and compare with results obtained for fine particulates to investigate the explanation given in section 7.6.2. In this investigation the effects of moisture content may be an important factor to be considered.

8.2.10 Application in liquids flow.

The work by King [1973] on liquid systems has shown the feasibility of measuring flow noise due to charging effects with electrodynamic sensors. The measurement system provided by this thesis should be tested on two component, non conducting, immiscible liquids and gas and non conducting liquid flows. The application of the mathematical models and techniques developed in this thesis may be adapted for such liquid based flow systems by considering the permittivities of the media used.

References.

Abdullah MZ, Dyakowski T, Dickin FJ, and Williams RA, Observation of hydrocyclone separator dynamics using resistive electrical impedance tomography, ECAPT93 Conference, Germany 1993.

Aleksander I, Why neural computing? a personal view. Neural Computing Architectures, the design of brainlike machines North Oxford Academic, 1988.

Anderson D, Neural Information Processing Systems. American Institute of Physics, New York, 1987.

Amadi-Echendu JE and Higham EH, Additional information from flowmeters via signal analysis, Conference Record IEEE Instrument and Measurement technical conference, p187-93 1990.

Barber, DC and Brown, BH, Applied Potential Tomography, J. Phys. E: Sci Instrum, vol 17 p723-733, 1984.

Beck, CM, Instrumentation and Control for minimum energy consumption in pneumatic conveying, PhD Thesis, University of Bradford, 1986(Dec).

Beck CM and Plaskowski, Crosscorrelation flowmeters, 1990.

Bertrand D, Robert P, Melcion JP and Sire A, Characterisation of powders by video image analysis, Powder Technology vol 66, p171-176 1991.

Binley AM, Dickin FJ, Henry-Poulter SA, Abdullah MZ and Gregory PJ, Observation of tracer migration using resistive electrical impedance tomography, ECAPT93 Conference, Germany 1993.

Birks, J and Hart B, Progress in Dielectrics, vol 3, London Heywood& Co Ltd 1961.

Clegg,IM, Non-invasive techniques for on-line measurement, Measurement and Control, vol 22, p102 May 1989.

Corbett RP and Bassett JD, Electric Field Measurements in ionic and particulate clouds, Proceedings of the 3rd Conference on Static Electrification, May 1971 .

Coulson JM and Richardson JF, Chemical Engineering vol2: Unit operations, Pergamon press 1968.

Coulthard, ICEMI92 Conference, China October 1992.

Cross J, Electrostatics; Principles, problems & Applications, Adam Hilger, 1987

DaDisp Manual, version 1.03 1987.

Dickin FJ, Hoyle BS , Hunt A, Huang SM, Illyas O, Lenn C, Waterfall RC, Williams RA, Xie CG and Beck MS, Tomographic Imaging of industrial equipment- review of needs and methods in Sensors, Technology & Application, ed Grattan, 1991.

Dickin FJ, Zhao XJ, Abdullah MZ and Waterfall RC, Tomographic Imaging of industrial process equipment - using electrical impedance sensors, in Sensors, Technology & Applications, 1991.

DeSieno D, Adding a conscience to competitive learning IEEE Conference on Neural Networks, 1988.

Duckworth HE, Electricity and magnetism, Holt, Rinehart and Winston, 1960.

Dugdale P, Green RG, Hartley AJ, Jackson A, Laundaro, Using optical sensor arrays in Sensors, Technology & Applications, 1991.

Dyakowski T, Process tomography for model validation, ECAPT93 Conference, Germany 1993.

ECAPT92, First meeting of the European concerted action on process tomography, Manchester 1992.

Etuke EO, Hall DA, Waterfall RC, Beck MS, Williams RA and Dyakowski T, Volumetric characterisation of a two particle type dispersion using impedance spectroscopy, ECAPT93 Karlsruhe 24-27 April 1993.

Featherstone AM, Green RG, Shackleton ME, Yarn velocity measurement, J Physics E: Sci Instrum vol 16 1983.

Freeston IL and Tozer RC, Impedance imaging using induced currents, ECAPT93 Conference, Germany 1993.

Gadhetsroni (Ed), Handbook of multiphase systems, Hemisphere publ corp 1982.

Gajewski JB, Mathematical model of non-contact measurements of charges while moving, J of Electrostatics, v15 , p81-92 (1984).

Gajewski JB, Kala W, How to measure the velocity and mass flow rate of a two-phase flow of solid particles in pipelines ?, Materials Science vol XVI No 1-3 1990.

Gajewski JB, Continuous Non-contact measurement of electric charges of solid particles in pipes of pneumatic transport Part I & II, Conference Record of the IEEE/IAS annual meeting, San Diego, USA, Oct 1-5 1989.

Green RG, Foo SH, Phillips JG, Flow measurement for optimizing the feed rate of pulverised fuel to coal fired boilers, Symposium on Fossil Energy Processes, USA 1981.

Green RG, PhD Thesis, Bradford University, 1981.

Gregory I, Shot Velocity measurement using electrodynamic transducers, PhD Thesis, UMIST, May 1987.

Griffiths DJ, Introduction to electrodynamics, Prentice Hall, 1981.

Grattan KTV (ed), Sensors - Technology, Systems & Applications, Adam Hilger, 1991.

Grossberg S, Studies of Mind and Brain. D. Reidel Publishing, (1982).

Gutierrez M, Wang J and Grondin R, Estimating hidden units for two layer perceptrons IEE Conf on Artificial Neural Networks (1989).

Hammer EA and Nordtedt JE, The application of a Venturi meter to multiphase flow of measurement in Grattan,KTV (ed), Sensors - Technology, Systems & Applications, 1991.

Harper WR, Contact and Frictional electrification, Oxford University Press, 1967.

Hebb DO, The organization of behaviour, New Wiley 1949.

Helicon Encyclopaedia, Helicon Publishers 1991

Henry RM and Beck MS, Incipient fault detection in pipeline transporting solid material, On-line surveillance and monitoring of process plant, Society of Chemical Industry 1977.

Hestenes D, How the brain works: the next scientific revolution, in Maximum Entropy spectral analysis and estimation problems, ed C.R.Smith and G.J.Erickson, D.Reidel Publishing (1987).

Higham EH, Fell R and Ajaya A, Signal analysis and intelligent flowmeters, Measurement and Control, June 1986.

Hosseini-Ashrafi ME, Tuzun U, MacCuaig N, Study of bed voidage in packed bed flows using photon transmission tomography, ECAPT92 Proceedings, p259 1991.

Howard JR, Fluidized Bed Technology: Principles and applications, Adam Hilger 1989

Hua P, Woo EJ, Reconstruction Algorithms, in Electrical Impedance Tomography Ed Webster, 1990.

Huang SM, Stott AL, Green RG and Beck MS, Electronic transducers for industrial measurement of low value capacitances, J Phys E: Sci Instrum vol 21 1988.

Huang SM, Plaskowski AB, Xie CG and Beck MS, J Phys E : vol 22, p173 1989.

Huang SM, Xie CG, Thorn R, Snowden D, Beck MS, Tomographic Imaging of industrial process equipment - design of capacitance sensing electronics for oil and gas based processes, in Grattan, KTV (ed); Sensors - Technology, Systems and applications, 1991.

Iinoya K, Hiroaki M, Watanabe K, Powder and bulk solids handling processes: instrumentation & control, Marcel Dekker, 1988.

Ilyas O and Williams R, Will Tomography make CFD models redundant ?, ECAPT93, Karlsruhe, 1993.

Ioannis N Miaoulis and Behrouz Abedian, A passive probe for electrostatic charge density measurements, Review of Scientific Instruments, vol 61 no 11 Nov 1990.

Izakov FY and Zubstov PA, Flowmeter for loose materials, Measurement Techniques (translated from Izmeritel'naya Tekhnika), no 10 p50-51 1979.

Johnk C, Engineering Electromagnetic fields and waves, John Wiley and Sons, 1988.

Josin G, (1987) Neural Network Heuristics. Byte. Oct 87.

Karna K and Breen D, An artificial neural network tutorial Neural Networks vol 1 no 1, Learned Information Ltd, 1989.

Kelly EG, Spottiswood DJ, The theory of electrostatic separations: A review Part 3: Particle Charging Minerals Eng vol 2 No 2 , 1989.

Kemp IC, Oakley DE , Bahu, RE, Computational fluid dynamics modelling of vertical pneumatic conveying dryers, Powder Technology, vol 65 p 477-84 1991.

Khan SH, Abdullah F, Computer aided design of process tomography capacitance electrode system for flow imaging, in Grattan, KTV (ed); Sensors - Technology, Systems and applications, 1991.

King PW, Mass flow measurement of conveyed solids by monitoring of intrinsic electrostatic noise levels, Pneumotransport 2 , second International Conference on pneumatic transport of solids in pipes, 5-7 Sep 1973, Surrey.

Kohonen T, Self Organisation and Associative Memory Springer-Verlag 1984.

Kohonen T, The Role of Adaptive and Associative Circuits in Future Computer Designs, Neural Computers, Edited by Eckmiller & V. D. Malsburg Springer Verlag, Berlin, 1988.

Kress-Rogers E, Instrumentation in the food industry, part II: Physical determinands and process control, J Physics E: Sci Instrum Vol 19 1986.

Lapple CE, Electrostatic Phenomenon with particulates, Advances in Chemical Engineering, 1970 vol8.

Leschonski K, Two phase flow techniques as applied in characterisation, PSA 91, Conference on particle size analysis, Loughborough 1991.

Li H, Xia Y, Tung Y and Kwauk M, Microvisualization of clusters in fast fluidised bed, Powder Technology vol 66 1991 p231-235.

Li W and Hoyle BS, Sensor optimisation for ultrasonic process tomography, ECAPT93 Conference, Germany 1993.

Lippmann R, An introduction to computing with Neural Nets, IEEE ASSP Magazine. 4-21, 1987

Louis AK and Natterer F, Mathematical problems of computerized tomography, Proceedings of IEEE vol71 no3 1983.

Lowell J, The electrification of polymers by metals, J Physics D: Appl Phys v 9, 1976.

Lynn PA, An introduction to the analysis and processing of signals, Macmillan 3rd edn 1989.

Malave-lopez J and Peleg M, Linearization of the electrostatic charging and charge decay curves of powders, Powder Technology Vol 42, 1985, p217-223.

Mclelland, Rumelhart and PDP Research Group, Parallel Distributed processing Explorations in the microstructure of cognition, Psychological and Biological Models. 2, 534-535, 1986.

Meade ML and Dillon CR, Signals and systems: models and behaviour, van Norstrand 1986.

Mills E and O'Neill BC, Particle flow instrumentation, Proc Second Int Conf on Applications of transputers 1990, p56-62.

Neff HP, Introductory electromagnetics, John Wiley and sons, 1991.

Nordin MJ, Multimodal tomographic reconstruction, unpublished Technical Report, Sheffield Hallam University 1993.

Norman D, Reflections on Cognition and PDP in PDP vol2 ed Rumelhart and McClelland, MIT Press 1986.

Plaskowski A, Bukalski P, Habdas T, Skolimaski, Tomographic imaging of process equipment - application to pneumatic transport of solid material, in Grattan,KTV (ed); Sensors - Technology, Systems and applications, 1991.

Plaskowski A, Beck MS and Thornton J, Flow Imaging (in publication) 1993.

Pao Y, Adaptive Pattern Recognition and Neural Networks, Addison Wesley 1989.

Rhodes MJ, Pneumatic Conveying, Chapter 7 in Principles of Powder Technology, ed M Rjodes, John Wiley & Sons 1990.

Ritter H, Martinetz and Schulten K, Neural computaion and self orgaizing maps, Addison Wesley ,1992.

Rossner M and Singer H, Measurement of micrometer particles by means of induced charges, Conf Record IEEE Industry Applications Soc, 1982.

Rumelhart & McClelland and the PDP research Group, Parallel Distributed Processing: Explorations in the microstructure of cognition. Vol. 1: Foundations MIT Press 1986.

Saeed N, Browne MA, Green RG and Martin P, Two component flow regime identification and imaging with optical sensors, IMEKO XI, Houston 16-21 Oct 88.

Savage SB, Powder Flow, Conference notes IFPRI Meeting, Harrogate 1992.

Shackleton MS, MPhil Thesis, Bradford University, 1981.

Smythe WR, Static & Dynamic Electricity, McGraw Hill, 1968.

Strawberry Tree Inc, Workbench manual version 2.01, 1991

Sydenham PH, Thorn P, Hancock NN, Introduction to measurement science and engineering, Wiley, 1989.

Von der Malsburg, Goal and Architecture of Neural Computers, NATO Scientific Affairs Division 1989.

Wernsdoffer, ECAPT92, Manchester 1992.

Williams RA, Xie CG, Dickin FJ, Simons SJR, Multiphase flow measurement in powder processing, Powder Technology vol 66 1991.

Woodhead SR, Coulthard J, Byrne B, Barnes RN and Reed AR, On-line mass flow measurement in low suspension density pneumatic conveying systems using electrostatic technique, Pneumotech 4, 1990.

Xie CG, Mass flow measurements of solids in gravity drop conveyor using capacitance transducers, PhD Thesis, UMIST July 1988.

Xie CG, Plaskowski A, Beck MS, 8 electrode capacitance system for two component flow identification, IEE proc vol136 ptA no 4 July 1989.

Xie CG, Huang SM, Hoyle BS, Beck MS, Tomographic Imaging of industrial equipment - development of system model & image reconstruction algorithm for capacitive tomography, in Grattan, KTV (ed); Sensors - Technology, Systems and applications, 1991.

Xie CG, Huang SM, Hoyle BS, Thorn R, Lenn C, Snowden D and Beck MS, Electrical Capacitance Tomography for flow imaging: system model for development of image reconstruction algorithms and design of primary sensors, IEE Proceedings G vol 139 no1 Feb 1992.

Xie CG, Electrical capacitance tomography, ECAPT93 Conference, Germany 1993.

Publications of the Research.

2.1 Publications list.

Publications produced during the period of this research are as follows :

1. Bidin AR, Green RG, Stott L, Taylor RW and Shackleton ME, Electrical-Charge Tomography, in "Tomographic techniques for process design and operations" ed MS Beck, CEC Brite Euram Computational mechanics publication, 1993
2. Bidin AR and Green RG, Electrical-Charge Tomography in powder flow, Conference notes in Control of Particulate Processes III, Engineering Foundation, Santa Barbara, 24- 29 January 1993
3. Bidin AR and Green RG, Flow regime identification from tomographic data, Conference notes in Control of Particulate Processes III, Engineering Foundation, Santa Barbara, 24- 29 January 1993
4. Bidin AR, Green RG, Shackleton ME, Stott AL and Taylor RW, Process Tomography using electrodynamic sensors, ECAPT93 conference, Karlsruhe, Germany 1993.
5. Bidin AR, Green RG, Shackleton ME, Taylor RW, A prototype electrodynamic imaging system for pneumatic conveyors, ECAPT'92 , European Concerted Action on Process Tomography, Manchester, 26-29 March 92.
6. Bidin AR, Green RG, Taylor RW, Shackleton ME, Process Tomography using electrodynamic measurements, ICEMI'92 Int Conf on Electronic Meas and Instrumentation, Tianjin University, China, October 92
7. Bidin AR and RG Green, Development of Electrodynamic flowmeter for pneumatic transport of particulates, 'Manufacturing Week', under R&D Village with Laboratory of Government Chemist, Birmingham NEC 24-27 Nov 92

8. Bidin AR and RG Green, On-line flow measurement using electrodynamic sensors for tomographic imaging of dry particulates, IFPRI'92, Int Fine Particle Research Institute, Harrogate, 2nd - 5th June 92

9. Bidin AR and RG Green, Flow Regime Identification by Neural networks, 10th Meeting of UK Process Tomography Group, Sheffield-Hallam University, 10th Sept 92.

10. Bidin,AR and RG Green, Tomographic Imaging using electrodynamic measurements, 10th Meeting of UK Process Tomography Group, Sheffield Hallam University, 10th Sept 92.

2.2 ECAPT Task 3 report.

This project has been recognised as Task 3 under the European Concerted Action on Process Tomography, ECAPT, and a recent report was presented by Dr RG Green at the ECAPT93 Conference in Karlsruhe, Germany, March 24-27.

2.3 Du Pont invited paper.

This project was evaluated on 9th December 1992 by Dr Arthur Boxman of Du Pont's Center for Particle Science and Technology and has been granted an award of US\$12000 and an invited presentation of the work in a specialist workshop on Control of Particulate Processes, January 24-29th, 1993.